Synthesis and Characterization of Metallic Crystalline - Amorphous Cu-Zr Composites

By

Ehsan Alishahi

A thesis submitted to
the Faculty of Graduate Studies
in partial fulfilment of
the requirements for the degree of
Doctor of Philosophy

Department of Mechanical Engineering

University of Manitoba
Winnipeg, Manitoba

August 2018

Abstract

Commercial applications of bulk amorphous metallic glasses are restricted due to a sudden brittle failure mode. To overcome this limitation, a toughening strategy in metallic glasses based on the introduction of large quantities of crystalline – amorphous (C-A) interfaces has been widely proposed, e.g., to form various types of C-A composites. Accumulative roll boding (ARB) technique as a cost-effective synthesis method that can be potentially used for producing bulk sized C-A composites, has thus received significant attention in recent years. However, previous studies on expensive highly pure Cu-Zr multilayers did not show neither significant amorphization nor alloying during the ARB process. This research aims to modify the ARB technique for the synthesis of cost-effective bulk C-A composites based on commercially available Cu-Zr sheets. The proposed ARB guideline provides conditions which ensure mechanical alloying and amorphization of CuZr phases in a commercial Cu-Zr alloy system. The composition and structural analysis revealed that intermediate annealing facilitates the formation of several amorphous and crystalline CuZr phases during the ARB process. Additionally, mechanical tests based on nanoindentation indicated that the CuZr phases, whether they are crystalline or amorphous, show a higher hardness and elastic modulus than pure Cu and Zr phases. Numerical molecular dynamics technique was also employed to study the fundamental structure-property relation at the C-A interface. Based on the results, the interfacial energy demonstrated a weak dependence on the crystalline orientation. In contrast, the plasticity of C-A composites was mainly determined by crystalline orientation at the C-A interface.

Keywords: ARB, Crystalline – Amorphous Interface, Nanoindentation, Structure-Property Relation, Molecular Dynamics

Acknowledgments

I would like to thank my supervisor Prof. Chuang Deng for his support throughout my Ph.D. research. I would like to thank my advisory committee members Prof. Derek Oliver and Prof. Nan Wu for their helpful supports.

I am extremely thankful to the generous funding I have received including the University of Manitoba Graduate Fellowship, International Graduate Student Entrance Scholarship, Faculty of Graduate Studies, Graduate Students Association and Faculty of Mechanical Engineering.

I would like to thank NSERC Discovery grant (RGPIN 430800-2013), Canada, that supported this research. Also thank to WestGrid and Compute/Calcul Canada which provide computing resources. Experimental equipment and services provided by Manitoba Institute for Materials (MIM) are really appreciated.

Last but not least, my sincere thanks to my family and friends for their unconditional support.

Dedication

Dedicated to my beloved soulmate, Sanaz, for her unconditional generous love and support in my life.

Table of Contents

List of Figures

List of Tables

List of Copyrighted Materials

Figure 2-4 Phase diagram for binary Cu-Zr alloys (used with permission from Springer Nature, license number 4304250357590).

Permission was obtained to reuse the published figures (Figure 3-7, *Figure 4-19*, Figure 4-20, Figure 4-21, Figure 4-22, Figure 4-23, Figure 4-24, Figure 4-26, Figure 4-27, Figure 4-28 and Figure 4-29) in a journal paper with the title of "**Orientation dependent plasticity of metallic amorphous-crystalline interface**", Computational Materials Science 141 (2018) 375–387. The permission statement is as following:

"Please be advised that Elsevier allows their authors to reuse their own materials in a thesis/dissertation without having to obtain permission as long as it is not published commercially." Further information can be found in the link below.

https://www.elsevier.com/about/our-business/policies/copyright#author%20rights

List of Abbreviations

List of abbreviations	**Description**
BMG	Bulk Metallic Glass
MG	Metallic Glass
C-A	Crystalline-Amorphous
ARB	Accumulative Roll Bonding
SEM	Scanning Electron Microscopy
EDS	Energy-Dispersive X-ray Spectroscopy
TEM	Transmission Electron Microscopy
EBSD	Electron Back Scatter Diffraction
SPD	Severe Plastic Deformation
MD	Molecular Dynamics
MC	Monte Carlo
CRSS	Critical Resolved Shear Stress
STZ	Shear Transformation Zones
XRD	X-ray Diffraction
d_{hkl}	Inter-planer Spacing
RDF	Radial Distribution Function
T_g	Glass Transition Temperature
T_m	Melting Point Temperature
R_c	Critical Cooling Rate
T_{rg}	Reduced Glass Transition Temperature
CN	Coordination Number
NVT	Conical Ensemble
NPT	Isothermal-Isobaric Ensemble

EAM	Embedded Atom Method
LAMMPS	Large-Scale Atomic/Molecular Massively Parallel Simulator
γ_{int}	Interface Energy
γ_{sur}	Free Surface Energy
C-A model	Crystalline – Amorphous Model
A-NC-A model	Polycrystalline Amorphous – Crystalline - Amorphous Model
t_{cu}/t_{zr}	Thickness Ratio of Cu and Zr Layers
σ_{zz}	Normal Stress along Z Direction
ε_{fd}	Strain at which the First Dislocation Nucleates
t_c	Thickness of Crystalline Layer

Chapter 1 : Introduction

Metals and metallic alloys play important roles in a variety of industries, from simple house furniture to ultra-complex aerospace shuttles. Metallic materials can be classified into two main categories: as either crystalline or amorphous based on their atomic structure. Crystalline materials are materials with a periodic pattern of atoms. Materials in which the atoms or molecules are not arranged in a periodic pattern are called amorphous materials. The structural differences between crystalline and amorphous metals leads to their distinct characteristics in terms of their mechanical properties and microstructures.

Although most metals are identified as crystalline, the new class of amorphous alloys, commonly known as metallic glasses (MGs), have exhibited remarkable properties such as high mechanical strength and elastic limit [1]. Commercializing MGs has been limited by a major drawback: the lack of ductility and a sudden brittle failure mode. Hence, crystalline-amorphous (C-A) composites have been introduced as a toughening strategy to improve the ductility of MGs [2]. Despite the initial successes, there are still challenges in both the synthesis and characterization of metallic C-A composites. In particular, the complicated interaction mechanisms between crystalline and amorphous phases are still not well understood, and hence, require an extensive and systemic investigation. This

research aims to introduce a cost-effective technique for the synthesis of bulk metallic C-A composites based Cu-Zr multilayers as a model system. It also aims to investigate the micromechanisms associated with the plasticity of C-A composites.

1.1 Background

One of the main disadvantages of MGs is the lack of ductility and, consequently, the possibility of catastrophic brittle failure under operational loading conditions [3]. The failure mechanism in amorphous metals is governed by the nucleation and propagation of high local inelastic shear strain clusters known as shear transformation zones (STZs) [4]. STZ collections on the maximum shear strain plane can lead to the localization of shear deformation in a local narrow region, called a shear band [5]. In order to improve the toughness of amorphous MG alloys, the shear localization (i.e. shear band formation and propagation) can be restricted through reinforcing micromechanisms (i.e. C-A interface). C-A composites have been introduced as a toughening strategy in MGs [6]. The C-A composite plasticity can be enhanced by the presence of the C-A interfaces; which impede shear band propagation, thereby leading to a more uniform shear deformation state [7].

Different methods have been used in the synthesis of metallic C-A composites, including melting and quenching, sputtering and mechanical alloying [1]. Melting the metallic components and quenching the liquid solution to the solidification temperature used to be the conventional technique in the synthesis of MG alloys. Initial attempts focused on synthesizing C-A composites by nucleating a secondary crystalline phase inside the glassy matrix during the quenching process. One example carried out was the preparation of a

dendritic Zr-Ti crystalline structure grown in equilibrium with a glass forming Zr-Ti-Cu-Ni-Be alloy [8]. In spite of initial successes, there are still many challenges including the limited range of compositions, and the high sensitivity to the cooling rate [2].

Multilayer C-A structures, synthesized by deposition techniques (e.g. sputtering), have been studied extensively. For instance, crystalline Cu- amorphous CuZr nanolaminates have been synthesized using magnetron sputtering [7]. Results showed an almost 14% increase in tensile elongation in the sputtered Cu-CuZr multilayers. While magnetron sputtering is well-suited to the synthesis of multilayer thin films and coatings, technical limitations (i.e., atomic layer by atomic layer deposition process) makes synthesis of bulk samples challenging.

The ARB technique has been used in the synthesis of bulk metallic composites such as nanolamellar Cu-Zr structures [9]. The simplicity and low production costs are two considerable advantages of the ARB technique. Results have shown that the plastic elongation can increase from 8% to 14% after 6 cycles of the ARB process. It is also possible to achieve an amorphous state at the interface of the crystalline layers during the ARB process, resulting in a bulk C-A composite. Amorphization at the interface of the highly pure (~ 99.8 %) crystalline Cu-Zr multilayers during the ARB process has been explained by inter-diffusion mechanisms [10]. However, TEM results demonstrated that the amorphous regions are limited to narrow areas (with thickness of less than 1 nm) at the interface of Cu and Zr layers. Additionally, the expensive highly pure Zr sheets causes a huge spike on the cost of large-scale production of C-A composites. On the other hand, it has been shown that the purity level of Zr sheets has strong influences on their mechanical

properties [11]. More specifically, the high hardness values of commercial Zr sheets with lower purity level and consequently, large mismatch in hardness between Cu and Zr sheets, cause significant differences in elongation rate of Cu and Zr layers during the rolling step. As a result, the achievable number of ARB passes will be limited as the uniform co-deformation of Cu and Zr sheets cannot occur. Therefore, it will be challenging yet necessary to modify the ARB process to achieve alloying and amorphization based on commercially available Cu and Zr sheets which is one of main goal of this research.

The effects of failure mechanisms in crystalline (dislocation activities) and amorphous (STZ and shear banding) phases on the plasticity of C-A composites have been studied extensively. For instance, Wang *et al*. [7] reported Cu-Cu_3Zr composites with significant toughness enhancement which was attributed to the absorption of dislocations at the C-A interface. Ductility improvement due to the suppression of shear banding at the C-A interfaces has also been reported for Zr-ZrCu micro-pillars under compression [12] and Cu-CuZr thin films under tension [13]. Nanoindentation and transmission electron microscopy (TEM) analysis has revealed coincidences of shear banding and dislocation at the interface of a multilayered Cu-CuZr system synthesized by magnetron sputtering [14].

Overall, the complex characteristics of such inhomogeneous defects (C-A interfaces) merit more investigation. It is not clear yet which phase (crystalline or amorphous) fails first and/or how the interaction between the failure mechanisms (dislocations and STZs) enhances the plasticity. Understanding the structure-property relationship is critical to addressing these questions. This research aims to investigate the structure-property relationship of the C-A interface using a numerical approach.

1.2 Research Hypotheses

The hypotheses of this research are stated as follows:

Hypothesis I: It is hypothesized that by implementing heat treatment procedure in the ARB process, large deformation strain (significant number of ARB passes) can be achieved in commercially available Cu/Zr multilayers.

Hypothesis II: It is hypothesized that intermediate heat treatment has significant influence on amorphization and alloying during the ARB process, particularly in commercial Cu/Zr multilayers with large mismatch in hardness and ductility.

Hypothesis III: It is hypothesized that crystalline orientation at the C-A interface is an influencing parameter on initiation of and interaction between plasticity mechanisms in crystalline and amorphous phases.

1.3 Scope and Objectives of Research

In summary, the objectives of this research can be summarized as follows:

I. Development of an ARB operational guideline for the synthesis of cost-effective bulk C-A composites based on a commercially available Cu-Zr alloy system

II. Microstructural and mechanical characterization of the ARB synthesized Cu-Zr composites

III. Atomistic investigation of the amorphization during the ARB process and plasticity at the C-A interface

1.4 Thesis Layout

The following thesis is categorized in 5 chapters, the first of which provides an overview of the research. *Chapter 2* is a literature review and is followed by *Chapter 3* which contains the methodology used in these investigations. *Chapter 4* contains the results and discussion from both experimental and molecular dynamics (MD) investigations. Finally, concluding remarks and recommendations for future work are in *Chapter 5*.

Chapter 2 : Literature Review

In the following chapter, the physical properties of crystalline and amorphous metals are reviewed, followed by an overview of the fundamentals of MD simulation. A review of the previous studies on the synthesis and mechanical properties of C-A Cu-Zr composites, which are the focus of this work, is also included.

2.1 Crystalline Metals

Atoms or ions in a crystalline metal are positioned in a repeating, or periodic pattern over large atomic distances. This long-range order is a key characteristic of crystalline metals. The crystal structure is defined by the manner in which atoms are arranged in three dimensional space [15]. In this context, the lattice is defined as a three-dimensional array of points which represent the atomic centers (positions) [15]. The smallest repeating atomic unit that shows the full symmetry of the crystalline structure is known as the unit cell [16]. Most metals have one of three relatively simple crystalline structures including face-centered cubic (FCC), body-centered cubic (BCC) and hexagonal close-pack (HCP) [15]. If the repeating atomic arrangement extends over the whole structure it is called single crystalline. Generally, the repeating atomic arrangement is interrupted and the structure

contains many small crystals or grains [15]. In these polycrystalline materials, the different crystalline orientation for each grain causes atomic mismatches at the grain boundaries.

Much of the knowledge in atomic arrangement and crystalline structures came from studies carried out using X-ray diffraction (XRD). The incident X-ray beam can be diffracted with an angle of diffraction which is correlated to the crystalline inter-planer spacing. The relationship between X-ray wavelength (λ), the crystalline inter-planer spacing (d_{hkl}) and the angle of diffraction (θ) can be described by Equation 2-1, which is known as Bragg's law [17].

$$n\lambda = 2d_{hkl} \sin\theta \qquad \text{Equation 2-1}$$

Those crystallographic planes which satisfy the Bragg's diffraction condition, result in the high intensity peaks in the diffraction pattern. The crystalline structure can also be determined from radial distribution function (RDF) analysis. RDF analysis measures the probability of finding an atom at distance *r* from a reference atom [18]. Discrete peaks will appear in the RDF analysis of crystalline models, representing the nearest neighbor atoms for the crystalline structure.

Plastic deformation in crystalline metals is associated with dislocations nucleation and motion [15] and the corresponding process is termed slip. Dislocation motion usually occurs on the crystalline plane with the highest atomic packing, and in a direction in that plane with the highest linear density. For instance, in FCC metals the slip system contains a set of {1 1 1} plane and <1 1 0> direction which is usually represented as {1 1 1} <1 1 0>. In a more detailed description, the slip process in FCC metals can occur by two different

mechanisms: known as full (1/2{111} <1 1 0>) and partial (1/6{1 1 1} <1 1 2>) dislocation nucleation. The dissociation of full dislocation to partial dislocations occurs if the total energy of partial dislocations is lower than that of full dislocation.

2.2 Amorphous Metals

Discovery of amorphous metallic materials dates back to the 1960s, when a glassy Au-Si alloy was synthesized by a process with high solidification rates [19]. Lack of long-range order is a key characteristic of this new class of metallic materials. Since amorphous metallic materials show a glass-like structure during the cooling process, terminologies such as metallic glasses (MGs), or glassy alloys were also used to describe these amorphous metals. Commercial applications of amorphous alloys increased in the 1990s due to their outstanding mechanical properties, i.e. high elastic limit and strength, and corrosion resistance [20–23]. Due to the fact that these alloys had thicknesses of more than 1 mm, the term bulk metallic glasses (BMGs) was used by researchers at that time. This section aims to provide a brief review of the physical properties of amorphous metallic alloys, including glass transition, structure and mechanical characteristics.

2.2.1 Glass Transition

During cooling of a metallic liquid, the specific volume decreases with temperature to the melting point (T_m, Figure 2-1); at which the volume drops rapidly to the characteristic value of the solid crystalline phase. Below T_m the reduction of specific volume continues slowly.

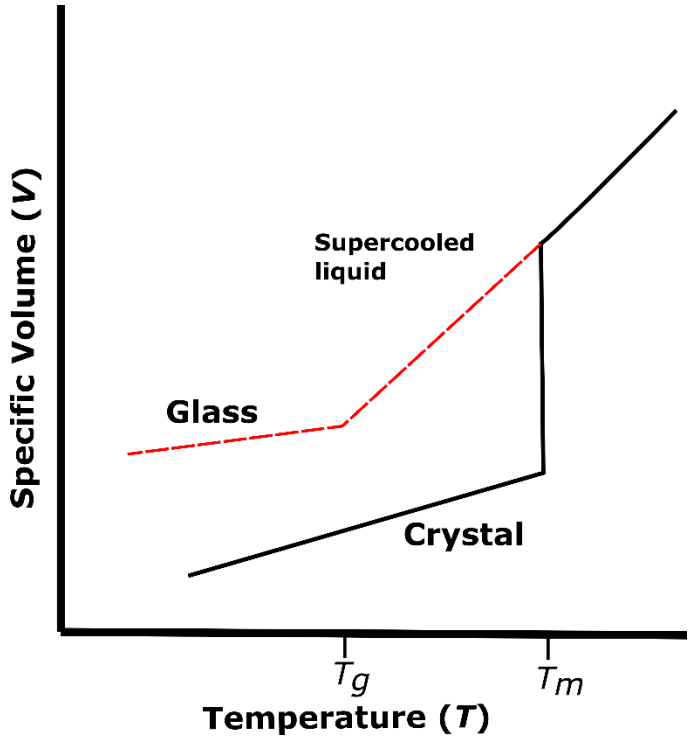

Figure 2-1: Reduction of specific volume vs. temperature during glass formation of liquid alloy (adopted based on a figure in [1]).

In the case of amorphous formation, the liquid state can be maintained at a temperature below T_m without showing crystallization (called as undercooling or supercooling). As long as the liquid undercools the volume will continue to decrease while the viscosity increases. The viscosity becomes very high at temperatures well below the T_m, and the liquid phase transfers to a solid-like state coined "frozen-in" [1]. At the "frozen-in" state the phase is referred to as glass and the corresponding temperature is referred to as the glass transition temperature (T_g, Figure 2-1). A sharp, definite glass transition temperature is frequently not presented, and instead, it is identified as a "glass transformation interval" [24]. However, there is an empirical definition for T_g based on the temperature corresponding to the viscosity value of 10^{12} Pa.s [1].

There is a critical cooling rate (R_c) beyond which the glass formation will occur [1]. The R_c is strongly dependent on the alloying elements (type and number of elements in an alloy system) and compositions. As mentioned earlier, undercooling the liquid solution to a temperature well below the T_g is required to form glassy state. Rapid solidification with a cooling rate above R_c is necessary to ensure this undercooling. The second important factor in glass forming ability of an alloy system is the reduced glass transition temperature ($T_{rg} = \frac{T_g}{T_l}$), where T_l is the temperature at the end of liquid formation or melting [25]. Higher values of T_{rg} correspond to easier glass formation in an alloy system. Finally, a significant atomic size mismatch is a key parameter in glass forming ability in metallic systems (minimum 12% atomic size difference has been suggested in Inoue criterion [1]).

At temperatures well below T_g the glassy state of solid metals is not in an equilibrium state. However, the properties of glassy alloys can be described as time independent with respect to experimental timescales. BMGs typically exhibit a reversible transition from glass to liquid state at T_g; suggesting that the atomic structure of glassy alloys is closely related to the liquid state [1].

2.2.2 Amorphous Structure

The periodicity of a crystalline structure means that there is a unique coordination number (CN), the number of nearest neighbor atoms, for each atom. As this periodicity is absent in amorphous (glassy) alloys, it is difficult to define a unique CN. The lack of long-range order in amorphous systems can be characterized by peak broadening in XRD patterns of

MGs. Unlike the crystalline phase with sharp peaks, there is just one broadened peak in XRD patterns of amorphous alloys indicating the randomness of the atomic arrangement.

It is also possible to study the structural characteristics of amorphous alloys using theoretical and numerical parameters such as RDF and Voronoi analysis. In contrast to crystalline structures, discrete peaks are not presented in RDF analysis of amorphous alloys since the CN is different for each atom [26]. Voronoi analysis asserts that the local ordering can be described using polyhedral structures created around each atom [27]. The polyhedron is represented by the Schlaefli notation: a vector of indices $<n_3, n_4,... ,n_v>$ where n_i is the number of polyhedron faces with i edges. The total value of n_i can be considered as the CN for each atom which can be used to differentiate between ordered and disordered structures. For instance, the amorphous CuZr phase can be described with a large fraction of five-edged faces. The Cu-centered index of <0, 0, 12, 0> has been reported as ~ 17% for a $Cu_{64}Zr_{36}$ model [28], as compared to index <0, 12, 0, 0> which represents a CN of 12 for crystalline Cu models.

2.2.3 Mechanical Properties of Amorphous Metals

While dislocations and slip are failure mechanisms in crystalline metals, shear transformation zones (STZs) are the plasticity mechanism proposed for amorphous alloys [29]. STZ can be described as a local cluster of atoms (~ 100 atoms Figure 2-2) which undergo an inelastic shear strain [30]. STZ operation requires a high amount of energy as compared to the required energy for dislocation nucleation in crystalline metals. Consequently, the STZ operation can accommodate local shear strain, and is strongly

dependent on local atomic arrangement [31]. The distribution of free volumes has been shown to have a significant impact on STZ activation energy [32] as the STZ operation is more feasible in locations with higher free volume. Free volume has been defined as a part of nearest neighbor volume for each atom in which the movement of the atom is not associated with an energy change [32].

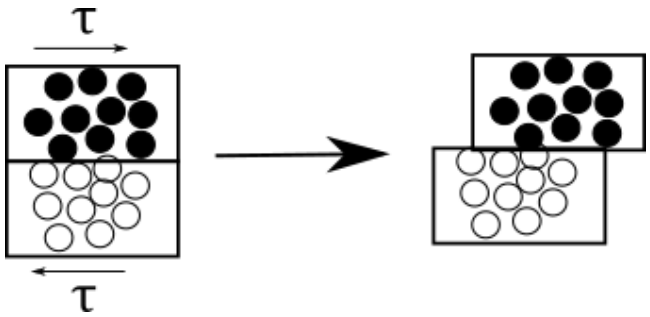

Figure 2-2: Schematic of shear transformation zone (STZ) during the deformation of amorphous alloys (adopted based on a figure in [30]).

Plastic deformation can take place in MGs by STZ operation and the accumulation of local shear strains. However, homogeneous deformation is usually associated with elevated temperatures (typically higher than $0.9T_g$) and low strain rates (typically lower than 10^{-1} s^{-1}). Meanwhile, catastrophic failure due to shear localization occurs at low temperatures [30]. Shear band is defined as a local narrow high shear strain region that is formed due to the accumulation of STZs; which occurs very quickly and results in considerable displacement (close to mm scale [33]). The effect of shear banding can be observed as "slip steps" on the fracture surface of samples.

As a consequence of shear localization, MGs usually show brittle failure under tensile loading. The brittle failure has been reported in studies of $(Cu_{0.5}Zr_{0.5})_{100-x}Al_x$ (x = 5, 6, 8) [34] and $Cu_{48-x}Zr_{48}Al_4Nb_x$ [35] BMGs under tensile loading. The brittle failure mode was

also observed in compression testing of Fe-based BMG rods [36] and for $Mg_{65}Cu_{7.5}Ni_{7.5}Zn_5Ag_5Y_{10}$ BMG [37]. Overall, the brittle failure, particularly under tensile loading, has been known as one of the most pertinent drawbacks of BMGs.

In addition, nanoindentation has also been commonly used to study the mechanical properties of MGs. Nanoindentation studies of MG alloys have several advantages compared to conventional tensile or compression testing, such as the non-destructive nature of the test and the very low penetration depth (up to few hundred nm). As a result, it is possible to study shear banding which appear as load discontinuities (pop-in) in the load-displacement curve [38]. The shear banding mechanism during nanoindentation of MGs was evident as a pop-in feature in force-displacement curves of Nb-Ni systems [39], and associated with shear localization that was obvious in atomic shear strain distribution results. Mechanical properties such as reduced elastic modulus and hardness can be also calculated from the force-displacement curve in nanoindentation testing.

2.3 MD Simulation

Classical MD is a common numerical technique which is useful in studying atomistic micromechanisms associated with the plasticity of C-A composites. Classical MD is based on classical Newtonian mechanics and is capable of performing atomistic simulation modelling with few millions of atoms and time scales up to a few ns. The corresponding time and size scale of the classical MD method makes it a powerful technique in capturing the atomistic plasticity of C-A composites.

MD is the study of the dynamic evolution of a type of N-body system [40]; which can be assessed by tracking the physical movement of atoms and molecules in a fixed period of time. Newton's equations of motion are being numerically solved to determine the trajectories of interacting atoms and molecules. The interatomic potential, or molecular force field, is required to calculate the forces between particles and their potential energies. The flow chart of the general MD algorithm is shown in Figure 2-3. The first step involves assigning an initial position (r) and velocity (v) to the atoms. Then, the atoms move for a short time interval (Δt); followed by numerical solving for Newtonian's equations of motions to calculate acceleration (a), as well as new positions and velocities. Consequently, the boundary conditions, temperature and pressure control will be applied to the system as needed. Finally, the physical quantities are calculated and the process is repeated by adjusting time and iteration step.

The time-averaged MD quantities are related to the macroscopic ensemble-based thermodynamic properties by using statistical mechanics relations [41]. The molecular level configuration of a system is called its microstate, and an ensemble is the collection of microstates that satisfy the fixed macroscopic properties of a system [42]. As a general rule, the simulation ensemble has to be selected in such a way that the corresponding constraints are comparable with those experimentally controlled properties. Canonical ensemble (known as NVT) and isothermal-isobaric ensemble (known as NPT) are two of the most common ensembles in MD simulations; particularly to study the deformation behavior of materials. The imposed constraints in the NVT ensemble are the number of particles (N),

volume (V) and temperature (T); while in NPT, the pressure (P) is constrained instead of volume. The internal energy of the system can fluctuate in both ensembles.

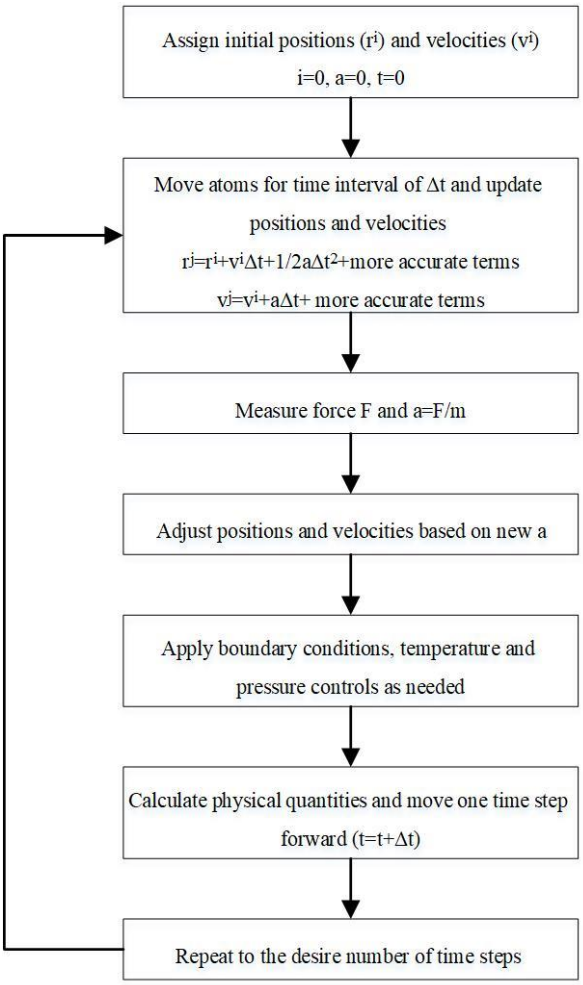

Figure 2-3: Simplified MD simulation process algorithm (adopted based on *[40]*).

2.4 Crystalline-Amorphous Cu-Zr Composites

As discussed in *Section 2.2*, the brittle failure is the main drawback of BMG alloys; which is associated with a highly localized shear deformation state known as the shear banding phenomenon [30,43]. In order to improve the ductility of BMGs, several strategies have been reported, such as introducing a high level of porosity to produce MG foams [44] and

designing MG alloys with particular elastic properties (i.e. large Poisson's ratio of 0.42) [45]. Synthesis of C-A composites is the main toughening strategy for BMGs [8], in which a secondary crystalline phase is introduced into the amorphous matrix to increase the toughness of BMGs. One of the C-A composite systems that has been studied extensively, is the binary Cu-Zr alloy which has shown high glass forming ability. The reduced glass transition temperature (T_{rg}) of the $Cu_{64}Zr_{36}$ was measured to be around 0.64 [46]; which is relatively high among corresponding values for other alloys such as Ca-Al, Ni-Nb, and Ni-Nb-Zr systems [1]. There is also a significant atomic size mismatch between Cu and Zr atoms. Based on the empirical atomic radius (~160 pm for Zr and ~128 pm for Cu), the atomic size mismatch in Cu-Zr systems is around 25 %; which is considerably higher than the minimum value for the Inoue criterion (around 12 %) [1]. Additionally, Cu-Zr binary alloys have shown a remarkable number of intermetallic compounds in equilibrium (phase diagram of Figure 2-4) due to the large negative enthalpy of mixing (~-23 kJ/mol); indicating that Cu and Zr can be mixed and vitrified easily. Figure 2-4 demonstrates the crystalline intermetallic compounds in equilibrium, including phases such as CuZr, $CuZr_2$ and $Cu_{10}Zr_7$. Due to a high glass forming ability, the Cu-Zr binary alloy has been selected as a model system in our current study to investigate the synthesis and characterization of C-A composites.

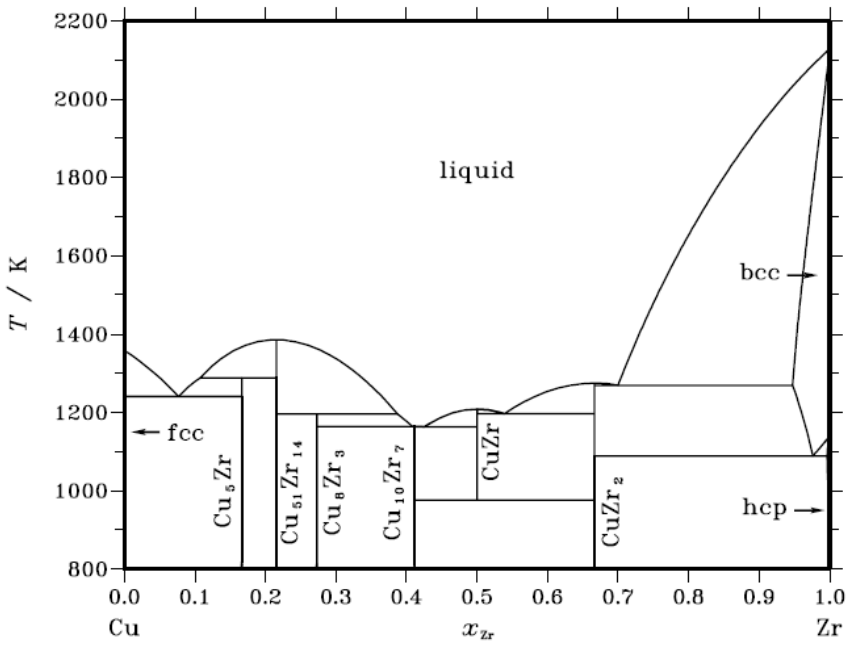

Figure 2-4: Phase diagram for binary Cu-Zr alloys (used with permission, license number 4304250357590) *[47]*.

2.4.1 Synthesis of C-A Composites

C-A composites synthesis methods can be categorized based on the initial starting phase which might be liquid (melting and quenching), vapor (sputtering) or solid (ARB). These techniques and their fundamental concepts will be reviewed in the following sections.

2.4.1.1. Melting and Quenching

The glass forming ability during melting and quenching of a metallic alloy was discussed at length in *Section 2.2.1*. The crystalline phase can be precipitated during the cooling process while the remainder can melt to form a glassy matrix. The precipitated crystalline phase usually has the dendritic morphology, such as the dendritic crystalline

$Zr_{71}Ti_{16.3}Nb_{10}Cu_{1.8}Ni_{0.9}$ phase nucleated in a glassy matrix with a composition of $Zr_{47}Ti_{12.9}Nb_{2.8}Cu_{11}Ni_{9.6}Be_{16.7}$ [8]. This study is important because it was one of the first studies which reported the successful synthesis of C-A composites with enhanced ductility. Plasma arc melting and casting copper molding have both been also used to synthesize Cu-Zr based BMG alloys (for example Zr-Ti-Nb-Ni-Cu-Be) reinforced with dendritic crystalline phases [48,49]. Several studies have shown the presence of nanocrystalline particles in BMG CuZr rods [50]. Meanwhile, synthesis of amorphous binary CuZr and nucleation of a secondary crystalline Cu or Zr phase during quenching to produce Cu-Zr C-A composites has not been reported. The reason for such can be mainly attributed to the technical limitations such as difficulties in controlling the cooling rate [1].

In spite of initial successes, there are several limitations to the synthesis of C-A composites using melting and quenching techniques. Firstly, the number of alloy systems that produced a glassy matrix with crystalline dendrites is not substantial [30]. Moreover, even in those few alloy systems, the range of compositions is limited. As it can be seen from the above examples, the composition of both glassy and crystalline phases is complex. Secondly, the precipitation of the crystalline phase is very sensitive to the cooling rate [51]. Even a slight change in cooling rate might lead to significant microstructural variations. Finally, the reported composites to date contain soft crystalline dendrites (in comparison with the hard amorphous matrix) which improved the ductility at the cost of a significant reduction in tensile strength of the glassy matrix [30].

2.4.1.2. Sputtering

Sputtering is a two-step technique: by applying a very high-energy ion field such as electron or magnetron field, the atoms are being knocked from the target surface; followed by the deposition of free atoms onto a cold substrate. The whole process occurs in a vacuum chamber in the presence of an inert gas such as argon or N_2. The distance between target and substrate is in the range of a few centimeters. Amorphous thin films can be synthesized by vapor-solid quenching during sputtering. Amorphization during sputtering is achieved by energizing the system using high energy sources (i.e. electrical or magnetic field) followed by quenching to a non-equilibrium state [52]. The structure of co-sputtered, or multilayered films, is strongly dependent on the substrate temperature and other deposition parameters such as adatom mobility during condensation and the heat of mixing [53]. Adatom mobility is closely related to the surface diffusion; and can be estimated from the kinetic energy of condensed particles. Heat of mixing (or enthalpy of mixing) is defined as the enthalpy which is released or absorbed upon compound mixing [54]. The enthalpy of mixing can be negative (when the mixture has a lower enthalpy than the pure compounds) or positive (when the mixture has a higher enthalpy than the pure compounds). Negative enthalpy of mixing (which reduces the Gibb's free energy) is required in order to form an amorphous phase during sputtering [53].

Magnetron sputtering has been extensively used in the synthesis of C-A nanolaminates due to the high deposition and ionization rate [55]. For instance, Cu-CuZr nanolaminates have been deposited on Si substrates using magnetron sputtering [56]. In addition, TEM analysis

indicated that the mixing behavior of Cu-Zr and Ti-Zr systems were different during the co-sputtering process [53]. While the Cu-Zr system (with large negative enthalpy of mixing ~ -23 KJ/mol) has shown amorphous characteristics, the nearly zero enthalpy of mixing has made the vitrification of Ti-Zr difficult. Although the application of sputtering techniques is beneficial in the synthesis of C-A thin films (with few μm thicknesses), preparation of bulk sputtered C-A composites is still challenging due to the technical limitations, i.e. atomic layer by atomic layer deposition process. Moreover, the multilayered structures are the most commonly synthesized composites, prepared using sputtering techniques.

2.4.1.3. Accumulative Roll Bonding

The ARB typically includes a repeating "roll and fold" process in which a multilayer sandwich stack is prepared and then rolled to a specific strain (or thickness reduction) to ensure bonding. Then, the rolled sample is cut in half and folded again to repeat this procedure. The surface treatments, e.g. surface roughening and cleaning, and intermediate modifications such as heat treatment typically have been used in the ARB process. This ARB process was firstly developed by Saito *et al.* [57] for synthesis of ultrafine grain materials.

The deformation and bonding mechanisms of a binary system during the ARB procedure can be explained based on the plastic instability, caused by the differing properties of each phase. In case of bonding a soft and a hard layer, the harder phase experiences necking (due to flow properties mismatches) during the high thickness reduction process [58–60].

Necking is referred to as a plastic instability when a large amount of tensile strain is localized in a small region, causing a significant decrease in local cross-sectional area. As a consequence of necking, the hard phase begins to fracture into small pieces and distributes in the form of particles inside the soft phase. The soft phase can flow and penetrate into the adjacent layer; which is known as the metallic strips bonding mechanism.

There are different parameters including percent thickness reduction, initial multilayers thickness ratios and surface treatment which have all shown significant influences on multilayer bonding during the ARB process. The percent thickness reduction has been investigated for several metallic systems, such as Cu-Cu, Cu-Ni, and Cu-Fe [61]; as well as Al-stainless steel, Cu-stainless steel, and mid steel-stainless steel [62]. These studies revealed that a minimum thickness reduction percentage is required to achieve strong bonding during the ARB process. A minimum thickness reduction varies for different alloy systems. However, such a practical range of percent thickness reduction has not been reported for the Cu-Zr system as of yet. The effects of multilayers thickness ratios have been also studied for different systems, including Cu-Zn-Al, Fe-Ag and Ni-Ag [58,63,64]. The key conclusion in these studies was that the plastic instability during the ARB process is strongly influenced by the multilayer thickness ratio. Similar studies on the influences of the Cu-Zr thickness ratios on multilayers bonding during the ARB process are missing and warrants further investigation.

Another important parameter in roll bonding of metallic sheets is the surface treatment, such as cleaning and surface roughening, before rolling. Previous data have demonstrated that the aluminum strip bonding strength can be increased almost 3 fold by roughening the

surface from ~ 2.5 µm to ~ 4.5 µm [65]. It has been demonstrated that surface preparation methods such as degreasing in acetone, scratch-brushing of surfaces as well as oxide contamination considerably influence Al strip bonding. Scratch-brushing causes surface embrittlement, and consequently, surface cracking can occur due to the hardness mismatch between the surface and underlying layers. The presence of such cracks on the surface facilitate the intimate contact and bonding of strips.

The mechanisms of solid state amorphization during the ARB process is related to increasing the Gibbs free energy, departing from an equilibrium state and quenching the system to a frozen state [66]. Accumulation of defects such as dislocations and stacking faults along with continues grain size reduction are all sources of increasing free energy in systems [67]. Figure 2-5 indicates the pathway of phase transformation during solid state amorphization. As it is shown schematically, the free energy of a system can be raised to a level higher than the corresponding energy level of the amorphous metastable phases due to structural defects. It is possible to form the amorphous phase while transferring the system from a high energy level to a lower one via mechanical alloying.

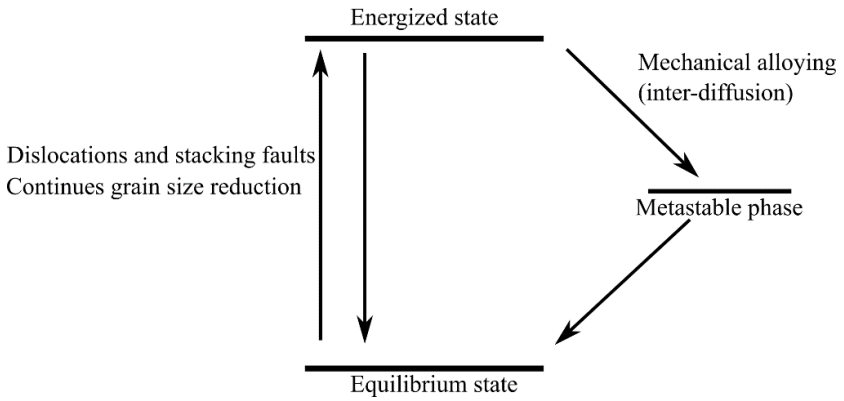

Figure 2-5: Energy pathway during energizing and quenching of metastable phase formation (adopted based on a figure in *[66]*).

The main atomistic mechanism in solid state amorphization is the inter-diffusion of elements during the mechanical alloying procedure. The diffusivity of elements at the interface of layered structures can increase as a result of crystalline defects (dislocations and stacking faults) and grain size refinement [66]. Although the ARB process is performed at room temperature, there is a slight change in temperature during rolling which increases the rate of diffusion.

The ARB method has introduced important advantages including simple procedure and low cost which makes this technique attractive for the synthesis of C-A composites. Additionally, there is no significant restriction in size of the synthesized samples using the ARB method. As a result, the application of the ARB technique is beneficial for the synthesis of bulk C-A composites.

Ohsaki *et al.* [10] have shown that the amorphization in highly pure Cu-Zr multilayered strips carried out using the ARB technique at room temperature. Five layers of Cu and four layers of Zr (with purity of ~ 99.8 %) were stacked, followed by 9 rolling and folding passes on the sandwich multilayers; with an average thickness reduction of 75 % after each cycle. While intermediate annealing or heat treatment procedure has not been reported, the high resolution TEM imaging have shown the amorphization of CuZr phases at the Cu/Zr layer interface after 9 ARB passes [10]. In a more detailed manner, the amorphous CuZr regions have been formed just in a narrow area with thickness of less than 1 nm at the interfacial regions after 9 ARB passes. The amorphization mechanism was inter-mixing of Cu and Zr atoms at the Cu-Zr interface. Furthermore, neither alloying nor amorphization were reported in early steps of the ARB process. The TEM analysis on similar multilayer Cu-Zr

sandwich stack, performed by Sun *et al.* [9], did not show either the formation of CuZr phases nor amorphization during the ARB process. As mentioned earlier, the purity level of Zr sheets has significant influences on their mechanical properties [11]. The main differences (in terms of composition and mechanical hardness values) between highly pure and commercially available Zr sheets have been summarized in Table 2-1.

Table 2-1: Differences in composition and mechanical hardness values for highly pure and commercial Zr sheets [11].

High purity Zr (Wt ppm)	Zr (%)	C	Fe	Al	Hf	N	O	Hardness (Hv)
	99.8	22	<50	<20	35	<20	<50	160
Low purity Zr (%)	Zr+Hf	C	Fe+Cr	H	Hf	N	O	Hardness (Hv)
	99.2	<=0.05	<=0.2	<=0.005	<=4.5	<=0.025	<=0.16	196

In addition, the application of such Zr sheets with high purity content is limited to the laboratory scale due to their high manufacturing cost. As discussed in introduction, the large hardness mismatch between commercially available Cu and Zr sheets (the hardness values for highly pure and commercial Zr sheets are indicated in Table 2-1) makes the co-deformation difficult and consequently, achievable number of ARB passes can be limited. Such reported results arise important questions needed to be answered, including; i) what ARB parameters might lead to the formation of CuZr intermediate phases; and ii) in which conditions would the amorphization occur for the ARB process in commercially available Cu-Zr systems. The current research aims to answer these important questions by providing

an ARB guideline for the synthesis of cost-effective C-A composites based on commercially available Cu-Zr multilayers. The effects of annealing on both alloying and amorphization during the ARB process of commercial Cu-Zr multilayers, which were not addressed in above-mentioned studies, are also aimed in this research.

2.4.2 Mechanical Properties of C-A Cu-CuZr Composites

Generally, C-A composites can be classified as bulk and nanolaminates based on the method in which it is synthesized. Bulk samples were mainly synthesized by melting and quenching, and the ARB techniques while the nanolaminates were synthesized using magnetron sputtering. As the main focus of this research is the ARB samples and MD simulation of nanolaminates, the mechanical properties and failure mechanisms of both bulk Cu-Zr composites synthesized by the ARB technique and C-A Cu-CuZr nanolaminates will be briefly reviewed.

2.4.2.1. Bulk C-A Cu-Zr Composites

The mechanical properties of C-A Cu-Zr composites synthesized by the ARB technique have been studied by carrying out tensile and indentation tests. For instance, experimental tensile data have shown the ductility enhancement from ~ 8 % to ~ 14 % after 6 ARB passes on a multilayer Cu-Zr sandwich stack [9]. However, by further increasing the number of rolling cycles, the ductility decreased. The inhomogeneous microstructure and the strength mismatch in the Cu and Zr layers were claimed as the main cause of cracking at the

interface. This property mismatch between two elements were reduced by increasing the ARB cycles to 6, leading to enhanced ductility. Vickers hardness testing has also been performed by Ohsaki *et al.* [10], with the results showing an improvement in hardness for the Cu-Zr multilayers from ~ 160 Hv to ~ 300 Hv after 10 ARB passes. Furthermore, the nanoindentation studies on C-A Cu-Zr composites synthesized by the ARB process - which is the second objective of this research - has not been reported in the literature as of yet.

2.4.2.2. C-A Cu-CuZr Nanolaminates

A summary of the important findings from both experimental characterizations and numerical MD method, used to study the mechanical properties of Cu-CuZr nanolaminates, will be discussed in the following section.

2.4.2.2.1. Experimental Studies

Different thicknesses (ranging from 1 to 200 nm) of crystalline Cu- amorphous $Cu_{60}Zr_{40}$ samples have been synthesized using magnetron sputtering [68]. The work of Zhang *et al.* [68] noted improvements from ~ 1.8 GPa for pure Cu to values of ~ 6.3 GPa for nanoindentation hardness in C-A multilayer composites. Based on the reported failure mechanisms, dislocation nucleation occurred in the Cu layer initially and propagated toward the C-A interface. When the dislocation met the interface, STZ activities were triggered in the amorphous CuZr layer due to dislocation pile up. Dislocation pile up refers to a situation where many dislocations are generated on the same slip plane, and the leading dislocation is blocked due to the presence of a barrier such as an interface or grain

boundary. Dislocations will pile up behind the leading one, triggering STZs in the amorphous layer.

Tensile elongation of sputtered crystalline Cu- amorphous Cu_3Zr nanolaminates have shown improvements of almost 14 % [7]. The thickness of the amorphous layer was around 5nm; and the nanocrystalline Cu layers were sputtered with an average grain size of ~ 35 nm. A different failure mechanism has been reported by Wang *et al.* [7] in which TEM images did not show a heavy dislocation pile up at the interface and the shear banding was not seen in the amorphous layer. The C-A interface was acting as the dislocation source and sink, leading to a uniform deformation state at the amorphous layer which enhanced the composites toughness.

Cui *et al.* [56] performed nanoindentation and TEM analysis on a deposited multilayered Cu-CuZr composite, which showed a transition from the plastic co-deformation (for ~ 4 nm CuZr thickness) to a shear induced instability (for ~ 100 nm thickness in the CuZr layers). Co-deformation occurred as a result of STZ nucleation in the amorphous CuZr layer due to dislocation pile up at the C-A interface; while nucleation and propagation of shear bands were the main causes of shear instability. Propagation of shear bands in the amorphous layers, which were parallel to the slip plane in crystalline Cu layers (slip plane in FCC metals is {1 1 1}), led to shear localization that was observed in C-A composite systems with a thick CuZr layer.

Absorption of dislocations at the interfacial regions of Cu-$Cu_{60}Zr_{40}$ nanolaminates with individual layer thicknesses of ~ 50 nm, has been observed during experimental micro-compression tests [69,70]. The presence of a C-A interface acted as an obstacle which

prevented dislocation motion and hence, led to an improvement in composite compressive ductility. The TEM and atom probe morphology analysis also demonstrated the coincidence of dislocation and shear banding at the Cu –$Cu_{54}Zr_{46}$ C-A multilayers interface [71,72]. The coincidence of the dislocation slip in the Cu layer and the shear band in the CuZr layer, resulted in a more uniform shear deformation. However, studies on nanolayered Cu-CuZr micropillars, carried out by Liu *et al.* [73], revealed a homogeneous deformation that was responsible for the superplastic-like deformation in multilayer structures. This is in contrast to other studies which investigated crystalline Cu – amorphous $Cu_{60}Zr_{40}$ nanolaminates and observed suppression of shear banding at the interfacial regions [13,74].

2.4.2.2.2. MD Simulations

Although experimental techniques are useful in microstructural analysis, there are several limitations in conducting experiments for the purpose of detecting atomistic characteristics. For example, the prepared samples for SEM or TEM analysis are just representative of a local area which might not reflect the bulk features of the sample. Additionally, some micromechanisms, such as dislocations and shear bands, are not easily detected using these techniques. Consequently, numerical MD has been used extensively in the study of Cu-Zr system microstructures. For instance, MD simulations on a multilayer crystalline Cu-amorphous $Cu_{75}Zr_{25}$ structure with amorphous intergranular films revealed that the absorption of dislocations was apparent at the interfacial regions [75]. The size of the sample in this study was ~ 70 × 32 × 9 nm along X, Y and Z axis, respectively - with an

average number of ~ 1,600,000 atoms. Due to the presence of the C-A interface, both crack nucleation and propagation were retarded; which was responsible for higher values for ductility and fracture toughness. Simulated the tensile loading on a Cu-CuZr model (with size of ~10 × 15 × 10 nm, and ~ 105,336 atoms) , Wang *et al.* [7] demonstrated that STZs can be nucleated at the C-A interface upon dislocation absorption. The disregistry vector (relative atomic displacement across a separating plane) analysis, performed by Brandl *et al.* [76], indicated the co-existence of dislocation activities and STZs at the C-A interface under shear loading. A Cu-$Cu_{46}Zr_{54}$ multilayer model, with a sample size of ~ 26 × 5 × 34 nm and ~ 300,000 atoms, was used in this study. The sliding phenomenon at the C-A interface was observed in MD simulation of Cu-$Cu_{46}Zr_{54}$ models (with model size of ~ 20 × 15 × 20 nm) due to the STZ plasticity; which led to dislocation nucleation and propagation at the interface [77]. This is in well agreement with results reported by Cheng and Trelewicz [78] who showed that the impinging of STZs at the C-A interface of a 10 nm crystalline Cu – 5 nm amorphous $Cu_{64}Zr_{36}$ model can trigger dislocation nucleation by reducing the activation barrier.

The key observations in the aforementioned experimental and numerical studies was to investigate the interaction between the crystalline and amorphous phases. In spite of contradictions in previous studies, the overall conclusion is still valid in that the C-A interface plays a vital role in the enhancement of mechanical properties of metallic C-A composites. Enhancement can occur through absorbing dislocations or by blocking shear band propagation. However, it is not clear which failure mechanisms govern the plasticity of C-A composites as there are contradictions on the initiation of STZs or dislocations.

Furthermore, the C-A interface is a relatively new type of defects in comparison with other defects such as grain boundary and free surface. The effects of crystalline characteristics at the interface, especially crystalline orientation on the mechanical behavior of C-A composites, has not been studied as of yet. As a result, to fully understand the effects of C-A interface on the failure mechanisms, some questions still require answers. Specifically, which failure mechanisms (dislocation nucleation or STZs) occurs first? What are the influences of parameters such as interface structure and crystalline orientation in the activation of yielding mechanisms? As discussed in *Section 2.3*, MD is a powerful technique in capturing the atomistic micromechanisms associated with the plasticity of C-A composites. Therefore, the numerical MD analysis in the current work aims to find answers to above-mentioned questions.

Chapter 3 : Methodology

Chapter 3 is assigned to describe details related to both experimental and numerical methodologies used in the current study. Experimental details include materials selection, synthesis (ARB procedures), characterization techniques (electron microscopy) and mechanical testing; all of which will be discussed in the first section. Details related to the MD simulations, such as model construction, relaxation processing, data extraction and analysis will be explained in the second section of this chapter.

3.1 Experimental

3.1.1 Sample Preparation

3.1.1.1. Materials Selection

Crystalline Cu and Zr sheets were purchased from ThyssenKrupp Materials NA and United Titanium suppliers, respectively. Based on the data sheet provided by the ThyssenKrupp Materials NA supplier, the Cu sheets were highly pure (~ 99.99 %). On the other hand, the Zr sheets were supplied with a purity of around 99.2 % as per the supplier specifications. The details of both as-received Cu and Zr sheets compositions are provided in Table 3-1.

The thickness of as- received Cu and Zr sheets were 508 µm and 711 µm, respectively. All the samples were prepared from the same batch of sheets.

Table 3-1: Composition of the as-received Cu and Zr materials based on the supplier's data sheet.

Cu sheet	Cu (%)	Ag	S	Fe	Pb	Ni	O
(ppm)	99.99	25	15	10	5	10	5
Zr sheet	Zr+Hf	C	Fe+Cr	H	Hf	N	O
(%)	99.2 to 100	<=0.05	<=0.2	<=0.005	<=4.5	<=0.025	<=0.16

3.1.1.2. Sample Synthesis Protocol

The ARB procedure was carried out using a 50 Ton STANAT rolling machine. The protocol for sample preparation was as following:

1. Crystalline Cu sheets with two different thicknesses of 300 and 250 µm were prepared from the as-received sheets by rolling the sheets from the initial 508 µm to the desired thicknesses. Similarly, crystalline Zr sheets with a thickness of 110 µm were prepared by rolling the as-received sheets from 711 µm to 110 µm. In order to recover the mechanical properties, the 110 µm Zr sheets were annealed at 1000 ^{o}C for 120 minutes after the rolling procedure.

2. The prepared Cu and Zr sheets were cleaned by putting them in acetone for about 5 minutes.

3. The surface of Cu and Zr sheets were scratched using a steel wire brush. The importance of wire brushing on the multilayer bonding during the ARB process was discussed in *Chapter 2*. The effects of brushing on the surface of samples were monitored by means of surface characterizations that will be discussed in *Chapter 4*.

4. After brushing, a sandwich multilayer (4 layers of Cu and 3 layers of Zr) was prepared so that the thicker Cu sheets (~ 300 µm) were located in the outer layers, and the thinner Cu (~ 250 µm) and Zr sheets were placed in the middle of the sample in an alternate fashion. Details of thickness selection and ratios will be explained in *Chapter 4*. Figure 3-1 shows the schematic of a sandwich multilayer and the corresponding thicknesses.

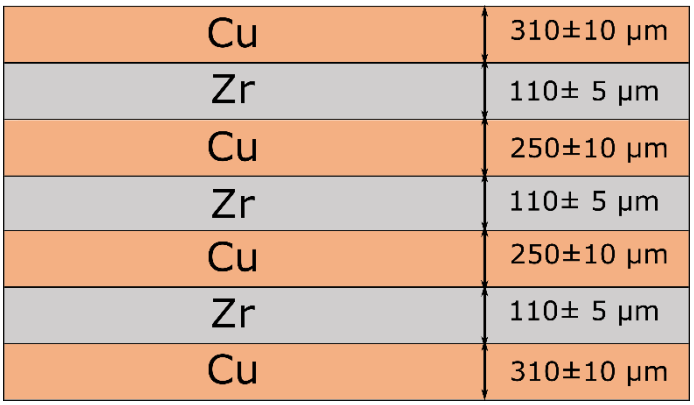

Figure 3-1: Schematic of multilayer sandwich specimen prepared for the ARB process.

5. In order to avoid sliding during the rolling process, 4 holes were made on the edge of the stacking layers, and then the layers were tightened to each other using wire strips as indicated in Figure 3-2. These wire strips were taken out by cutting the edge of the samples after the rolling step.

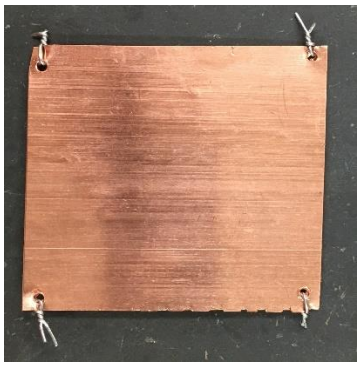

Figure 3-2: Multilayer sample tightened with steel wire.

6. After preparation of the multilayered sandwich sample, the sample was rolled to obtain at least a ~ 50% thickness reduction. The most efficient thickness reduction was noted to be between ~ 49 to 62%, which will be discussed in detail in *Chapter 4*. Considering that the total thickness of the initial sandwich multilayers was 1430 µm, the thickness of the sample after rolling should be lower than 715 µm to ensure a 50% thickness reduction. The gap between rollers was adjusted as ~ 0.120 mm to achieve a minimum 49% reduction.

7. After rolling, the edge of the samples were cut to remove the wire strips as well as the edge cracks. Then, the annealing procedure was carried out on the roll bonded sample using a Carbolite Gero furnace. The annealing temperature were set to 350 ^{o}C and 700 ^{o}C for a time range of about 60 to 90 minutes (details of annealing temperature and time as well as effects of oxidation during annealing will be covered in *Chapter 4*). To minimize oxidation effects, the samples were wrapped by steel sheets. The first rolling pass was completed after step 7.

8. Following the heat treatment, the samples were cut in half and the procedure from step 2 to step 7 was repeated for the desired number of rolling passes.

Figure 3-3 indicates the schematic procedure of a complete ARB pass used in the current study.

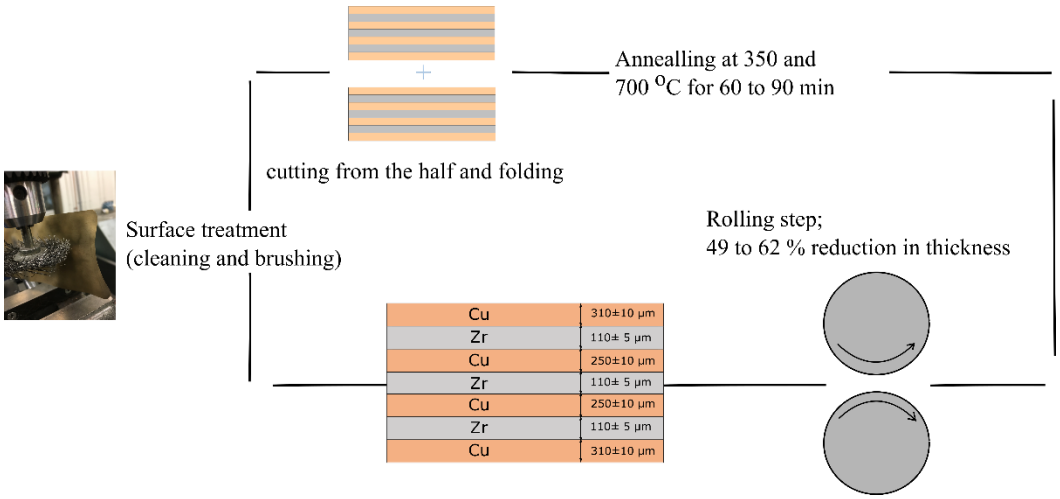

Figure 3-3: Schematic view of the ARB procedures.

3.1.2 Materials Characterizations

In order to investigate the microstructure of synthesized samples, two main electron microscopy techniques, SEM and TEM, were used. Mechanical testing was performed using nanoindentation experiments.

3.1.2.1. Scanning Electron Microscopy

In order to study the phase distribution and surface morphology such as micro-defects, a JEOL JSM-5900 LV SEM was used. The spot size variation was set at ~ 30 to 40 and the beam voltage was set to 10 to 20 V depending on the samples characteristics such as surface quality. Both secondary and back-scattered electron detectors were used in imaging the

surface and cross-sectional area of the samples. A mounting and polishing procedure was performed to prepare the samples for the SEM analysis based on recommendations in [79]. The samples (either cross section or surface) were mounted using a high pressure high temperature mounting machine. The chemo-mechanical polishing procedure was carried out by using a rough (1200) sand paper and gradual shifting to smoother 6 and 1 micron clothes. Distilled water was used as a lubricant during rough grinding. A diamond suspension was applied for the 6 micron cloth, and final polishing alumina (0.05 μm) was used for the 1 micron cloth for the smooth polishing process. After polishing steps, the sample was washed carefully with methanol and distilled water. Finally, after sonicating in an ultrasonic methanol bath for about 15 minutes, the sample was prepared for SEM imaging.

3.1.2.2. Transmission Electron Microscopy

TEM was used in this study to identify the phase structures of the synthesized samples. The TEM analysis was conducted using a FEI Talos F200X; and post processing was performed using TEM image analysis (TIA) Software. TEM sample preparation was carried out on a surface side and based on the procedure described in the following: a disk shape sample of 3 mm diameter and 100 μm thickness was prepared. A grinding procedure, called dimpling, was used to create an area in the center of the disk-shape sample with a thickness of 50 μm. After that, electro polishing was carried out based on recommendations in [80] to create one, or several holes with a diameter of several μm inside the thin region. Usually, a tiny area with a thickness of several nm might be created at the edge of these holes, which is

then used for TEM analysis. Electron diffraction analysis were conducted with TEM to identify the phase structure of the samples.

3.1.2.3. Energy-Dispersive X-ray Spectroscopy

Energy-dispersive X-ray spectroscopy (EDS or EDX) analysis was conducted along with both SEM and TEM studies. The composition variation, through line or within an area, was captured by doing line and area scan, respectively. After the imaging procedure in both the SEM and TEM modes, the images were imported in TEAM (Texture & Elemental Analysis Microstructure) software and EDS analysis were performed on the desired regions by assigning the lines and areas accordingly.

3.1.2.4. Electron Backscatter Diffraction

Electron backscatter diffraction (EBSD) is a strong instrumentation technique used in capturing the surface morphology and particularly, used to investigate grain size and texturing. EBSD technique is sensitive to the surface quality of sample and therefore, a three-step process was applied to prepare the cross-sectional area of the samples for EBSD analysis. The sample preparation process was based on recommendations in [81]; and include chemo-mechanical polishing, vibro-polishing and ion milling. After chemo-mechanical polishing, which was mentioned earlier in *Section 3.1.2.1*, the sample was polished for about 12 hours in a vibration polishing machine containing a 0.5 µm polishing clothe and colloidal silicon polishing suspension (50-70 nm). Followed by sample cleaning in an ultrasonic methanol bath, the sample was polished for an additional half an hour using an ion milling process to condition the sample for EBSD analysis.

The EBSD analysis was performed on the cross section of the samples after its 2nd, 4th, 6th and 8th rolling steps. This analysis was carried out using a FEI Nova NanoSEM 450 machine by tilting the sample at about 70°. Post processing was performed by two software packages, TEAM and OIM (Orientation Image Microscopy).

3.1.2.5. Nanoindentation

The reduced elastic modulus and hardness were measured using a Hysitron TI 750 Ubi NanoIndenter with Berkovich tips. The nanoindentation testing was performed on mounted and polished samples as described in *Section 3.1.2.1*. All tests were conducted based on the standard trapezoid load function shown in Figure 3-4 in load control mode. All the tests were conducted at room temperature. The maximum force was set to 8000 µN and the results were extracted using the Hysitron software.

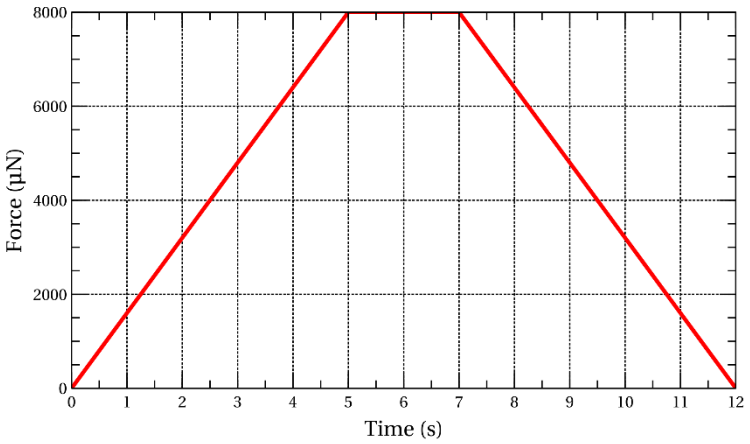

Figure 3-4: Standard trapezoid load function in nanoindentation testing.

The hardness (H) and reduced elastic modulus (E_r) were extracted from the nanoindentation force-depth curve (shown schematically in Figure 3-5) according to Equation 3-1 and Equation 3-2.

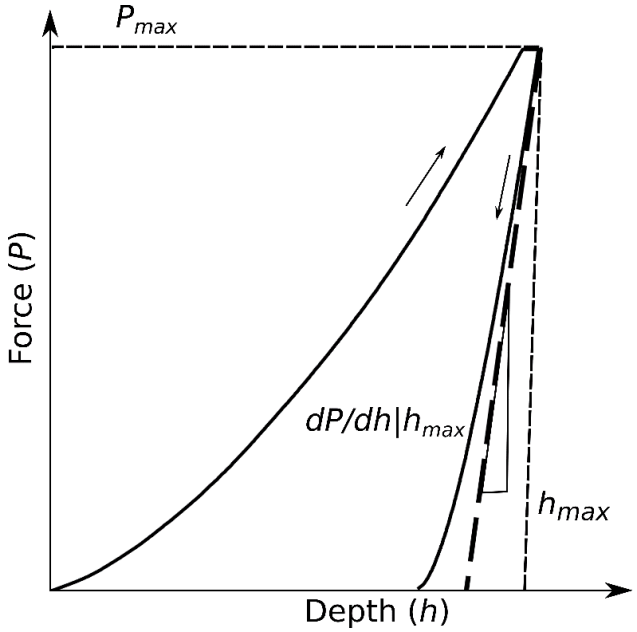

Figure 3-5: schematic view of the nanoindentation force-depth curve (adopted based on *[82]*).

$$H = \frac{P_{max}}{A(h_c)}$$ Equation 3-1

$$E_r = \frac{\sqrt{\pi}}{2\sqrt{A(h_c)}} dP/dh|h_{max}$$ Equation 3-2

In these equations, P_{max} is the maximum force; $A(h_c)$ is the contact area which is a function of contact depth (h_c); and $dP/dh|h_{max}$ is the slope of unloading curve at the maximum indentation depth (h_{max}). These parameters, P_{max}, h_{max} and $dP/dh|h_{max}$, are shown in a schematic view in Figure 3-5. Details related to measuring the contact area and contact depth can be found in [82].

3.1.2.6. Surface Roughness Measurement

Surface roughness was also measured using the Alpha step instrument. The roughness measurement was conducted based on the ASTM-D7127 standard on two samples: one before and the other one after brushing. Roughness testing was performed at 5 randomly

chosen locations on each sample. The roughness was measured as the difference between the maximum peak and minimum valley through a 2 mm line scan for each test. The average roughness was calculated using the 5 sampled locations for each sample.

3.2 MD Simulation

MD simulation was used to study the ARB process of the Cu-Zr multilayer, and the tensile behavior of C-A composites. The purpose of MD analysis is to complement the experimental studies and investigate the micromechanisms. The simulations set up in the current research will be summarized in the following sections.

3.2.1 Embedded Atom Method Potential

As mentioned in *Chapter 2*, an interatomic force field or potential is required to measure the force between atoms. One of the most common potentials used in metallic systems is the embedded atom method (EAM) potential. The general form of EAM potential is shown in Equation 3-3.

$$E_i = F_\alpha\left(\sum_{i \neq j} \rho_\beta(r_{ij})\right) + \frac{1}{2}\sum_{i \neq j} \varphi_{\alpha\beta}(r_{ij}) \qquad \text{Equation 3-3}$$

Where F_α is an embedding function that represents the energy required to place atom i of type α into the electron cloud; ρ_β is the contribution to the electron charge density from atom j of type β at the location of i; r_{ij} is the distance between atoms i and j; and $\varphi_{\alpha\beta}$ is the pair-wise potential function. E_i in this equation is the potential energy of an atom i.

As it is clear from the EAM formula, the measuring energy of a single element system such as the pure Cu requires three scalar functions that include: embedding, pair-wise interactions and electron cloud contribution functions. In a binary alloy such as CuZr, seven scalar functions should be specified: two embedding functions, two electron cloud contributions and three pair-wise functions for Cu-Cu, Cu-Zr, and Zr-Zr. Herein, the EAM potential introduced by Mendelev *et al*. [83] has been used to define the interatomic potential functions for both the crystalline Cu and amorphous CuZr models. Experimental data (i.e. T_g, liquid density and enthalpy of mixing at 1500 K) has been used to calibrate this EAM potential for liquid and amorphous $Cu_{64.5}Zr_{35.5}$ alloys. Specifically, T_g was measured as ~ 770 K by using this potential, which is close to experimental values of ~ 737 K for this composition [83]. Moreover, previous studies, extensively applied this potential for modeling the mechanical deformation of amorphous CuZr models [84–86].

3.2.2 Simulation Models and Procedure

MD simulations were performed using Large-scale Atomic/Molecular Massively Parallel Simulator (LAMMPS) [87]. Numerical studies include the ARB process and tensile modeling. Details of the different MD models and the set up for each study will be explained in the following sections.

3.2.2.1. ARB Models

An atomic model of the sandwich multilayer containing single crystalline Cu and Zr layers was created and is shown in Figure 3-6. The size of model was ~ 25 × 8.5 × 40 nm along X, Y and Z directions, respectively - with ~ 528,000 number of atoms. The ARB process

was simulated by compressing the model in the Z direction with a uniform strain rate of 0.01 m/s up to 50% of the initial model thickness (dimension of the model in the Z direction is considered the thickness). A fully periodic boundary condition (along all three directions) was applied during the ARB simulation, and the shrinkage was allowed in all lateral directions (X and Y) to keep the overall volume of the model constant in response to the deformation along the Z axis. Figure 3-6 shows one step in the deformation of the sample with a thickness reduction of 50%. Similar to the experimental procedure, the models were cut in half and folded on top of each other for the next cycle of deformation. This procedure was repeated for 6 cycles. The simulation was performed at a temperature of 300 K using a NVT ensemble.

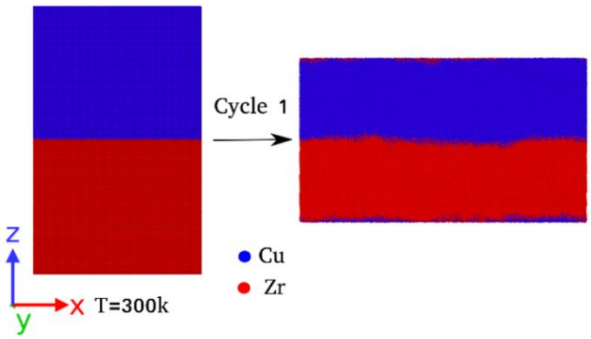

Figure 3-6: Schematic of a MD multilayer model and the first cycle of accumulative rolling simulation.

3.2.2.2. Tensile Models

In the current study, the amorphous CuZr models with a composition of $Cu_{63}Zr_{37}$ were created using a melting and quenching process. Firstly, the corresponding elemental composition was created by randomly deleting some atoms in a pure Cu model and

replacing them with Zr atoms. After that, the model was melted at 2000 K for about 250 ps (equal to 50,000 MD time steps). The model was cooled down to 10 K in a three-step process. Firstly, it was cooled down to 1000 K in a rapid cooling rate step (4 K/ps). To ensure that amorphization occurs, the cooling process around the T_g should be slow enough. Considering the T_g of CuZr, which is near to 750 K [83], a low cooling rate of 0.12 K/ps was applied in the temperature range between 1000 and 700 K. Finally, the final step of cooling was performed from 700 to 10 K using a cooling rate of 1.38 K/ps.

In order to optimize the time and cost of numerical simulations, different configurations of atomic models were created; which include C-A and polycrystalline amorphous-crystalline-amorphous (A-NC-A) models. The different model sizes were created by cropping the well quenched amorphous model. Figure 3-7 demonstrates a schematic of two representative models used in this study. Figure 3-7 (a) indicates a typical C-A model with the size ~ 20 × 2.6 × 20 nm in X, Y and Z directions, respectively. The crystalline layer in these C-A models have different orientations which imposes slight differences in model sizing along the Z direction to achieve the periodic boundary condition. The relatively small size of the C-A model (typically 76000 to 79000 number of atoms depending on the crystalline orientation) reduces the simulation time and processors, and therefore, it is suitable in measuring interface energy (γ_{int}) and critical resolved shear stress (*CRSS*).

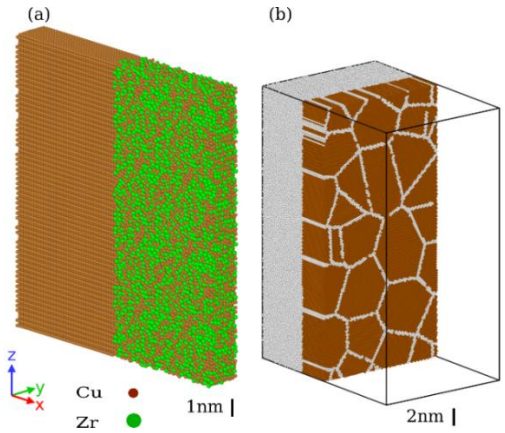

Figure 3-7: Representative atomistic structure of the (a) C-A model and (b) A-NC-A model with a polycrystalline layer. The model in (b) is sliced in the middle to show the atomistic configurations of the polycrystalline layer. The atom color corresponds to the atom type in (a) and common neighbor analysis (CNA) in (b).

The orientation of the Cu layers in both C-A models were assigned in such a way that the Y direction had a [1 -1 0] orientation and the other two axis (X and Z) were varied from [1 1 0] to [0 0 1] in an orthogonal coordination system. In addition to the crystalline orientation, the effects of the grain boundary and texturing on the failure mechanism were investigated by creating two polycrystalline A-NC-A models. Figure 3-7 (b) shows the cross section representation of a A-NC-A model with polycrystalline Cu layer. In these models, the columnar polycrystalline Cu models textured along the <0 0 1> and <1 1 1> orientations in the X direction were constructed using the Voronoi tessellation method [88]. The average grain size in the columnar polycrystalline Cu models was around 7 nm, and the size of the Cu layer was ~ 10 nm along the X axis; with variations due to texturing orientations. The total number of atoms was ~ 1,600,000 and the size of the model was ~ 28 × 20 × 40 nm in the Cartesian coordination system.

The atomic models need to be well relaxed thermodynamically in order to avoid any huge fluctuation in the results. Hence, a heating and quenching process were employed in all

models as a relaxation procedure. The model was at a temperature of 1000 K for 1 ns and then cooled down to 10 K at a cooling rate of 0.5 K/ps. The final relaxation step was carried out at 10 K and zero pressure for about 100 ps in an isothermal-isobaric (NPT) ensemble.

During the relaxation procedure and while measuring the interface energy as well as *CRSS*, the fully periodic boundary conditions were applied. However, in simulating the tensile deformation of polycrystalline A-NC-A models, both periodic and free surface (shrink-wrap) conditions along the X axis were applied to capture the effects of the boundary conditions on potential failure mechanisms. In order to simulate the condition of tensile deformation in thin films along the Z direction, shrinkage along the X axis is required. To satisfy this condition, the simulation cell remained constant in tensile deformation for both C-A and polycrystalline A-NC-A models. All tensile loading was carried out in a Noose-Hoover thermostat under canonical ensemble (NVT) at a temperature of 10 K and constant strain rate of 10^{-4} /ps along the Z direction.

3.2.2.3. Interface Energy

Equation 3-4 was used to calculate the interface energy of the C-A models with different crystalline orientations.

$$\gamma_{int} = (E_{C-A} - E_{crys} - E_{amorph})/S_{int} \qquad \text{Equation 3-4}$$

In this equation, E_{C-A} is the summation of potential energy in a well-relaxed C-A model for all atoms and will be referred to as the total energy in the current study. The terms E_{crys} and E_{amorph} are the total energy of the bulk form of the crystalline and amorphous layers before joining together, respectively. The fully periodic boundary conditions were applied

in all C-A, crystalline and amorphous models while measuring the energy. Also, the same heating and quenching procedures that were discussed in the previous section were applied in relaxation of the whole models. S_{int} is the interface cross-sectional area. The state of being well relaxed was carefully monitored by tracking the total energy of the system and its variations. If the total energy converged to a plateau, the model was considered to be a well relaxed model.

After measuring the interface energy in the C-A models, the effects of orientation on free surface energy (γ_{sur}) in the crystalline Cu layers was investigated, and the results compared. To do this, the free surface energy in the crystalline layer was measured as the difference in total energy of system with two different boundary conditions: one fully periodic and the second with a free surface (shrink-wrap) along the X dimension. Finally, considering slightly differences in the model size with different orientations, the observed free surface energy was normalized by the surface area to be comparable with values obtained from the different models.

3.2.2.4. Atomic Structural Analysis

The atomic structural analysis was performed by measuring several parameters such as atomic density, composition, RDF and Voronoi analysis. A slicing procedure was conducted in the atomic structural analysis. A region around the C-A interface with 4 nm thickness was selected in such a way that covers approximately half of the crystalline and half the amorphous layers; with the original interface position defined as the reference (X=0) point. The sectioned regions were selected in such a way that represent the structural

variation around the interface. Around 40 slices, with thicknesses of 1 nm in the X direction, were created starting from X= -20Å. More specifically, the first slice was located within -20 Å< X < -10 Å, and subsequently, the next one was shifted to the right with an increment of 1 Å (-19 Å< X < -9Å). This procedure was repeated up to X=20 Å - which is the end point of slicing. In the slicing process, the atomic density was measured as the total number of atoms divided by the volume of each slice. Similarly, the composition analysis was carried out by measuring the number of Cu and Zr atoms in each slice section and then, dividing the corresponding value by the total number of atoms represented in each slice. RDF and Voronoi analysis were also performed in each sliced section using OVITO [89] and Voro++ code [90], respectively.

3.2.2.5. Measuring Atomic Stress

In order to investigate the mechanical behavior of models under tensile loading, measuring the stress and strain tensors is required. At the atomic scale, stress measurements can be performed using the virial theorem [87,91]. The viral stress used is based on Equation 3-5 [92].

$$\sigma_{ij}^{V} = \frac{1}{V}\sum_{\alpha}[1/2\sum_{\beta=1}^{N}(R_i^{\beta} - R_i^{\alpha})F_j^{\alpha\beta} - m^{\alpha}v_i^{\alpha}v_j^{\alpha}] \qquad \text{Equation 3-5}$$

In this equation, *(i, j)* represents values of X, Y and Z directions; β is the number of neighbors of atom α; R_i^{α} is the position of atom α along the direction of i; $F_j^{\alpha\beta}$ is the force on atom α due to atom β in the direction of *j*; V is the total volume; m^{α} is the mass of atom α; and v_i^{α} is the thermal excitation velocity of atom α along the direction

of i. The viral atomic stresses were averaged over time and normalized by the atomic volume to calculate the stress in the amorphous CuZr layers. The normalization is required since the atomic size of Cu and Zr are different. Due to the different atomic size of Cu and Zr atoms, the atomic volume was calculated as the volume of the model divided by the total number of atoms. The same methodology was applied in computing stresses in the C-A models. It is required to determine yield stress values in the crystalline layer when the first dislocation was nucleated in measurements for *CRSS*. Therefore, a stress tensor was computed in the crystalline layer by defining a group of atoms within the crystalline layer in such a way that the C-A interface does not influence the results. Considering the original C-A interface at X = 0 Å, this group was defined in the crystalline Cu layer within -95 Å < X < -5 Å. The *CRSS* (τ_{CRSS}) was measured using Equation 3-6.

$$\tau_{CRSS} = \sigma_n \cos\varphi \cos\theta \qquad \text{Equation 3-6}$$

Where σ_n is the normal stress along the loading direction (Z) - which was computed in only the crystalline layer as described earlier. The $\cos\varphi \cos\theta$ is called the Schemid factor [93] which can be measured by calculating the angle between loading direction and the normal of the slip plane (φ); and the angle of loading direction and the slip direction (θ). While performing dislocation analysis using OVITO, the slip plane and slip direction were extracted for each C-A model and consequently, the Schemid factor was calculated considering the orientation of the model along the Z direction. Substituting the Schemid factor and normal stress in Equation 3-6, the *CRSS* was measured for the C-A models.

Chapter 4 : Results and Discussion

The current chapter is specified to discuss the results obtained by experiments and MD simulations. Experimental data including the development of the ARB guideline, microstructural analysis, and the nanoindentation results of synthesized samples are provided in the first part. This is followed by MD studies of the microstructural evolution during ARB, and the effects of crystalline orientation on the mechanical properties of C-A composites.

4.1 Experimental

4.1.1 Influences of ARB Parameters on Bonding between Cu-Zr Multilayers

There are several important parameters to consider, including surface roughness, multilayer configuration, Cu/Zr thickness ratio, thickness reduction per rolling pass, annealing temperature and time; all of which should be carefully monitored to assure bonding of metallic Cu-Zr multilayers. The details of the selected ARB parameters will be discussed in following sections.

4.1.1.1. Surface Roughness

As stated in sample preparation protocol in *Chapter 3*, cleaning in acetone and roughening the surface by using a wire brush are important steps in sample synthesis. Figure 4-1 indicates two representative surface profiles obtained from surface roughness measurements before and after brushing. The average surface roughness has been increased from ~ 3.9±0.1 µm to ~ 5.1±0.2 µm due to the brushing.

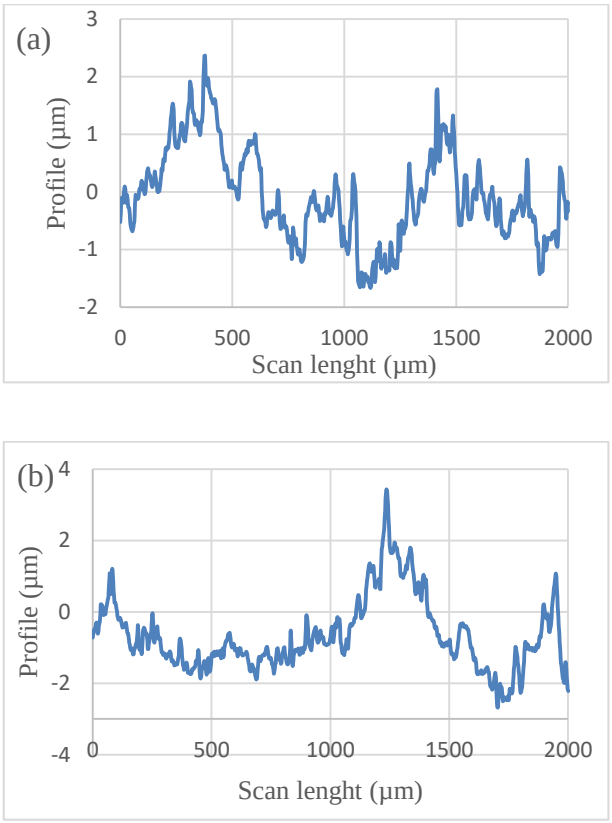

Figure 4-1: Representative surface profiles for the measurement of surface roughness a) before and b) after brushing.

The effects of the remaining particles on the sample surface due to brushing has been carried out by performing an EDS analysis on two samples: one before, and the other after

brushing. As demonstrated in Figure 4-2, the content of carbon (C) and iron (Fe) did not change significantly after brushing; indicating that the effects of the remaining steel particles on the sample surface (due to the brushing) is not a serious issue.

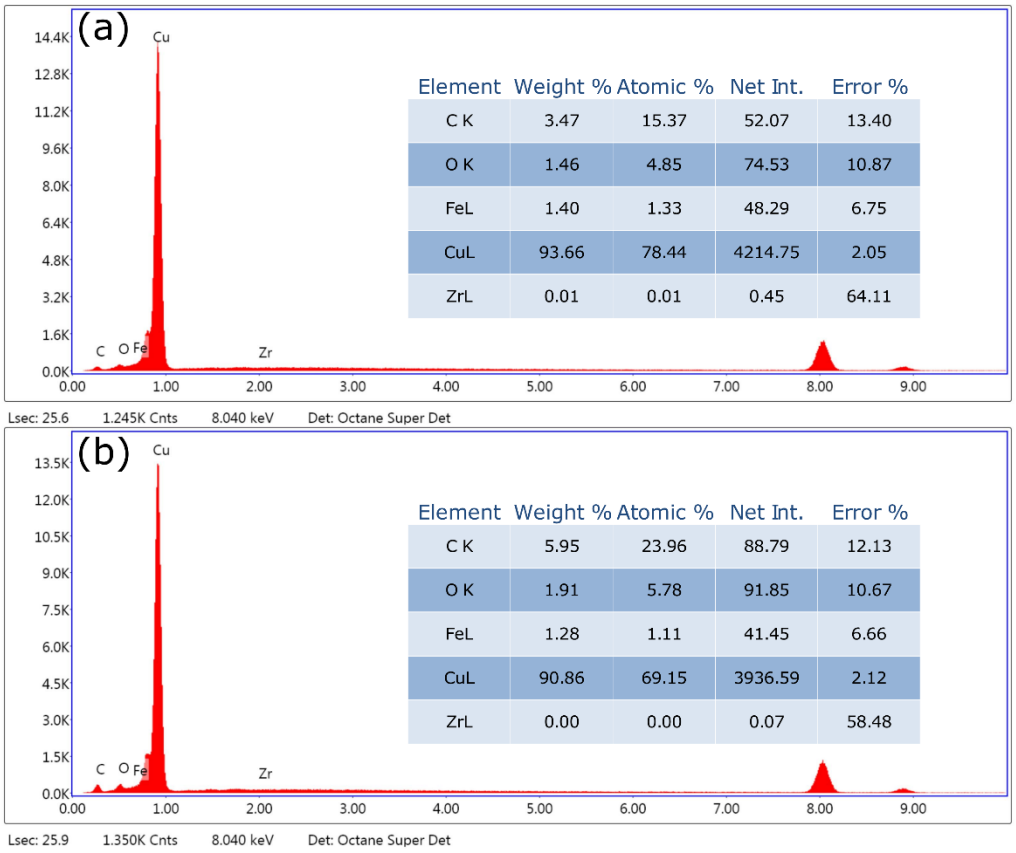

Figure 4-2: EDS analysis on the surface of samples a) before and b) after brushing. The content of Fe and C did not show significant alteration, indicating that there is not a considerable amount of steel particles remaining after brushing.

As discussed in *Chapter 2*, the surface embrittlement can occur due to surface roughening by brushing; and consequently, leads to surface cracking which facilitates the multilayer bonding. The friction shear force between layers is heightened by increasing the surface roughness which imposes severe plastic deformation on the interface of the multilayers. With all other parameters being equal, samples prepared without surface brushing did not

show strong bonding, and the multilayers were delaminated after 1 or 2 passes of rolling. It means that surface roughening is an important factor in the bonding of layers during the ARB process performed on Cu-Zr multilayers.

4.1.1.2. Multilayers Configuration and Cu/Zr Thickness Ratio

As discussed in *Chapter 2*, the configuration of the multilayers and the thickness ratio of Cu and Zr layers (t_{cu}/t_{zr}) are important parameters to consider, as they influence the plastic instability and the multilayer bonding in the ARB process. In order to achieve bonding, different configurations and thickness ratios have been tested. Firstly, two layers of Cu-Zr configuration were attempted. However, bonding of two layers was not successful even though different thickness ratios, including t_{cu}/t_{zr} = 0.5, 1 and 2, were tested. Therefore, the experimentation was shifted to testing three multilayer configurations so that two Cu sheets would be located in the outer layers, and one Zr layer will be located in the middle of the sandwich stack. While testing different thickness ratios, it was found that strong bonding can consistently form when the t_{cu}/t_{zr} was almost equal to 3. The reason can be related to the bonding mechanisms that were discussed at length in *Chapter 2*. If Zr layers are not thin enough in comparison to the Cu layers, the breaking of Zr will not occur; and therefore, the multilayer sandwich sample will remain disconnected after rolling. Table 4-1 summarizes the thickness ratios investigated in the bonding of multilayers. The most efficient thickness ratio was defined as the ratio which met the targeted composition of Cu-Zr, which was assigned as 60-40 as the percentage of Cu and Zr respectively. The target composition has been selected based on the reported data for Cu-Zr systems, which was discussed in *Chapter 2*. Although bonding has been carried out using thick Cu and very

thin Zr layers (for instance 508-50 µm of Cu-Zr thicknesses, respectively), the composition ratio was not high enough to accept such a configuration.

Table 4-1: Different thickness ratios investigated in the bonding of Cu-Zr multilayers during the ARB process.

t_{Cu} (µm)	**t_{Zr} (µm)**	**Bonding status**
508	380	No bonding
508	250	No bonding
508	25	Good bonding but low composition ratio
508	50	Good bonding but low composition ratio
508	110	Good bonding
485	200	No bonding
300	50	Good bonding but low composition ratio
330	150	No strong bonding
330	110	Good bonding

In spite of good bonding found in 3 layers configurations with $t_{cu}/t_{zr} \sim 3$, the total thickness ratio was around 6:1 (total t_{Cu}=660 µm divided by t_{Zr}=110 µm) which is still not close to the target value of ~ 2.5:1. Consequently, the proportion of Zr in the configuration increased by increasing the number of multilayers (i.e. to 5, 7 and 9) with the same t_{cu}/t_{zr} ratio. This attempt led to samples showing good bonding in 5 and 7 layer configurations, while no bonding occurred in 9-layer stacks. The reason for the lack of bonding in 9-layers stacks is that the high total thickness of starting multilayers (more than 2 mm) is above the

capacity of the rolling machine used (10 Ton). As a result, the focus was on 7 layer configurations. Further investigation showed that the thicknesses of the layers can be modified to some extent, especially in the middle layers. The final configuration, which was discussed in *Chapter 3*, contains 4 layers of Cu and 3 layers of Zr, with a total thickness ratio of around 3:1 (t_{Cu}=1100/t_{Zr}=330~3.3).

4.1.1.3. Thickness Reduction per Rolling Pass

As discussed in *Chapter 2*, the percent thickness reduction is a critical factor in the bonding of metallic layers during the ARB process. The current study on Cu-Zr multilayer systems show that a minimum thickness reduction of around 50 % is required for Cu-Zr multilayers bonding. The thickness after rolling pass should be equal to or lower to half of the initial thickness before rolling. Furthermore, the thickness reduction varied from 49 % (rolling from 1430 to 730 µm) to ~ 62 % (rolling from 1190 to 450 µm) depending on the number of rolling cycles for different samples. Any other range in thickness reduction less than 49 % or above 62 % led to either delamination of the multilayer in the former case, or severe cracking in the latter case. Overall, the range of thickness reduction for the ARB process in Cu-Zr multilayers formation was identified to be between 49 to 62 %.

4.1.1.4. Annealing Temperature and Time

The other severe challenge during the ARB process is a loss of ductility due to the cold working. After 2 or 3 rolling passes, the sample was so brittle that it prevented the carrying out of further rolling steps. However, the alloying during the ARB usually occurs following a higher number of rolling passes. In order to continue the rolling process, it is necessary

to recover the ductility of the samples by the intermediate annealing process after each rolling step. Temperature and time are two important parameters in the heat treatment procedure. Due to the presence of two distinct metallic phases (Cu and Zr), finding the appropriate temperature and time was challenging. Considering the recommended temperature and time of annealing for Cu and Zr [94], a systematic study was performed to find the appropriate annealing parameters. As indicated in Table 4-2, the process started at low temperatures of 200 ^{o}C, and increased to a maximum temperature of 1000 ^{o}C. The annealing time was also set between 5 - 90 min.

Table 4-2: Details related to finding the optimized annealing temperature and time for the Cu-Zr multilayers during the ARB process. The focus was on recovering ductility of the samples, as well as minimizing oxidation.

Temperature (^{o}C)	**Time (min)**	**Sample condition**
200	5	Annealed in air, high oxidation, no ductility recovery
200	15	Annealed in air, high oxidation, no ductility recovery
200	60	Annealed in air, high oxidation, no ductility recovery
300	15	Annealed in air, high oxidation, no ductility recovery
300	60	Annealed in air, high oxidation, no ductility recovery
400	5	Annealed in air, high oxidation, no ductility recovery
400	15	Annealed in air, high oxidation, no ductility recovery
400	60	Annealed in air, high oxidation, ductility recovery
500	60	Annealed in air, high oxidation, ductility recovery
300	30	Wrapped in steel sheet, low oxidation, no ductility recovery

300	60	Wrapped in steel sheet, low oxidation, no ductility recovery
400	60	Wrapped in steel sheet, low oxidation, ductility recovery
500	30	Wrapped in steel sheet, minor oxidation, ductility recovery
500	60	Wrapped in steel sheet, minor oxidation, ductility recovery
700	30	Wrapped in steel sheet, minor oxidation, ductility recovery
700	60	Wrapped in steel sheet, minor oxidation, ductility recovery
700	90	Wrapped in steel sheet, minor oxidation, ductility recovery
800	30	Wrapped in steel sheet, high oxidation, ductility recovery
800	60	Wrapped in steel sheet, high oxidation, ductility recovery
1000	60	Wrapped in steel sheet, high oxidation, degraded sample

The obtained data in Table 4-2 shows that at the low temperature range (below than 300 ^{o}C) the ductility was not recovered significantly. Surface cracking occurred during rolling of the samples which were annealed at the low temperature regime, indicating that annealing at low temperatures is not effective. By increasing the annealing temperature up to around 800 ^{o}C, the ductility recovery improved, although oxidation became serious. In order to minimize the oxidation effects, the samples were wrapped in steel sheets during heat treatment. The EDS analysis on the sample surface in Figure 4-3 demonstrates that the oxygen content before and after annealing was similar. That is to say, the steel wrapping was effective in minimizing the oxidation effects.

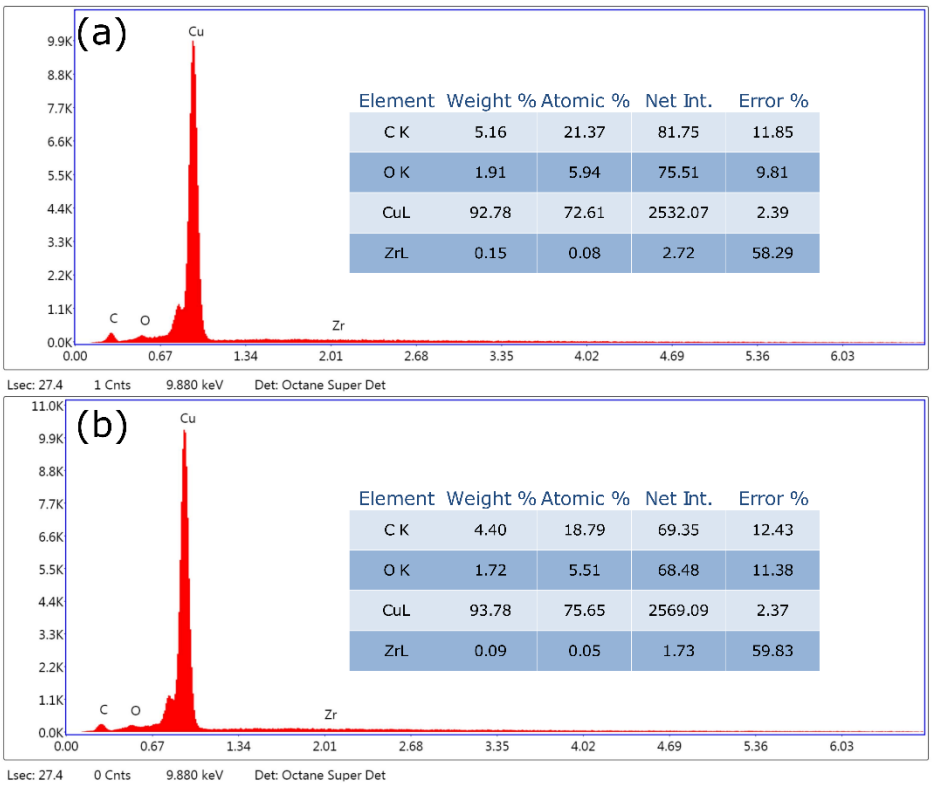

Figure 4-3: EDS analysis on the surface of sample a) before and b) after annealing. Samples did not show significant oxidation during heat sample treatment wrapped by steel sheets.

A high oxidation rate was observed by increasing the temperature to above 800 ^{o}C which was not beneficial during the ARB process. As a result, the efficient annealing temperature was identified to be between 350 ^{o}C to 700 ^{o}C in terms of achieving a minor oxidation rate and good ductility recovery. Considering the crystallization temperature range for different amorphous CuZr compositions between ~ 425 ^{o}C to ~ 525 ^{o}C [95], the effective temperature range identified in this research covers the whole range of crystallization associated with CuZr components. To investigate the effects of the annealing temperature on the amorphization of CuZr during ARB, the lower (350 ^{o}C) and upper (700 ^{o}C) temperature bounds of the efficient range were assigned as the annealing temperature.

The effects of annealing time was also studied and are summarized in Table 4-2. It was found that annealing time should be longer than 30 min to obtain a ductile sample. The ductility recovery improved by increasing the annealing time. However, the impacts of annealing time on ductility recovery was less than the annealing temperature. Based on the obtained data, two different samples were prepared: one annealed at 350 ^{o}C for 60 minutes, and the other one with annealing temperature and time of 700 ^{o}C and 90 minutes respectively, between every single rolling pass.

4.1.1.5. Microstructural Evolution during ARB

The bonding of Cu-Zr multilayers was a challenging step in sample synthesis. As discussed in *Chapter 2* on the bonding mechanisms in a binary system during ARB, the harder phase experienced necking, and consequently, broke down into small pieces. The soft phase can penetrate in the middle of the broken particles, allowing them to reach the adjacent soft layer. Figure 4-4 indicates the structural evolution on the cross section of the Cu-Zr multilayers following different rolling steps from 2 to 8. As it is clear, the Zr layers breaks down into smaller pieces after 6 rolling steps. The different hardness values of Cu (100.8 HV) and Zr (196 HV), measured in this study, imposed different elongation rates during the rolling process. While Cu is part of the soft phase and can be elongated easily, the hard Zr phase is not able to elongate with the same rate as the Cu layer. Consequently, the hard Zr phase breaks down into small pieces through the necking process due to plastic instability (see Figure 4-4 (a)). The plastically deformed Cu regions can flow in between these broken Zr particles and reach the adjacent Cu layer through the process of cold welding (or cold bonding). As shown in Figure 4-4, the multilayer structure contains the

distributed broken Zr particle in the Cu matrix following increased number of rolling cycles from 2 to 8.

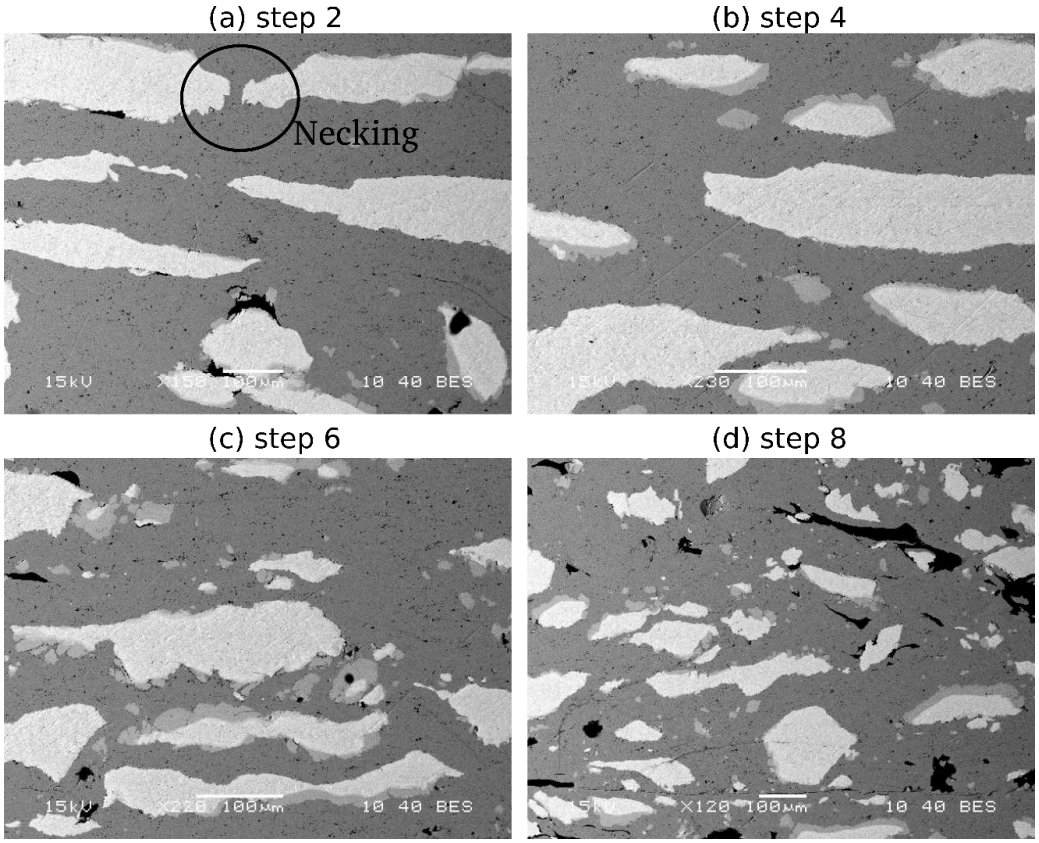

Figure 4-4: SEM image on the cross section of samples after a) 2nd, b) 4th, c) 6th and d) 8th cycles of rolling. The structural evolution during ARB process can be captured through breaking down of Zr layers into small particles.

The observed microstructural evolution in the SEM analysis of Figure 4-4 is in well agreement with the SEM data reported by Sun *et al.* [9] and Ohsaki *et al.* [10] on ARB structural studies of highly pure Cu-Zr multilayer systems. Both studies have shown the island-like Zr blocks distributed in the Cu matrix after ~ 6 ARB cycles. However, the final structure after ~ 9 ARB cycles have shown an almost lamellar configuration which is not observed in this current work. There was also a transformation from inhomogeneous to homogeneous deformation after around 6 ARB passes due to homogenization of hardness

mismatch between Cu and Zr layers, as claimed in [10]. It should be noted that the ARB procedure has been modified in current study to implement intermediate annealing which is necessary to conduct large strain deformation on commercial Cu-Zr multilayers. However, the intermediate annealing has not been performed in [9,10] and therefore, the Cu layers were more work-hardened than Zr layers after around ~ 6 ARB cycles and consequently, homogeneous deformation occurred due to the close hardness values of Cu and Zr phases. This is in contrast to the current research where large hardness mismatch causes inhomogeneous deformation even after 10 ARB passes. Meanwhile, the alloying and formation of a new phase even in early steps of ARB process, as indicated in Figure 4-4, was not reported in previous studies. It seems that the intermediate annealing facilitates the mechanical alloying during the ARB process of commercial Cu-Zr multilayers which will be discussed later in this chapter. In addition, it has been shown that the purity of the Zr element, especially in terms of oxygen and nitrogen content, has a strong influence on its mechanical properties [96]. Consequently, the difference between the current microstructure and the above-mentioned studies after ~ 9 ARB cycles can be related to the purity of starting materials, particularly for the Zr sheets. While the purity of the applied Zr sheets in [9,10] were more than 99.8 % with the hardness of around 160 HV [10], the as-received Zr sheets in this study contained higher amounts of impurities as stated in *Chapter 3* with the hardness value of around 196 HV. The large hardness mismatch is the reason that the elongation rate of the Cu and Zr sheets used in current study are dramatically different. The strong mismatch in the elongation rate during the ARB process is a source of stress raiser at the interface. As a result, defects such as cracks and voids (observed in Figure 4-4) were initiated and propagated due to stress concentration and a

heavy state of loading. The presence of defects and a strong mismatch between elongation rates avoid homogeneous deformation state that was reported in [9,10]. It is worthwhile mentioning that commercial Zr sheets have significantly lower price than highly pure ones. Such variation in costs of starting materials can cause a huge difference on final product's price, especially in large-scale production.

4.1.1.6. Summary of Efficient ARB Parameters

The prepared multilayer samples were 6 cm wide to minimize defects such as edge cracking. The final thickness of the obtained samples varied from around 0.5 mm to 0.9 mm depending on the thickness reduction following each cycle and the number of rolling passes. In summary, Table 4-3 indicates the most efficient ARB parameters for synthesis of two types of Cu-Zr samples. Sample I was rolled up to 10 cycles, while the ARB process terminated in cycle 8 for sample II, as the ductility recovery was not as good as sample I due to the annealing temperature of 350 ºC. The following analysis (both microstructure and mechanical testing) are all based on parameters summarized in Table 4-3 and conducted on average 10 number of samples for each type I and II. Samples will be referred to as sample I and II for further analysis.

Table 4-3: Efficient parameters in ARB process of Cu-Zr samples.

ARB parameters	Number of starting multilayers	t_{cu}/t_{zr}	Thickness reduction (%)	Annealing temperature (°C)	Annealing time (min)	Number of ARB cycles
Sample I	7	~ 3	49 to 62	700	90	10
Sample II	7	~ 3	49 to 62	350	60	8

4.1.2 Microstructural Analysis

Figure 4-5 shows sample I after 10 rolling passes and the corresponding SEM image displaying the cross-sectional area. Three distinct phases can be easily detected in Figure 4-5. Since the process started with two metallic crystalline phases, the presence of Cu (dark) and Zr (bright) phases are expected. However, the interesting point in the SEM image is the formation of a phase (gray) with unknown composition and structure; which is the sign of alloying CuZr phases during the ARB process. In this section, the microstructural analysis based on EBSD, SEM, TEM and EDS will be discussed.

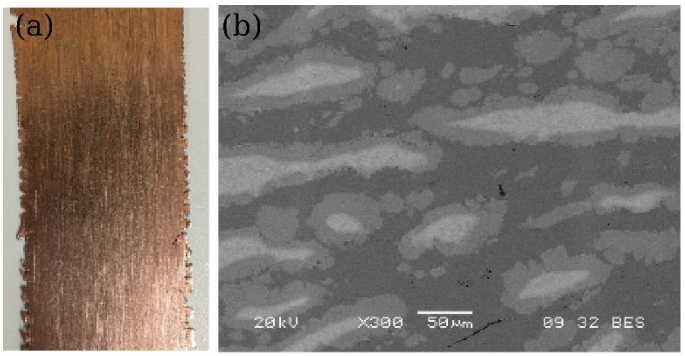

Figure 4-5: (a) Synthesized sample and (b) SEM on the cross section for sample I after 10 rolling passes.

4.1.2.1. Grain Structure Evolution on Cross Section

EBSD analysis was performed on the cross section of the samples after its 2^{nd}, 4^{th}, 6^{th} and 8^{th} steps of rolling, prepared from sample II. The EBSD analysis was carried out before the annealing process following each pass. The EBSD mapping and corresponding phase map for each rolling pass is demonstrated in Figure 4-6.

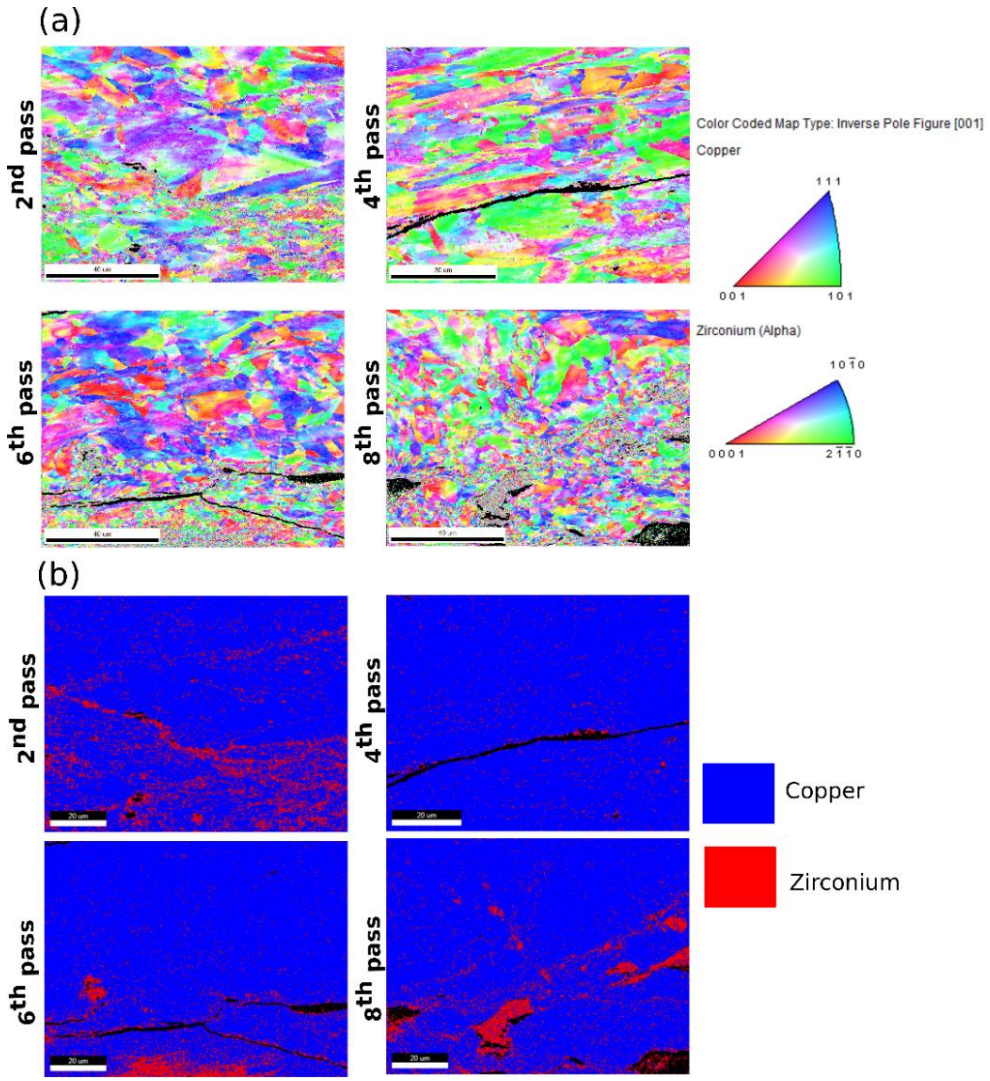

Figure 4-6: a) EBSD mapping on the samples prepared from cross section following different steps of rolling, and b) EDS mapping on the same area of EBSD mapping showing the composition ratio.

Interpretation of the EBSD results reveals several important microstructural characteristics. Firstly, there are several regions which do not show any grain structure. Considering the EDS mapping in Figure 4-6 (b), the region composition without a grain structure shows the CuZr phases. The reason for such behavior are two-fold: insufficient surface quality (which might be the case even after ion polishing), or the absence of a crystalline structure. Although the presence of rougher surfaces are possible, the grain structure of the

surrounding areas can provide a clue in determining if a sufficient surface quality exists. Another possible reason for the absence of a grain structure in EBSD mapping of CuZr phases can be due to their amorphous or semi-amorphous structures. In spite of providing a strong clue through EBSD analysis, the amorphous nature of CuZr phases cannot be confirmed by EBSD analysis.

The refinement of the microstructure, which can be captured by gradual decreasing grain size with increasing number of rolling passes, is also evident from the EBSD analysis. Figure 4-7 indicates the quantitative analysis on the cross-section grain size evolution during the ARB process. As demonstrated, the average grain size decreases from ~ 10 μm in the 2^{nd} pass of rolling to less than 1 μm in the 8^{th} pass of rolling. As discussed in *Chapter 2*, the mechanical alloying mechanisms during ARB are associated with an increase in free energy due to defects, such as dislocations as well as structural refinement. The observed grain structure refinement in Figure 4-7 can also cause a higher diffusion rate at the grain boundary and interfacial regions. Consequently, mechanical alloying mechanisms and a higher diffusion rate due to the structural refinement can facilitate the formation of CuZr phases at the interfacial regions during the ARB process.

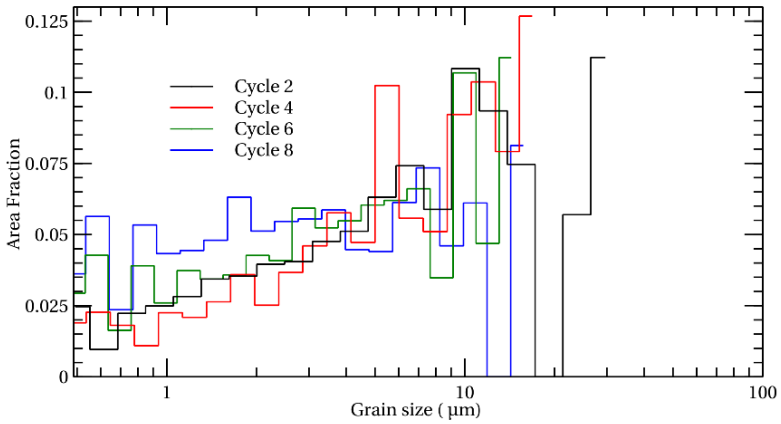

Figure 4-7: Grain size variation on samples prepared from cross section in different steps of rolling.

4.1.2.2. Development of CuZr Phases

The alloying and consequent formation of CuZr phases during the ARB process is demonstrated in Figure 4-5 (b). EDS analysis was performed on the cross section of sample I to identify the compositional content of the formed phases during the ARB process. Figure 4-8 demonstrates the composition results from the EDS analysis. As it can be seen, three distinct phases such as pure Cu (Figure 4-8 (a)), pure Zr (Figure 4-8 (e)) and several CuZr phases (Figure 4-8 (b), (c) and (d)) are presented in the EDS results of the roll-bonded sample. While the quantitative analysis on the selected areas shows upwards of a 99 % pure Cu and Zr composition, the corresponding data for CuZr phases reveals a variety of compositions including $Cu_{38}Zr_{62}$ (Figure 4-8 (b)), $Cu_{50}Zr_{50}$ (Figure 4-8 (c)) and $Cu_{62}Zr_{38}$ (Figure 4-8 (d)). As a result, the EDS results confirmed that CuZr phases with different formulae (~ $CuZr_2$, CuZr and Cu_2Zr) are formed during the ARB process. The formation of CuZr phases were observed in all synthesized samples (~ 10 samples).

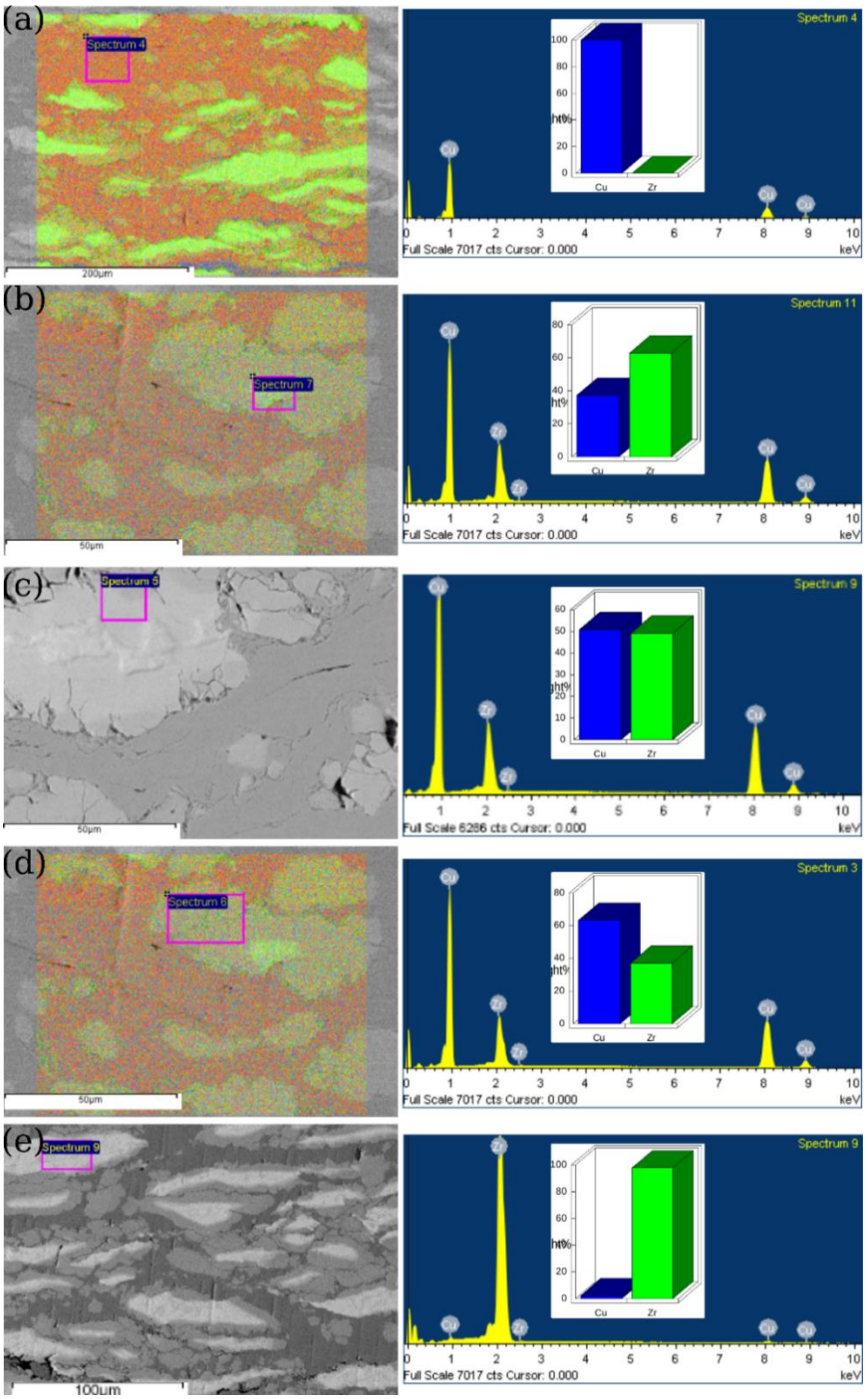

Figure 4-8: EDS analysis and composition of (a) pure Cu, (b) $Cu_{38}Zr_{62}$, (c) $Cu_{50}Zr_{50}$, (d) $Cu_{62}Zr_{38}$ and (e) pure Zr phases. The results obtained based on EDS analysis on around 10 samples.

Based on the alloying mechanisms during the ARB process which were discussed in *Chapter 2*, the inter-diffusion of Cu and Zr can take place at the interfacial regions which

are responsible for the formation of inter-metallic CuZr phases. The microstructural refinement was discussed earlier in Figure 4-7 as a facilitating factor in the inter-diffusion phenomenon. The evidence of such inter-diffusion phenomenon can be found in area mapping and line scan results shown in Figure 4-9 for a representative sample I (the same phenomena were observed for all samples). As it is clear from line scan analysis in Figure 4-9 (b), the gradual variation of Cu and Zr compositions at the interface regions supports the occurrence of inter-diffusion. EDS mapping in Figure 4-9 (a) indicates that CuZr phases are mostly formed around the interface of Cu and Zr phases, which provides further evidence of inter-diffusion at the interfacial regions.

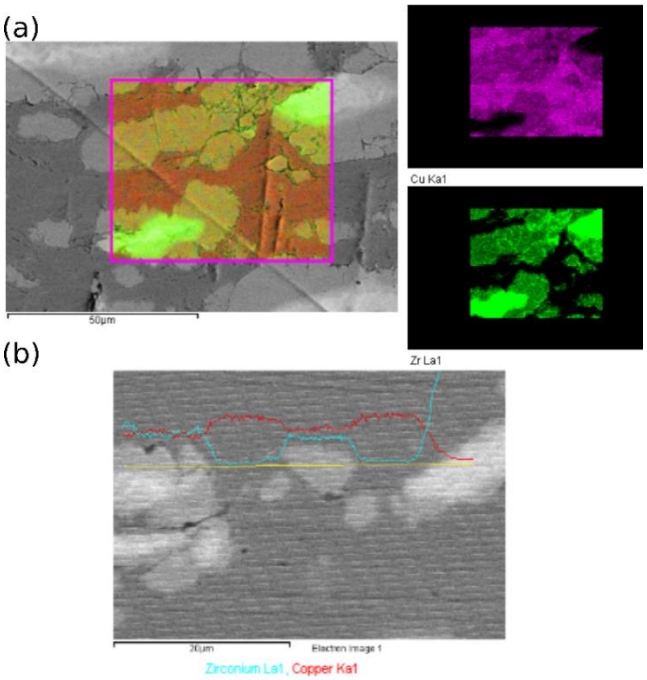

Figure 4-9: a) EDS mapping on cross section, and b) line scan analysis showing the formation of CuZr phases and inter-diffusion around interface.

The presence of CuZr phases with different compositions in the rolled samples has been confirmed in EDS analysis, indicating that the alloying occurs during the ARB process.

This is different from the results of [9,10] where the strong alloying was not reported in SEM analysis. As discussed earlier, the intermediate annealing procedure performed in current study, is a significant step in mechanical alloying during the ARB procedure of commercial Cu-Zr multilayers. Annealing has been led to the formation of several CuZr phases with different compositions. Particularly, the inter-diffusion rate, discussed in Figure 4-9 as the atomistic mechanisms of alloying, is higher with increasing temperature [97]. Therefore, intermediate annealing procedure increases the rate of inter-mixing Cu and Zr atoms during the ARB process, facilitating the formation of CuZr phases. Furthermore, the fraction of new-formed CuZr phases are so high that are easily detected in SEM and EDS analysis, in contrast to limited narrow regions (with thickness of less than 1 nm) in previous TEM studies [9,10]. Table 4-4 summarizes the main differences between current work and previous studies in terms of materials used, procedure and results.

Table 4-4: A summary of differences in terms of materials, procedure and results between current and previous studies on ARB of Cu-Zr multilayers.

Research groups	Materials	Procedure	Results
Current study	Commercial Zr and Cu sheets	ARB with intermediate annealing	Significant alloying and formation of CuZr phases even in early steps of the ARB
Sun *et al.* [9]	Highly pure Zr and Cu sheets	ARB with no intermediate annealing	No significant alloying was observed in SEM
Ohsaki *et al.* [10]	Highly pure Zr and Cu sheets	ARB with no intermediate annealing	No significant alloying was observed in SEM and limited narrow CuZr regions were detected in TEM analysis

The structure of the newly formed phases remains unknown. As discussed in Figure 2-4, the experimentally extracted phase diagram of binary Cu-Zr alloys shows that the inter-metallic Cu-Zr compounds can form in thermodynamic equilibrium. The crystalline $Cu_{10}Zr_7$, which has close composition with the detected $Cu_{62}Zr_{38}$ phase in the EDS analysis, is stable up to around 900 ^oC. Furthermore, the crystalline $CuZr_2$ phase is also stable up to around 1000 ^oC and it has close formula with the identified $Cu_{38}Zr_{62}$ phase; while the crystalline CuZr phase ($Cu_{50}Zr_{50}$) is not stable below 715 ^oC. Overall, it is important to investigate the structure of the CuZr phases to determine whether it is crystalline (as those inter-metallic components in phase diagram) or amorphous (such as those represented in *Chapter 2*).

4.1.2.3. TEM Structural Analysis

As was mentioned in Section 4.1.1.4, two different samples were prepared by applying two annealing temperatures of 350 ^oC and 700 ^oC, representing a lower and a higher temperature bound than the crystallization temperatures [95], respectively. TEM with electron diffraction analysis was performed in order to investigate the structure of the CuZr phases and the effects of annealing temperature on the structure of the formed phases. The TEM results of the sample prepared with an annealing temperature of 700 ^oC (sample I), shown in Figure 4-10, demonstrate the presence of both crystalline and amorphous phases. While the electron diffraction reveals the crystalline structure for the right-side selected area (which is obvious even from the image itself), the corresponding diffraction on the left-side area indicates an amorphous structure. More interestingly, the d-spacing measured by the electron diffraction (shown in Figure 4-10) matches with a pure Zr phase; while the

corresponding EDS data indicates a $Cu_{26}Zr_{74}$ composition for the amorphous region. To this point, the presence of an amorphous phase is confirmed by electron diffraction methods.

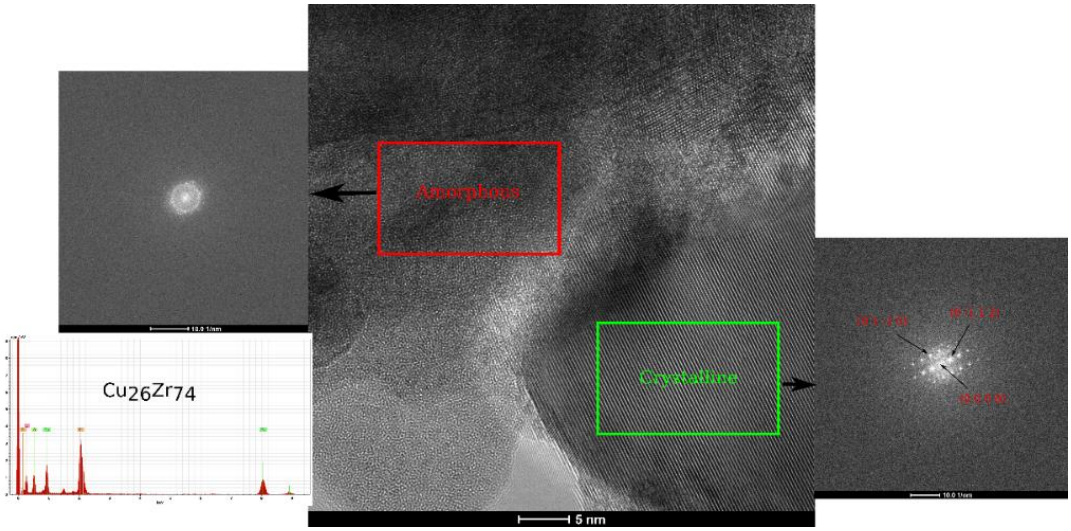

Figure 4-10: TEM results with electron diffraction analysis. The distinct two regions with amorphous CuZr (left side box) and crystalline Zr (right side box) structures were identified (annealing temperature was 700 ^{o}C).

Higher magnification of the TEM analysis of the same sample (sample I) is shown in Figure 4-11 indicates important aspects of structural analysis. Similar to low magnification analysis, the presence of both crystalline and amorphous phases is obvious. However, the main point in Figure 4-11 is that both phases have shown similar CuZr compositions. The EDS analysis demonstrates the composition of $Cu_{26.9}Zr_{63.9}$ for both amorphous and crystalline regions, which are in good agreement with the EDS results from SEM analysis. The impurity content - including elemental C and O - were not considered in EDS composition analysis as they are common in TEM samples prepared using the electro polishing technique. CuZr phases has a close formula to $CuZr_2$, which was representing in the phase diagram as a stable crystalline phase up to around 1000 ^{o}C. The measured d-spacing is well matched to that of tetragonal $CuZr_2$ crystalline phase with lattice parameters

of a=b= 3.22 Å and c=11.18 Å [98]. However, the electron diffraction shows that the amorphous structure for this composition is also formed, although it is limited to small regions. The interface between amorphous and crystalline phases is highlighted in Figure 4-11. Annealing the samples at 700 ºC increases the chance of crystallization of formed CuZr phases, and consequently, widespread amorphous regions were not detected in the TEM analysis for sample I.

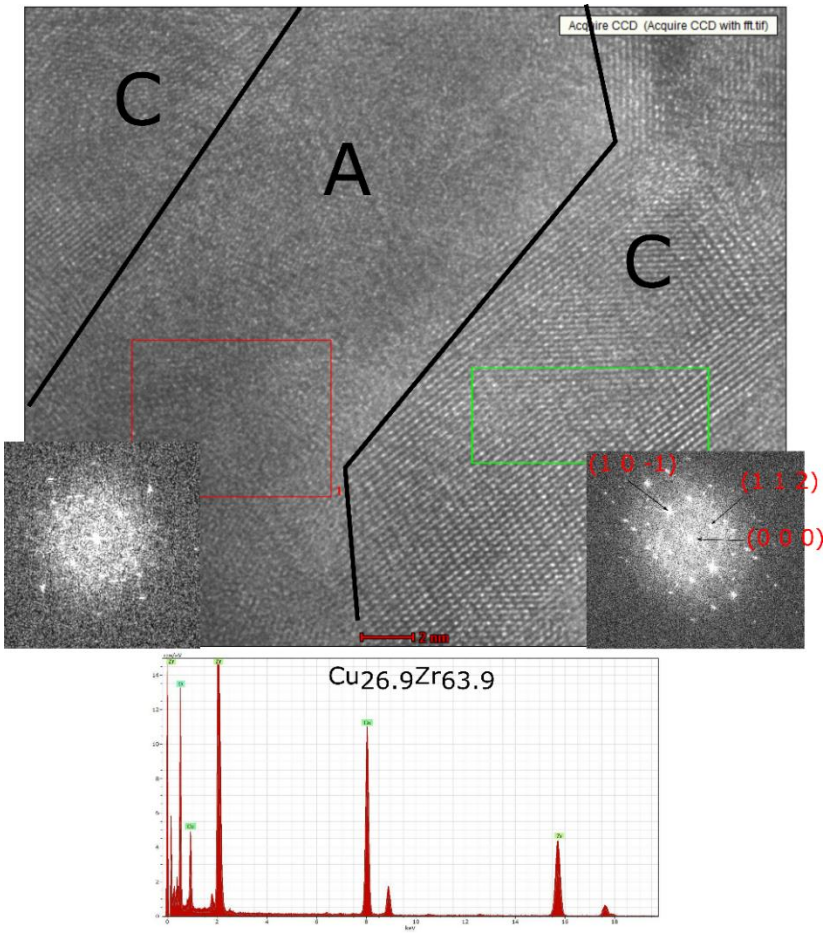

Figure 4-11: High magnification of TEM analysis revealing the presence of both amorphous and crystalline CuZr2 phases (annealing temperature was 700 ºC).

In order to eliminate the crystallization phenomenon, the annealing temperature was set at 350 ºC (sample II) which is lower than the crystallization temperature of ~ 425 ºC [95].

The crystalline $Cu_{31}Zr_{69}$ phase is detected as shown in the TEM analysis of Figure 4-12. Similar to the other sample with a higher annealing temperature (sample I), the formula of the detected phase is very close to a crystalline $CuZr_2$ inter-metallic compound. Although the annealing temperature is below the crystallization temperature for all possible CuZr intermetallic compounds reported in [95], the formation of crystalline CuZr phases still occurred during the ARB process in this work.

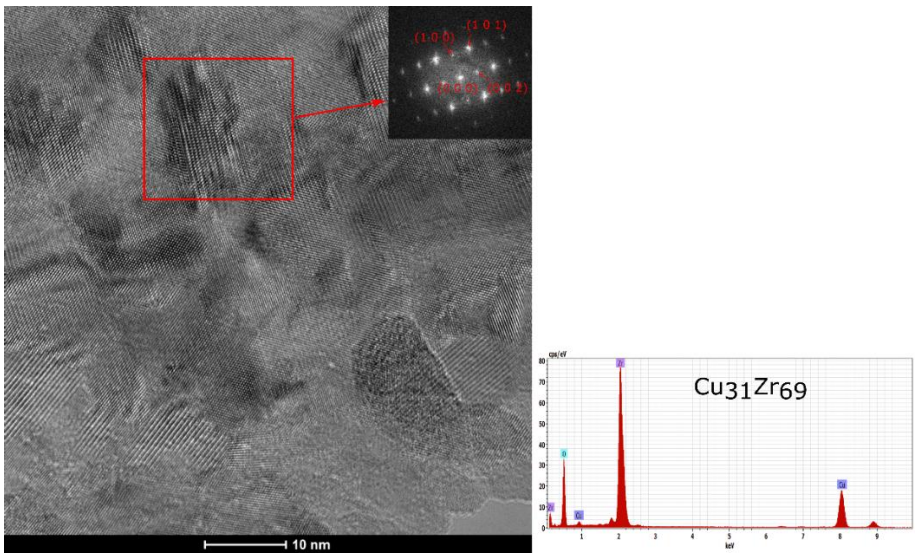

Figure 4-12: High magnification TEM analysis revealing the presence of crystalline $Cu_{31}Zr_{69}$ phase (annealing temperature was 350 ºC).

The influence of annealing temperature on the structure of the CuZr phases can be recognized by the fact that the widespread amorphous regions have been detected in samples which annealed at 350 ºC. As shown for a representative region in Figure 4-13 (a), the electron diffraction pattern of the $Cu_{36}Zr_{64}$ phase contains hollow circles, as well as spots indicating the presence of both crystalline and amorphous phases. This is confirmed in high magnification TEM analysis on display in Figure 4-13 (b), where the amorphous regions are located beside the crystalline nanoparticles. Overall, formation of amorphous

$CuZr_2$ phase adjacent to the crystalline $CuZr_2$ nanoparticles, observed in TEM analysis of sample II, indicates an ultrafine structure which is different from the reported multilayer structure in [10]. In fact, both alloying and amorphization of CuZr phases during the ARB process have been facilitated due to the intermediate annealing procedure, led to the ultrafine microstructure in current study.

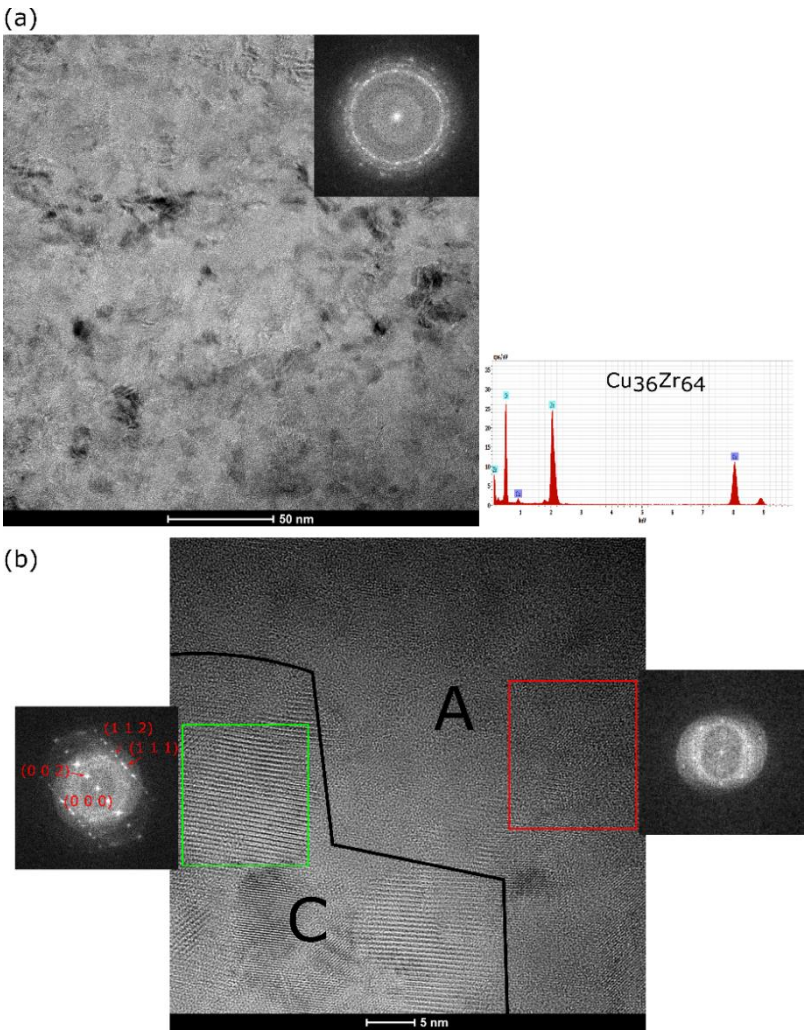

Figure 4-13: TEM analysis (a) electron diffraction pattern containing both hollow circles and spots, and (b) high magnification TEM revealing the presence of both amorphous and crystalline $Cu_{36}Zr_{64}$ phases (annealing temperature was 350 ºC).

Theoretical investigation of thermodynamics and kinetics of CuZr amorphization has revealed high glass forming ability close to intermetallic compounds [99]. The key conclusion was that the Gibbs free energy has demonstrated a sharp increase for intermetallic compounds, leading to a lower Gibbs free energy neighboring the intermetallic compositions. The temperature dependent viscosity was also indicated the kinetically favored glass forming compositions close to the intermetallic compounds, especially for $Cu_{10}Zr_7$, CuZr and $CuZr_2$.

The amorphization of CuZr phases with compositions close to the $CuZr_2$ phase in this work (observed in both samples with different annealing temperatures) is in well agreement with the theoretical predictions of glass forming ability reported in [99]. However, based on the TEM and electron diffraction analysis, amorphization of CuZr phases during ARB process is more likely to occur by annealing at a temperature lower than the crystallization temperature. Overall, TEM and electron diffraction analysis indicated that the C-A composite structures were synthesized by ARB. The crystalline phases include pure Cu, pure Zr, and a possible crystalline CuZr phase such as $CuZr_2$. The formation of amorphous CuZr phases during the ARB process resulted in amorphous regions distributed in the crystalline matrix.

4.1.3 Mechanical Properties: Nanoindentation

The elastic modulus and hardness of both samples (I and II) have been extracted using a large set of testing data based on nanoindentation. Figure 4-14 shows the typical load-displacement curves for pure Cu, pure Zr, and representative CuZr phases for two annealing

temperatures of 350 ºC and 700 ºC. The indentation depths for the three representative phases, in a sample with annealing temperature of 350 ºC shown in Figure 4-14 (a), takes different values for pure Cu (~ 400 nm), pure Zr (~ 290 nm) and CuZr phases (~ 150 nm). The corresponding indentation depths for the sample with an annealing temperature of 700 ºC (Figure 4-14 (b)) are ~ 400 nm, 300 nm and ~ 200 nm for pure Cu, pure Zr and CuZr phases, respectively. As a key difference, the presence of pop-in feature is highlighted in load-depth curves for the CuZr phase, formed in a sample II. As stated in *Chapter 2*, the presence of pop-in features in nanoindentation load-depth curves is a strong support of the amorphous nature of indented metallic phases. The absence of a pop-in feature in the load-depth curve for CuZr phases with an annealing temperature of 700 ºC is in well agreement with the TEM analysis where the widespread amorphous phases were not detected. In contrast, the amorphization of CuZr phases below the crystallization temperature is supported by the pop-in feature of nanoindentation load-depth curves in Figure 4-14 (a).

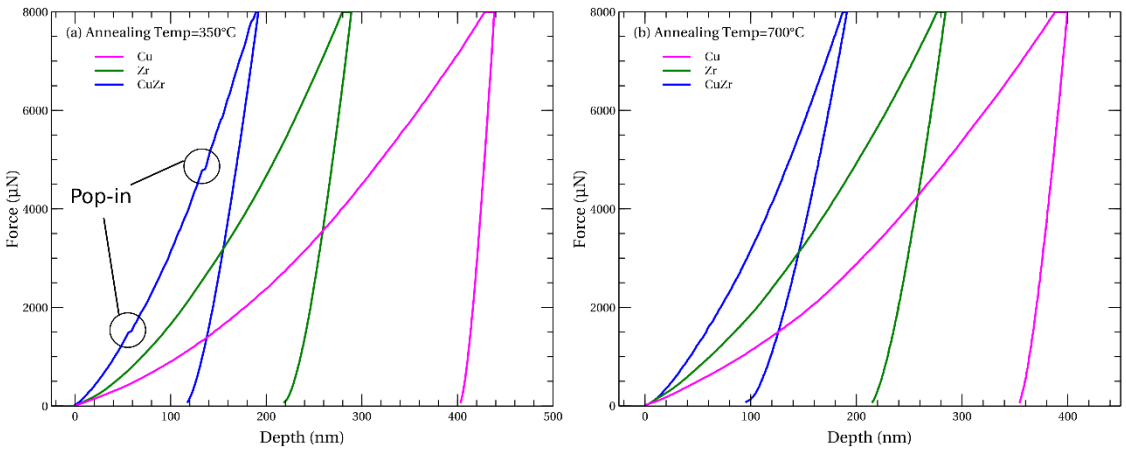

Figure 4-14: Representative load-depth curve in nanoindentation testing of pure Cu, pure Zr and CuZr phases (a) for the sample annealed at 350 ºC and (b) for the sample annealed at 700 ºC.

In order to extract elastic modules and hardness values, large-scale tests were performed as demonstrated in SEM image of a representative sample II in Figure 4-15. EDS analysis on the sample with an annealing temperature of 350 ºC in Figure 4-15 indicates that the indentation spots cover different phases, including dominant Cu (area 1), dominant Zr (area 3) and $Cu_{76.46}Zr_{23.54}$ phases (area 2).

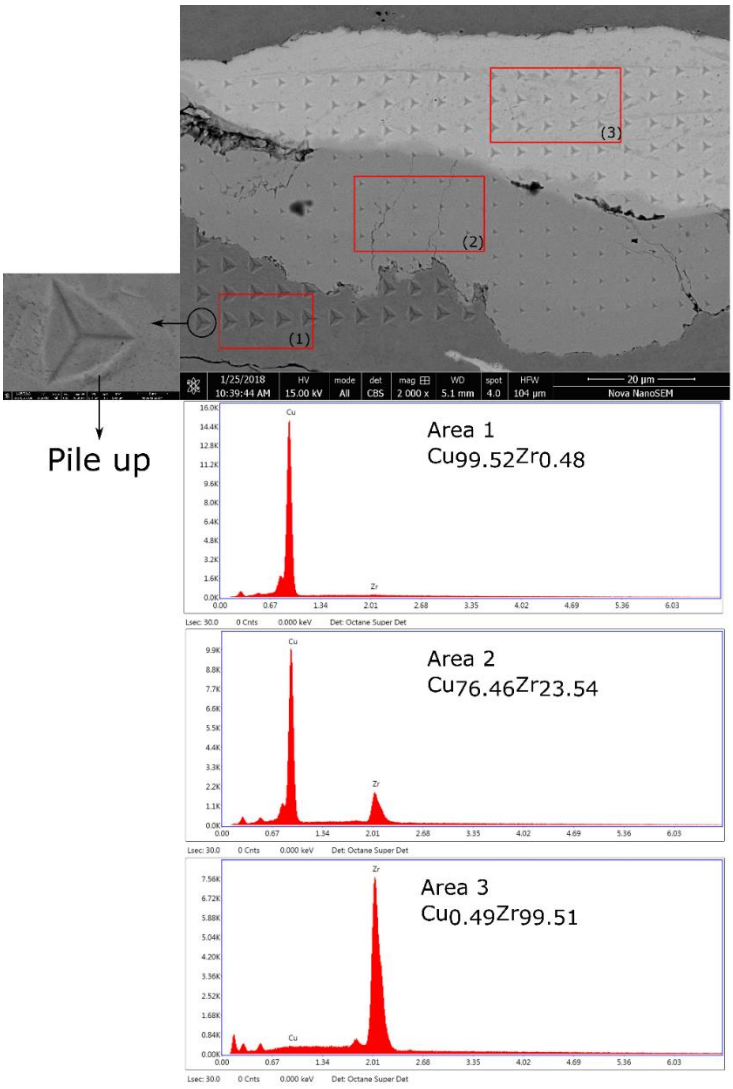

Figure 4-15: SEM image showing the indentation spots and EDS analysis of different representative phases including Cu, Zr and CuZr. The nanoindentation was performed on a sample II with an annealing temperature of 350 ºC.

Figure 4-16 indicates the indentation spots and the corresponding hardness values for each spot in the sample with an annealing temperature of 350 ºC (sample II). Herein, the★ sign represents pop-in in load-displacement curves. Also, both color and size of the symbols are proportional to the hardness values. The results in Figure 4-16 (b) reveal that the hardness of CuZr phase (~ 8 GPa) are higher than pure Cu (~ 2 GPa) and Zr (~ 4 GPa) phases. Although the pop-in feature was observed in load-displacement curves for most CuZr spots, there are a few number of CuZr spots which do not show the strong pop-in feature. This is consistent with the TEM analysis in Figure 4-13 that indicates an ultrafine structure (containing both amorphous and crystalline $CuZr_2$ phases) for sample II. Due to the fact that the nanoindentation is a local testing procedure, it is possible that the CuZr spots without the pop-in feature are located on the crystalline phases.

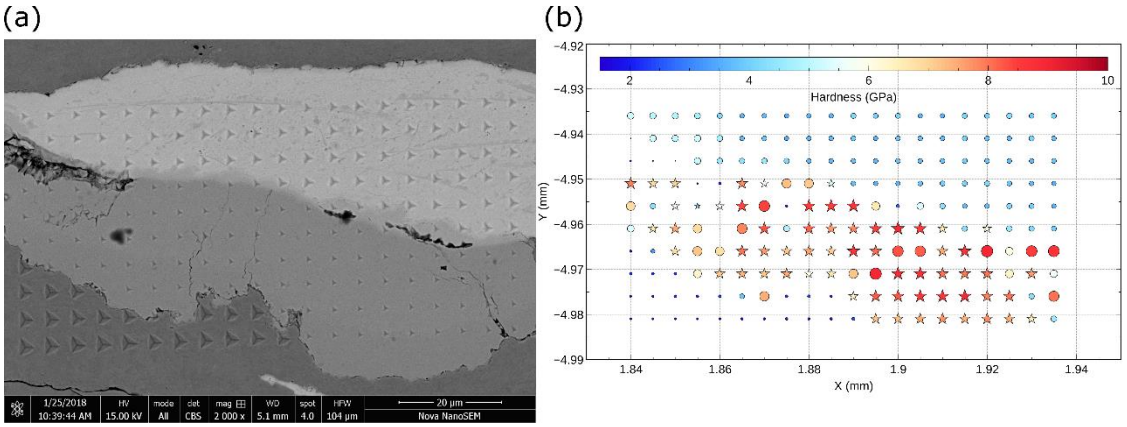

Figure 4-16: Large-scale nanoindentation testing. (a) SEM image indicating the indentation spots and (b) is the hardness values for each spot in samples with an annealing temperature of 350 ºC. In this figure, ★ is representing pop-in in load-displacement curves. Also, both color and size of symbols are proportional to the hardness values.

After eliminating the spots which are located on cracks or interfaces, the average elastic modulus and hardness values were extracted and summarized in Table 4-5. The data was extracted for each phase by averaging over at least 10 indents. Based on the results of both

samples in Table 4-5, Cu is the soft phase with an average hardness of ~ 2 GPa, Zr can be identified as the intermediate phase with an average hardness of ~ 4.2 GPa, and the CuZr phases formed during the ARB process have recorded the highest hardness at ~ 8 GPa. The obtained results are in well agreement with the reported hardness values on nanoindentation testing of CuZr phases using the Berkovich tip [100]. The trend in results for elastic modulus also demonstrated higher values for CuZr (~ 125 GPa) than both Cu (~ 110 GPa) and Zr (~100 GPa) phases in both samples. However, the corresponding elastic modulus for each phase in sample with an annealing temperature of 350 ºC recorded almost 10 % higher values in comparison with samples annealed at 700 ºC. Such a behavior can be related to the state of residual stresses which might be different as a function of annealing temperature. It was shown that since the pile up around the indenting spots (indicated in Figure 4-15) is not considered in the calculation of contact area in nanoindentation testing; therefore the reduction in elastic modulus by changing the state of residual stress is not real [101]. Meanwhile, in the CuZr phases, the possible structural differences observed in both TEM and nanoindentation curves (pop-in feature) may have resulted in the reduction in elastic modulus due to increased annealing temperature.

Table 4-5: Nanoindentation hardness and elastic modulus for different phases in samples with two different annealing temperatures.

Phase	**Annealing Temperature of 350 ºC**		**Annealing Temperature of 700 ºC**	
	H_{avg} (GPa)	E_{avg} (GPa)	H_{avg} (GPa)	E_{avg} (GPa)
Pure Cu	2.0 ± 0.2	124 ± 5	2.2 ± 0.2	104 ± 2
Pure Zr	4.1 ± 0.3	106 ± 5	4.4 ± 0.3	93 ± 3
$Cu_{76.46}Zr_{23.54}$	8.3 ± 0.4	132 ± 4	-	-
$Cu_{74.4}Zr_{21.6}$	-	-	7.6 ± 0.5	117 ± 4

4.2 Molecular Dynamics Simulations

This section provides the results of numerical MD simulations as a complementary analysis for experimental data. As it was discussed in *Chapter 2*, the limitations of both experimental and numerical techniques in atomic scales make the exact comparison of these data difficult. However, in order to capture the deformation mechanisms during the ARB process, accumulative rolling of crystalline Cu-Zr multilayers was simulated using MD. The MD findings on ARB process have been compared with experimental characterizations and the similarities and differences have been discussed in first part. Studying the influence of the C-A interface on the mechanical properties and yielding mechanisms of C-A composites will also be elaborated on in second section.

4.2.1 MD Simulation of ARB Process

Figure 4-17 indicates the accumulative rolling simulation from cycle 2 to 6. As demonstrated, the Zr layer (in red) has experienced necking (which is shown by circles on Figure 4-17 (b)) following increased number of rolling cycles. Consequently, several island-like regions have been created due to the breaking down of the Zr layer. Finally, Zr atoms were diffused all over the sample following higher number of rolling cycles (for instance cycle 6 in Figure 4-17 (e)). Similar behavior was observed during the ARB process of Cu-Zr multilayers which was discussed in Figure 4-4, indicating that the MD results can be used to capture the deformation mechanisms of crystalline multilayers during the ARB procedure. However, the state of deformation in the MD models of Figure 4-17 are more homogeneous than the observed experimental structure in Figure 4-4, as the MD models

show a lamellar structure after 6 cycles of rolling. While the as-received Cu and Zr sheets are polycrystalline materials with impurities and possible defects (e.g. dislocations or pre-cracks), the MD models contain 100 % pure single crystalline Cu and Zr layers that are free of defects. In addition, MD simulations are inherently limited by the small model size and time scale. However, although MD cannot be used to fully repeat experimental observations, it is useful in studying the atomistic mechanisms during the ARB process such as inter-diffusion.

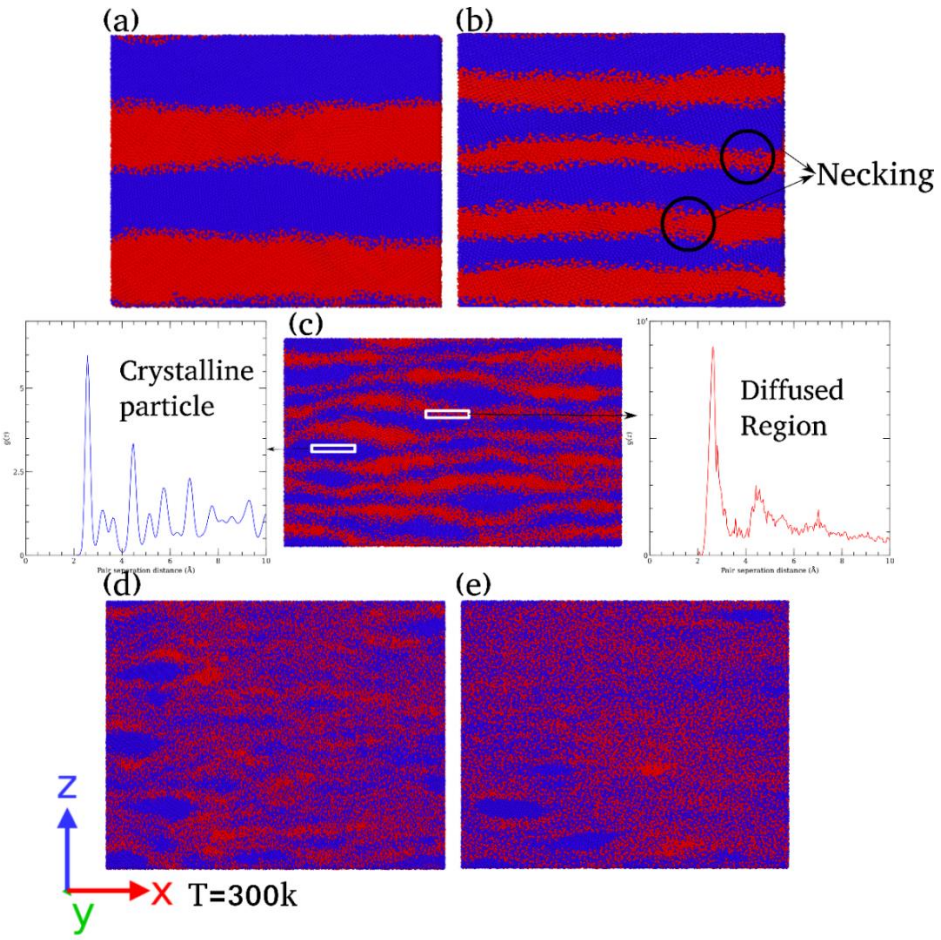

Figure 4-17: Different steps of MD simulation of accumulative rolling (a) step 2, (b) step 3, (c) step 4, (d) step 5 and (e) step 6. The inset in (c) indicates the RDF analysis on crystalline Cu and diffused CuZr regions.

Further investigation of MD results in Figure 4-17 reveals that the inter-diffusion of Cu and Zr atoms at the multilayer interface is the atomistic mechanism of mechanical alloying. As indicated in the zoomed-in image in Figure 4-17 (c), a mixed region containing both Cu and Zr atoms is created at the interface of the Cu-Zr layers. RDF analysis on this mixed region (Figure 4-17 (c)) shows a broadened peak which is a sign of a disturbed crystalline lattice. The inter-diffusion mechanisms observed in the MD simulation at the interface of the Cu-Zr layers is in well agreement with the EDS analysis displayed in Figure 4-9, which indicated the presence of CuZr phases at the interface regions. RDF analysis on ARB models shown in Figure 4-18 helps to demonstrate that the crystallinity of the model decreases with increased number of rolling cycles.

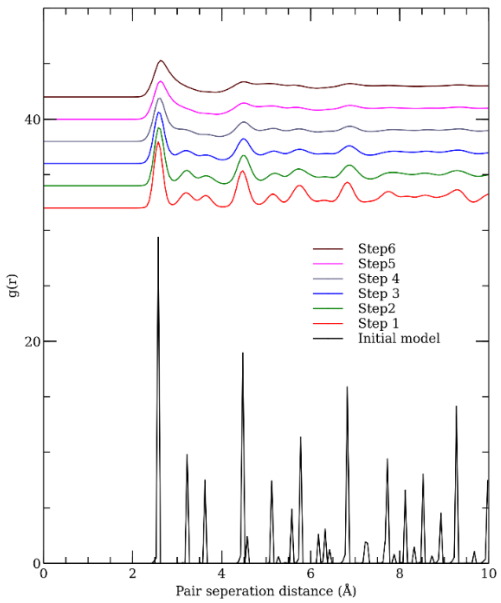

Figure 4-18: RDF analysis on different steps of rolling in MD simulation. The broadening of peaks indicates the disturbance of the crystalline lattice and the formation of diffused phases.

While the RDF analysis indicates sharp peaks in early steps of deformation (which is the sign of crystalline structure), the peak broadening at the higher number of rolling cycles is

associated with a more diffused structure. Such a transition supports the alloying and amorphization of the CuZr phases during the ARB process observed in both EDS and TEM experimental analysis. There are still island-like crystalline Zr particles following 6 cycles of rolling which is consistent with the presence of Zr particles inside the Cu matrix even after 10 cycles of rolling (Figure 4-5).

4.2.2 C-A Interface Structure

Figure 4-19 demonstrates the results of the potential energy distribution and normal stress along the Z axis (σ_{zz}) for a well-relaxed, representative C-A model with a (1 1 0) crystalline interface at the Cu layer (labelled as $C_{(1\ 1\ 0)}$-A). The results indicate that the distribution of both potential energy and σ_{zz} is uniform in each individual crystalline and amorphous phase of the $C_{(1\ 1\ 0)}$-A model. The relatively smooth transition for both parameters across the C-A interface is in sharp contrast with previous results of grain boundaries [102–104] and free surfaces [105]. This means the C-A interface did not impose any local spike in potential energy or stress distribution.

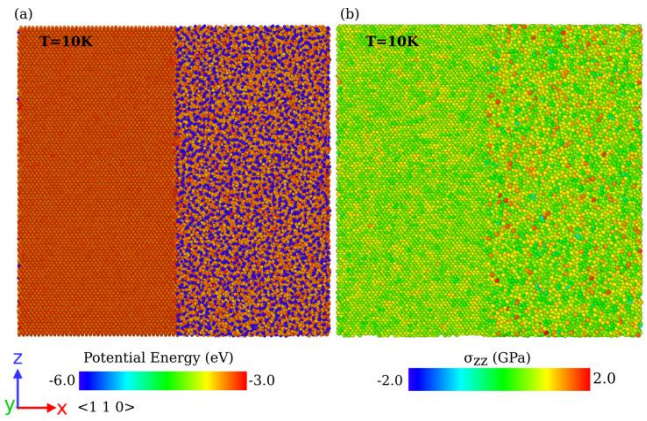

Figure 4-19: Representative (a) potential energy and (b) stress (σ_{zz}) distribution in C-A model with (1 1 0) oriented crystalline interface (C(1 1 0)-A) after relaxation.

4.2.2.1. Inter-Diffusion Analysis

The inter-diffusion of elements at the C-A interface during the heating and quenching relaxation procedure is identified as the reason for the smooth structural transition in Figure 4-19. The C-A models (described in *Chapter 3*) were used to investigate the inter-diffusion mechanisms under periodic boundary conditions. The atomic inter-diffusion at the C-A interface has been monitored by assigning different colors to the Cu atoms belonging to the original crystalline and amorphous layers prior to the relaxation. Figure 4-20 shows the atomic structure of a well-relaxed $C_{(1\ 1\ 0)}$-A interface as a representative model to explain the mechanisms which was observed in all orientations.

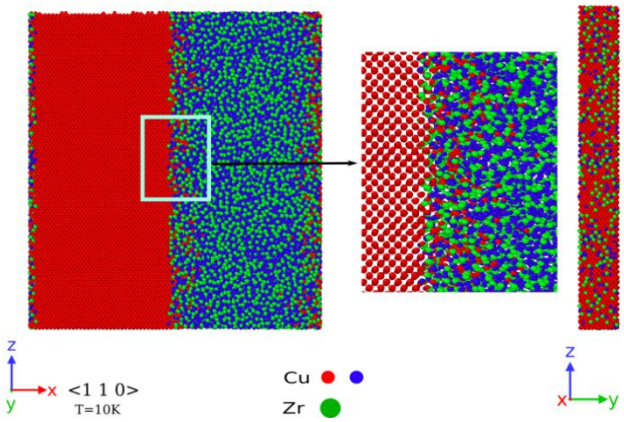

Figure 4-20: Representative atomic structure of the relaxed C-A interface. The zoomed-in image in the middle indicates atomic inter-diffusion across the interface. The right-side image is the cross section of the interface.

As shown in Figure 4-20, a number of Cu atoms that originally belonged to the crystalline layer (red atoms), have crossed the interface and moved to the amorphous layer. The same atomic movement can be observed in the zoomed-in image in Figure 4-20 for Zr, where few Zr atoms moved to the crystalline Cu layer. However, the number of diffused Zr atoms is lower than the migrated Cu atoms. One possible reason may be due to the atomic size of

Cu (empirical atomic radius ~ 128 pm) and Zr (empirical atomic radius ~ 160 pm). Also, the amorphous phase has a lower atomic packing density compared to the crystalline phase. Therefore, the diffusion of the bigger Zr atoms into the highly packed Cu layer becomes more difficult than the inter-diffusion of Cu atoms into the amorphous layer. This phenomenon can be also observed in cross-sectional image of the C-A interface in Figure 4-20; where the structure of the interface (close to the crystalline Cu layer) contains some Cu and Zr atoms, originally belonging to the amorphous layer.

Several quantitative analysis were also performed to study the inter-diffusion at the C-A interface. Two parameters including atomic density and composition were measured for three different C-A orientations based on the slicing procedure discussed in *Chapter 3*. The results for the three models i.e., $C_{(0\,0\,1)}$-A, $C_{(1\,1\,0)}$-A , and $C_{(1\,1\,1)}$-A are shown in Figure 4-21. The smooth transition for both parameters from the crystalline to the amorphous phase for all models is clear and highlighted in the gray rectangular box. The trend in transition for both atomic density and composition is the same for three different {1 1 0}, {1 1 1}, and {1 0 0} C-A interface planes (the curves for both parameters are located almost on top of each other). Although the atomic packing across these three C-A interface planes is dramatically different, a similar transition trend is the sign of a more diffused structure at the interface. The width of the relaxed C-A interface is roughly measured as 1 nm; which is the width of the transitional region of both parameters in the gray box. The interface width starts from ~ - 0.6 nm in the crystalline layer to ~ 0.4 nm of the amorphous layer. Herein, the original separation of crystalline Cu and amorphous CuZr layers is considered to be X = 0 Å.

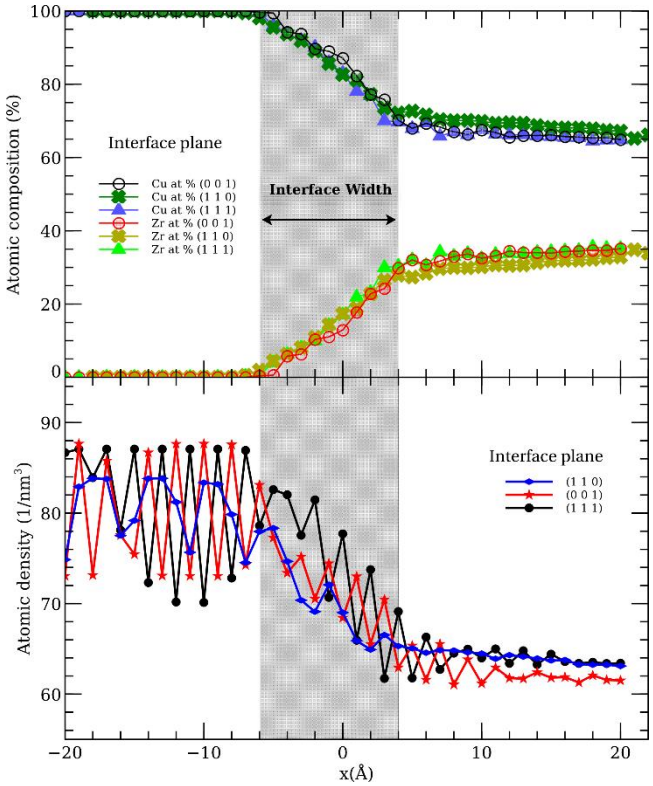

Figure 4-21: Composition (upper image) and atomic density analysis (lower image) across the C-A interface.

4.2.2.2. RDF and Voronoi Analysis

Considering a representative $C_{(1\ 1\ 0)}$-A model, RDF analysis was performed and is shown in Figure 4-22. The difference between the crystalline and amorphous layers can be easily detected through the presence of sharp peaks in the crystalline Cu layer; which is in contrast to the peak broadening in the amorphous CuZr layer. The sharp peaks in the crystalline layer gradually vanish in the interfacial region (middle figure), and the peak broadening occurs close to the amorphous layer. This interfacial analysis was performed using the same slicing strategy that was used in Figure 4-21. Similar to the atomic density and composition results, there is a smooth transition from ordered crystalline Cu layer, to the disordered

amorphous CuZr phase. The same transition is also reported in the MD analysis of crystalline Cu - amorphous $Cu_{46}Zr_{54}$ interface structures [76].

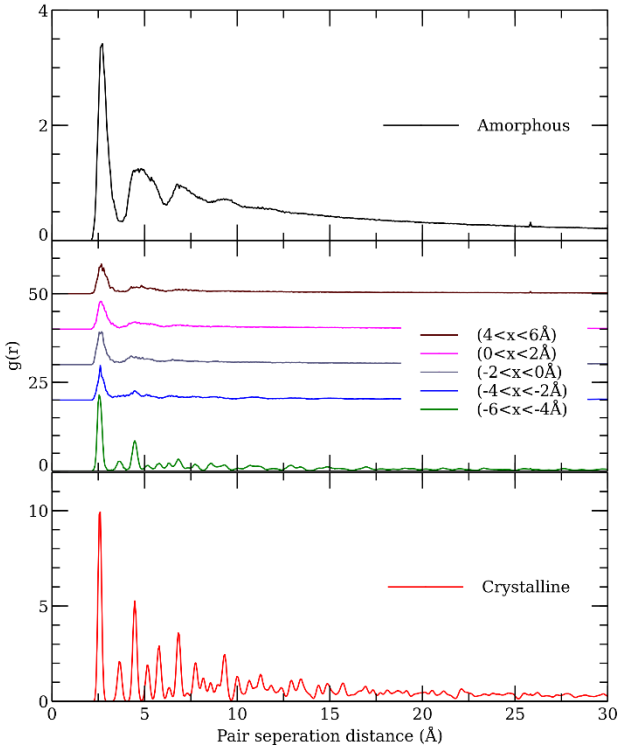

Figure 4-22: RDF analysis in crystalline (lower), amorphous (upper) and interface region (middle) in the $C_{(1\,1\,0)}$-A model.

Voronoi analysis was also performed on the same slices using Voro++ code [90], and the results of Cu-centered Voronoi polyhedral distribution are shown in Figure 4-23. The Schlaefli notation, a vector of indices $<n_3,n_4,\ldots,n_v>$ where n_i is the number of polyhedron faces with i edges, has been measured for each slice. The trend in results, indicated in Figure 4-23, shows the same transitions from highly ordered structure to less ordered structure around the interface that was observed in RDF analysis. More specifically, the crystalline Cu layer (X~-8 Å) has a high percentage of <0, 12, 0, 0> Cu-centered Voronoi index; which represents the coordination number of FCC pure Cu. However, the

high fraction of <0, 0, 12, 0> polyhedron can be observed in the amorphous $Cu_{63}Zr_{37}$ structure (X~10 Å) and is approximately 15% for all three orientations. The 15% fraction of the <0, 0, 12, 0> index in the amorphous layer is in well agreement with the value (around 20%) reported for a similar CuZr glass [106]. The inter-diffusion phenomenon (discussed in previous section), and possibly structural evolution (i.e. local crystallization), can be a reason that the lower <0, 0, 12, 0> index is observed in the current study. Meanwhile, the gradual decrease of crystalline Voronoi index (<0, 12, 0, 0>), as well as the increase of the amorphous <0, 0, 12, 0> index around the interface region, is another indication of the inter-diffusion phenomenon.

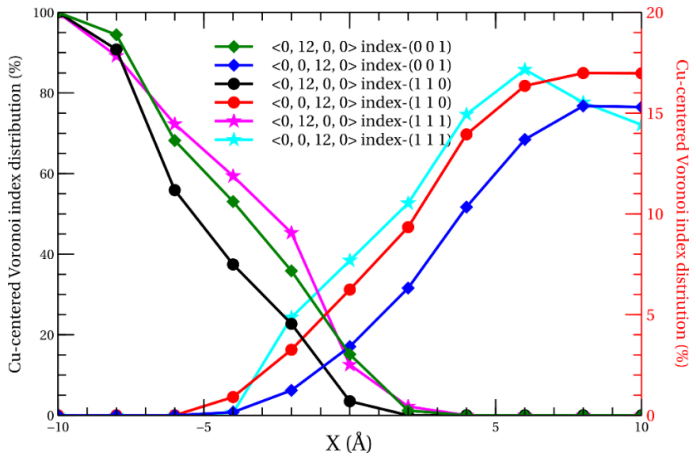

Figure 4-23: Voronoi Cu-centered polyhedral distribution around the C-A interfaces.

4.2.3 Interface Energy Analysis

C-A models were used to measure the interface energy at a temperature of 10 K and under periodic boundary condition. The γ_{int} for different orientations of the Cu layer was measured and are shown in Figure 4-24. For comparison purposes, the free surface energy (γ_{sur}) was also determined and is indicated in Figure 4-24. It is obvious that the results of

γ_{int} and γ_{sur} do not follow the same behavior. The amount of energy for the C-A interface is dramatically lower than the γ_{sur} for all orientations of the Cu layers. Such a lower energy is another evidence of less disturbance of the lattice structure at the C-A interface. In spite of the free surface energy results that showed a minimum value at the (1 1 1) plane, the (1 1 1) C-A interface plane has exhibited close value to some other orientations, e.g., (5 5 1), (5 5 2), (2 2 1), (1 1 2) and (1 1 4). Overall, the interface energy shows a weak dependence on the C-A interfacial plane orientation which is in well agreement with the composition analysis discussed previously in Figure 4-21.

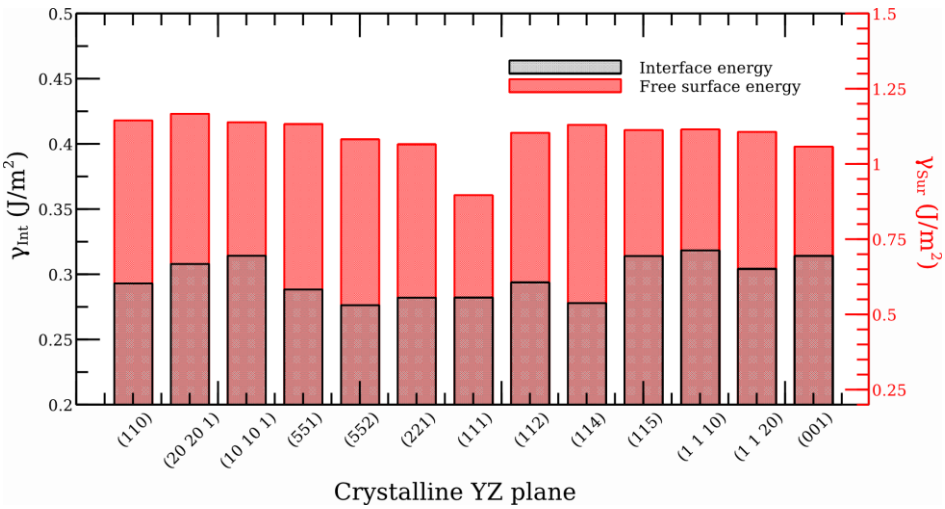

Figure 4-24: Interface (γ_{int}) and free surface (γ_{sur}) energy for C-A models with different crystalline orientations.

4.2.4 Interfacial Strength and Yielding Mechanisms under Tensile Deformation

4.2.4.1. *CRSS* Analysis

The influence of crystalline orientation on the mechanical behavior of C-A models under tensile loading has been studied using the *CRSS* parameter. Figure 4-25 indicates the variation trend in crystalline orientations at the C-A interface for different models.

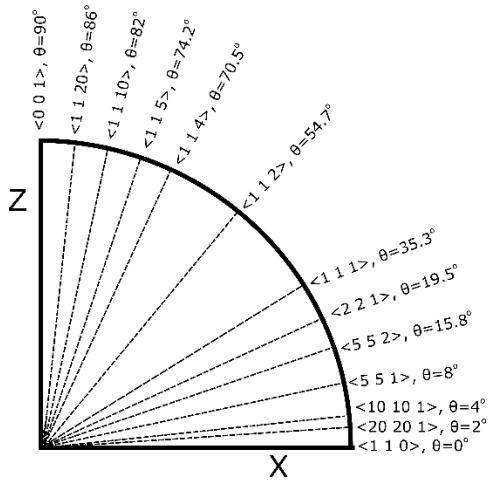

Figure 4-25: Schematic of variation of crystalline orientation at the C-A interface in different models.

The overall stress-strain curves from tensile simulation of the C-A models are shown in Figure 4-26 (a). The trend in results for elastic modulus demonstrates two distinct behaviors for different crystalline orientations. While several models indicate higher modulus (those models that are labeled with partial dislocation nucleation in Figure 4-26 (b)), the second group of C-A models, with full dislocation nucleation plasticity mechanisms in the crystalline layer, demonstrate a lower elastic modulus. The different elastic behavior is due to the transition in slip system of the C-A models from full to partial dislocation nucleation. The full dislocation nucleation is attributed to the condition in which a leading partial dislocation is followed immediately by a trailing partial on the same slip plane. In contrast, only partial dislocation will be shown if the leading partial is not followed by a trailing partial and instead, other leading partials are nucleated on parallel slip planes. The transition from full to partial dislocation nucleation is mainly determined by the crystalline orientation at the C-A interface. Specifically, the competition between full and partial dislocation nucleation is governed by the difference in Schmid factors for leading and trailing partials, which are strongly dependent on crystalline orientation [107]. If the

Schmid factor is higher for the trailing than the leading partials, the full dislocation nucleation will be activated - and vice versa. Such a transition from partial to full dislocation nucleation in Figure 4-26 is in well agreement with previous studies in FCC crystalline nanowires [107].

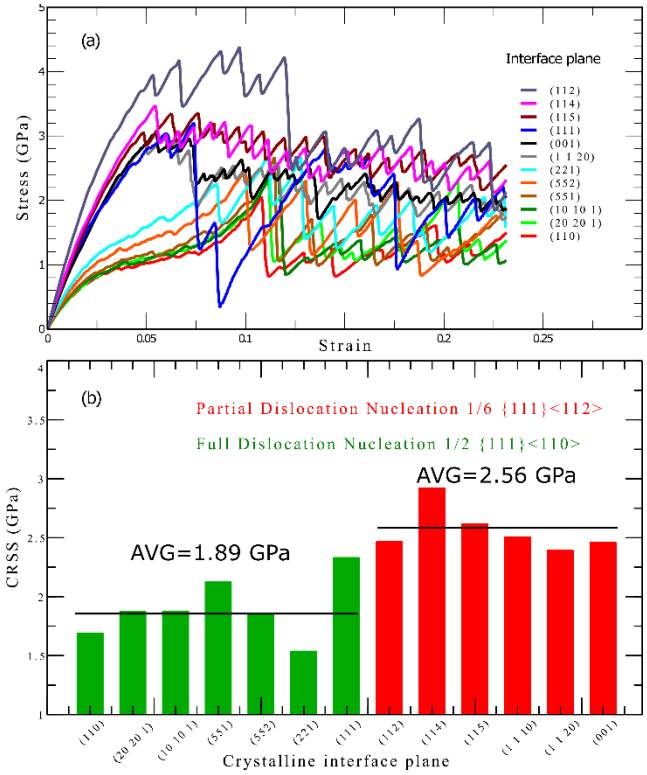

Figure 4-26: (a) Stress-strain curves from tensile simulation of C-A models with different crystalline orientations and (b) Orientation dependency of *CRSS* in the crystalline layer of C-A models.

The plastic deformation of C-A models indicates two different behaviors. While those models with partial dislocation nucleation show strain hardening after yielding, strain softening has been found in other models with full dislocation nucleation. Further microstructural analysis by OVITO reveals more details on hardening and softening behaviors where the impinging of dislocation propagation at the C-A interface is responsible for the strain hardening. Consequently, hardening can occur due to the pile up

of stacking faults and partial dislocations at the C-A interface. Absorption of dislocations at the C-A interface (as a dislocation sink) is also possible [108] which leads to another type of hardening called “starvation”. This type of hardening was introduced in FIB-milled metallic micro pillars under compression [109,110] to explain strain hardening. The wavy shape of the stress-strain curves for models with full dislocation nucleation in Figure 4-26 (a) can be explained by nucleation and absorption of secondary dislocations; which has been observed in these models (after yielding).

The transition in activated slip systems for different orientations of the C-A models is also clear in the *CRSS* results, shown in Figure 4-26 (b). Two distinct slip systems have been recognized in different C-A interface orientations: full dislocations (1/2 {1 1 1}<1 1 0>) for those orientations shown in green, and partial dislocations (1/6 {1 1 1} <1 1 2>) for those models in red. It is also clear from Figure 4-26 (b) that the orientation of the crystalline layer has a strong influence on the *CRSS* values, regardless of full or partial dislocation slip systems. Seeking for a reason for the *CRSS* dependence on interface orientation, it was found that the strain at which the first dislocation was nucleated is dramatically different for the full and partial slip events.

As indicated in the stress-strain results of Figure 4-27, the strain at which the first dislocation was nucleated (ε_{fd}) is different for C-A models with partial and full dislocation slip systems. Table 4-6 summarizes the values of strain at which the first dislocation was nucleated for all C-A models in Figure 4-26 (a). The C-A models with partial dislocation nucleation yielded at strain < 5% which is clear in Figure 4-27 (b) for $C_{(0\,0\,1)}$-A model. On the other hand, yield strain for those models with full dislocation nucleation was > 10%

that is shown in Figure 4-27 (a) for $C_{(1\ 1\ 0)}$-A model. The yielding mechanisms have not been changed in both models by changing the thickness of crystalline layer (t_c) from 2.5 to 10 nm, as indicated in Figure 4-27.

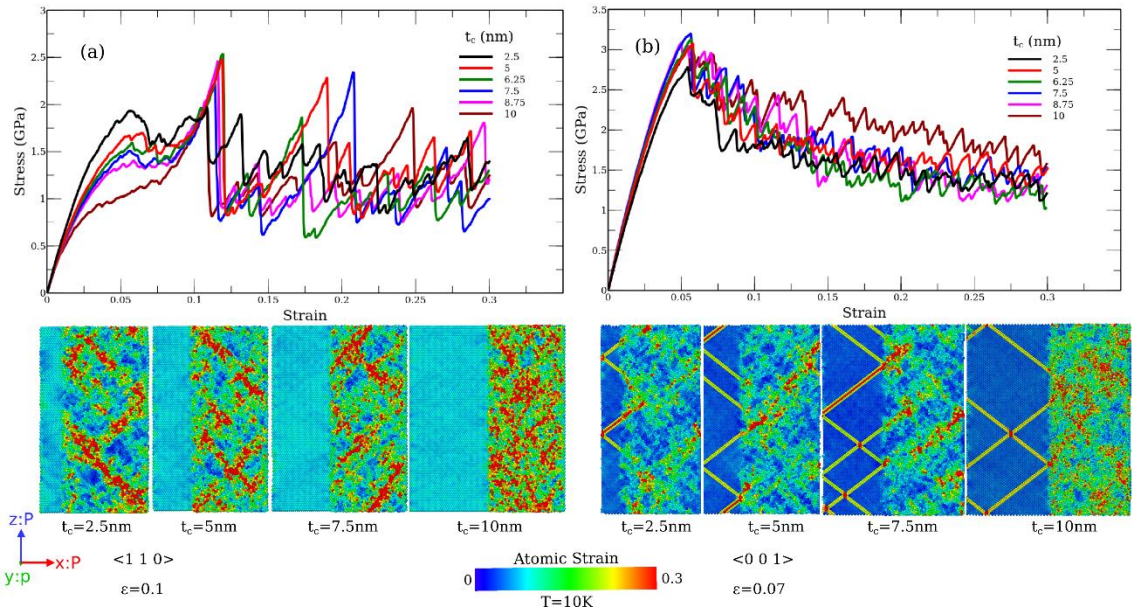

Figure 4-27: The overall stress-strain curves and failure mechanism in (a) $C_{(1\ 1\ 0)}$-A and (b) $C_{(0\ 0\ 1)}$-A models with different t_c. The atoms are colored according to the local atomic strain.

Table 4-6: Strain at which the first dislocation is nucleated (ε_{fd}) for C-A models.

Orientations with full dislocation nucleation	(1 1 0)	(20 20 1)	(10 10 1)	(5 5 1)	(5 5 2)	(2 2 1)	(1 1 1)
ε_{fd}	**10.8**	**11.1**	**11.55**	**11.4**	**10**	**8.45**	**6.1**
Orientations with partial dislocation nucleation	(1 1 2)	(1 1 4)	(1 1 5)	(1 1 10)	(1 1 20)	(0 0 1)	
ε_{fd}	**5.3**	**5.4**	**4.85**	**5.1**	**5**	**5.5**	

Overall, the onset of plasticity is not the same within these two groups of C-A models. Shear localization occurs in the amorphous layer before the dislocation initiation in the crystalline layer for C-A models governed by full dislocation nucleation. However,

dislocations have been nucleated prior to shear localization for models with partial dislocation slip systems.

The stereographic triangle of Figure 4-28 has been used to summarize the orientation-dependent deformation behaviors of C-A models, and their correlation with the activated slip system in crystalline layers (full or partial dislocation nucleation). This stereographic figure is constructed on the basis of loading orientation. Table 4-7 provides data on the correlation between the interface plane and loading orientation.

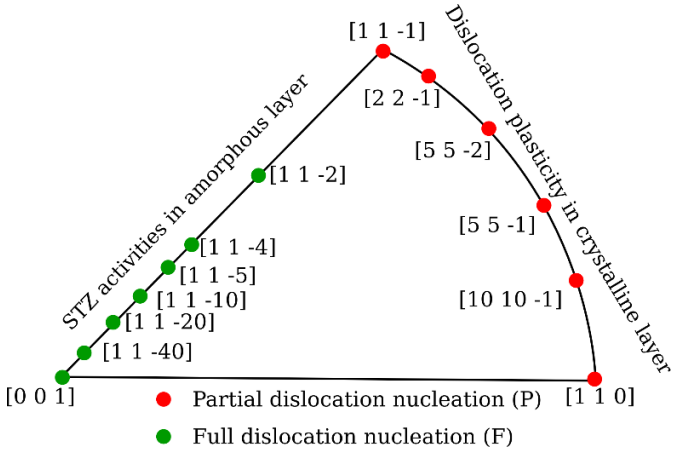

Figure 4-28: Stereographic triangle summarizing the orientation dependent behavior of C-A models.

Table 4-7: The relation between C-A interface plane orientations and loading direction.

Interface plane	Loading direction	Slip system
(1 1 0)	[0 0 1]	Full
(20 20 1)	[1 1 -40]	Full
(10 10 1)	[1 1 -20]	Full
(5 5 1)	[1 1 -10]	Full
(5 5 2)	[1 1 -5]	Full
(2 2 1)	[1 1 -4]	Full
(1 1 1)	[1 1 -2]	Full
(1 1 2)	[1 1 -1]	Partial
(1 1 4)	[2 2 -1]	Partial
(1 1 5)	[5 5 -2]	Partial
(1 1 10)	[5 5 -1]	Partial
(1 1 20)	[10 10 -1]	Partial
(0 0 1)	[1 1 0]	Partial

4.2.4.2. Effects of Texturing and Grain Boundaries

As discussed in *Chapter 2*, both experimental and numerical investigation have shown the importance of C-A interface on the yielding behavior of crystalline Cu- amorphous CuZr composites. In addition, formation of both crystalline and amorphous CuZr phases during the ARB process, and the subsequent presence of C-A interfaces, has been discussed in *Section 4.1*. Therefore, a multilayer crystalline Cu- amorphous CuZr MD model has also been built by MD in order to study the fundamental yielding micromechanisms in C-A composites in the presence of C-A interfaces. Since polycrystalline phases are mostly observed in experimentally synthesized metallic C-A composites, the major focus of this section of work is to investigate the effects of texturing orientations on the deformation behavior of A-NC-A models with columnar polycrystalline layers (referred as A-$NC_{<0\,0\,1>}$-A and A-$NC_{<1\,1\,1>}$-A).

The yielding process in the presence of a free surface boundary (along X axis) was investigated for the A-$NC_{<0\,0\,1>}$-A model. Figure 4-29 (a) and (b) provide a snapshot of the plastic deformation around the C-A interface at strain of 10% in the crystalline and amorphous layers. The initiation of dislocations at the grain boundaries, as well as the emerging high strain areas (collection of STZs) in the amorphous layer due to dislocation activities, can be observed in Figure 4-29 (a) and (b), respectively. Similar coupling mechanisms between dislocations and STZs were also reported in the work of Cheng and Trelewicz [78].

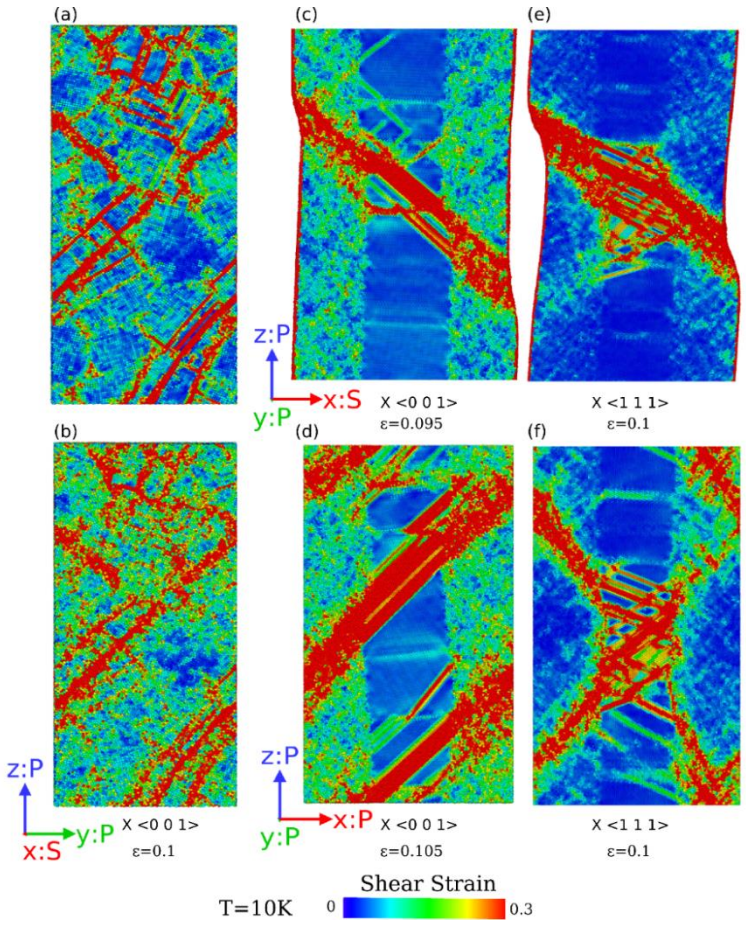

Figure 4-29: Cross-section of the (a) crystalline and (b) amorphous layer in the A-NC<0 0 1>-A model at the onset of plasticity under tensile loading. Yielding in the (c) A-NC<0 0 1>-A model with x:S, y:P, z:P and (d) x:P, y:P, z:P boundary conditions and (e) C<1 1 1>-A model with x:S, y:P, z:P and (f) x:P, y:P, z:P boundary conditions. Here S and P represent free (shrink-wrapped) and periodic boundary conditions. The atoms are colored according to the local atomic strain.

In the next step, the plasticity mechanisms of the A-NC-A models were studied under two different boundary and loading conditions. Firstly, the model was loaded by applying free surface condition (shrink-wrap) along the X axis, and a fixed sample size in the Y dimension. The results for the A-NC$_{<0\ 0\ 1>}$-A model, outlined in Figure 4-29 (c), indicate the localization of plasticity through strong shear banding in both crystalline and amorphous layers. The results are in good agreement with the experimental data on synthesized C-A multilayer thin films [71]; where strong shear banding was reported in

both crystalline and amorphous layers. In order to simulate the bulk material's behavior, the fully periodic boundary condition was applied. For comparison purposes, such periodic conditions were used for tensile simulation of the A-NC$_{<0\ 0\ 1>}$-A model and is shown in Figure 4-29 (d). The shrinkage of the model was allowed in both X and Y dimensions to keep the overall volume of the model constant during tensile loading along the Z direction. Similar results were found in that strong shear banding was observed across both layers.

In order to investigate the texturing effects on the deformation behavior, similar boundary conditions and loading states were used to simulate tensile loading on the A-NC$_{<1\ 1\ 1>}$-A model. The results, shown in Figure 4-29 (e), reveal the formation of a shear band in the A-NC$_{<1\ 1\ 1>}$-A model. However, in contrast to the A-NC$_{<0\ 0\ 1>}$-A model (Figure 4-29 (c)), the dislocations in the polycrystalline Cu layer and the shear banding in the amorphous layer are not well aligned with each other in the A-NC$_{<1\ 1\ 1>}$-A model. Particularly, some of the dislocations in the Cu layer intersect with the main shear band in the amorphous layer of the A-NC$_{<1\ 1\ 1>}$-A model; while the shear band and slip systems are parallel to each other in the A-NC$_{<0\ 0\ 1>}$-A model. Simulation results of the periodic boundary condition with the same loading state are displayed in Figure 4-29 (f), and demonstrate the appearance of two major shear bands for the A-NC$_{<1\ 1\ 1>}$-A model; while there is only one major shear band in the A-NC$_{<0\ 0\ 1>}$-A model (Figure 4-29 (d)). Meanwhile, both models under periodic boundary conditions showed a number of slip intersections. These findings demonstrate the influences of crystalline orientations on the plasticity of C-A composites.

The alignment of slip and shear banding planes in crystalline and amorphous layers respectively, play a significant role in avoiding shear localization in C-A composites. The

interaction between shear localization and dislocation activities can be constructive or destructive. Constructive interaction occurs when the activated slip system in the crystalline layer impinges the shear band propagation at the C-A interface. Such a constructive interaction occurs due to the misalignment of the shear banding plane and slip plane. It was shown that the shear banding plane has an inclination angle of ~ 45°, relative to the uniaxial loading direction in amorphous MGs [8]. On the other hand, depending on the crystalline orientation, the angle between activated slip plane and loading direction might take on different values. In the present A-NC-A models, the misorientation angle between slip plane and loading axis was 35.3^{o} and 70.5^{o} for the A-NC$_{<0\,0\,1>}$-A and A-NC$_{<1\,1\,1>}$-A models, respectively. As a result of the well alignment between the slip plane and the shear banding inclination angle in the A-NC$_{<0\,0\,1>}$-A model, strong shear localization in both crystalline and amorphous layers were found to occur in this model. Meanwhile, the slip plane (with angle of 70.5^{o} relative to the loading direction) is not aligned with the shear banding plane (45° misorientation angle with loading axis) in the A-NC$_{<1\,1\,1>}$-A model. Consequently, a constructive interaction can occur that avoids shear localization in both crystalline and amorphous layers. The results of the A-NC$_{<1\,1\,1>}$-A model (Figure 4-29 (e) and (f)) reveal that by controlling the texturing orientation in the columnar grains, a more uniform deformation can be achieved by avoiding shear localization. TEM analysis have shown that shear bands in the amorphous layer can occur on planes parallel to the {1 1 1} slip system in the crystalline phase for a sputtered multilayer Cu/CuZr composite [111]. The MD observations in this section on the effects of crystalline orientation on the interaction between STZs and dislocations at the interface, are in good agreement with this experimental data.

Chapter 5 : Conclusions and Recommendations

The purpose of the current research was to develop an ARB guideline for the synthesis of C-A composites in Cu-Zr alloy systems. Different instrumentation techniques were used to study the microstructural characteristics of synthesized samples. In addition to experimental studies, fundamental investigation of the micromechanisms and structure-property relations were carried out using an atomistic MD numerical method.

Briefly, the systematic study on the ARB parameters provided a guideline which answer questions regarding the operational conditions required for the alloying and amorphization of CuZr phases during the ARB process. The bonding of Cu-Zr multilayers - and the corresponding parameters such as surface roughness, thickness ratio and percent reduction - were studied initially. Then, the factors which influence the alloying and amorphization of CuZr phases (i.e. annealing parameters) were investigated by using various microstructural characterization techniques. Mechanical testing by nanoindentation was also performed on the ARB samples to investigate their mechanical properties, such as elastic modulus and hardness for the different phases. Overall, the first and second objectives of this research have been met by providing an ARB guideline regarding the

synthesis of bulk metallic C-A Cu-Zr composites and mechanical testing by nanoindentation.

Regarding the third objective, numerical MD results indicated that the inter-diffusion of Cu and Zr elements is the primary alloying mechanism during the ARB process. Moreover, the effects of crystalline orientation on the yielding micromechanisms of crystalline Cu – amorphous CuZr composites were studied for the first time in this research. The results shed some light on possible plasticity micromechanisms: including STZs and dislocations, the occurrence of each yielding mechanisms, and the influence of crystalline orientation on the mutual interactions between these mechanisms.

5.1 Main Findings

A summary of both experimental and numerical findings in the current work are summarized as follows:

- It was found that the surface treatment, surface cleaning and brushing, are important in establishing crystalline Cu-Zr multilayer bonding. Furthermore, the thickness ratio between Cu and Zr (t_{Cu}/t_{Zr}) layers was identified as another influencing parameter in multilayer bonding; which was established to be around 3 to achieve a strong level of bonding. The best configuration was achieved with a 7 multilayer structure. A minimum thickness reduction of around 50 % was also required to bond the Cu-Zr multilayers during the rolling procedure. An efficient thickness reduction range was identified as ~ 49 to 62 %. Finally, the intermediate heat treatment was necessary to recover the material ductility, which is significant in the accumulative

rolling procedure. The effective annealing temperature range was determined to be between 350 ºC to 700 ºC.

- EDS results illustrated the presence of pure Cu, pure Zr and several compositions of CuZr phases ($Cu_{38}Zr_{62}$, $Cu_{50}Zr_{50}$ and $Cu_{62}Zr_{38}$) which were formed during the ARB process. TEM analysis with electron diffraction confirmed the presence of both amorphous and crystalline $CuZr_2$ phases. Moreover, TEM results demonstrated that the amorphization of CuZr phases during the ARB process is more likely to occur at an annealing temperature lower than the crystallization temperature, i.e. 350 ºC.
- The nanoindentation results showed the highest hardness of ~ 8 GPa for the formed CuZr phases; while the corresponding values for the Cu and Zr phases were ~ 2.2 and 4.4 GPa, respectively. Apart from the higher hardness values, the pop-in feature was observed in load-displacement curves of CuZr phases in samples with an annealing temperature of 350 ºC. The presence of spots with and without pop-in features in load-displacement curves (representing both amorphous and crystalline regions) confirmed the ultrafine structure of CuZr phases - which was observed in TEM analysis for this sample.
- MD simulation of the ARB process showed that the amorphization of the crystalline phase occurred during accumulative rolling of the Cu-Zr multilayers. Atomic structural analysis such as atomic density, composition, RDF and Voronoi results revealed strong inter-diffusion across the C-A interface. Consequently, the interfacial energy data demonstrated almost no dependence on the crystalline

orientations; in which is in contrast to other types of interfacial defects such as grain boundaries and free surfaces.

- MD results indicated a strong dependence of *CRSS* on the orientation of the interface planes. While dislocation nucleation in the crystalline layer was responsible for plasticity in models with a partial slip system, the shear localization through STZ activities occurred prior to dislocation nucleation in C-A models with a full dislocation slip. Moreover, highly localized shear banding in both crystalline and amorphous layers were found where the slip plane and shear banding plane were well-aligned with each other.

5.2 Concluding Remarks

Considering the research hypotheses in section 1.2, the concluding remarks are stated as follows:

- It was found that without performing intermediate heat treatment, bonding of commercially available Cu-Zr multilayers cannot occur. That means modification of ARB process by implementing annealing procedure was successfully led to the large deformation strain (considerable number of ARB passes) in commercial Cu-Zr multilayers. Furthermore, formation of CuZr phases occurred in early stage of the ARB process which indicated that heat treatment facilitates mechanical alloying.
- It was found that the annealing temperature is an influencing factor on amorphization of CuZr phases during the ARB process. Heat treatment at temperature below the crystallization range led to more volume fraction of

amorphous CuZr phases. The TEM analysis indicated ultrafine structure where amorphous $CuZr_2$ regions were formed adjacent to the nanocrystalline $CuZr_2$ particles, which is because of annealing process in modified ARB procedure.

- It was also found that the plasticity of C-A composites is influenced by the crystalline orientation at the C-A interface. The crystalline orientation influenced the interaction between the slip plane in the crystalline layer, and shear banding plane in the amorphous layer. Consequently, either highly localized or more uniform shear deformation occurred in C-A composites depending on the crystalline orientation.

5.3 Recommendations for Future Works

The current research has highlighted a number of topics which merit further investigation. The observations, limitations and characteristic analysis from both experimental and numerical studies has provided suggestions and recommendations for future work.

One of the main limitations in the current study was the purity of the starting materials. It is suggested to study the influence of high purity Zr sheets on the structure of synthesized composites. It is expected that Zr sheets with lower contents of impurities exhibit higher ductility. As a result, different elongation rates of highly pure Cu and Zr layers might lead to a different structure, i.e. lamellar configuration. Furthermore, application of Zr sheets with high purity along with intermediate annealing might increase the possibility of performing the ARB to a higher number of passes (for instance more than 50 passes). This can lead to a higher volume fraction of alloyed CuZr phases.

The other limitation during the ARB process is the occurrence of severe damage i.e. cracking due to the heavy state of deformation by cold working. One possible alternative option can be the application of hot rolling to eliminate such defects. Thermally activated mechanisms during hot rolling can be beneficial in multilayer bonding, mechanical alloying mechanisms and crack healing processes. Therefore, hot rolling is a potential technique in the synthesis of bulk C-A composites with a lower density of defects such as cracks and voids.

Finally, the application of recent techniques in the investigation of microstructures might be beneficial in revealing the fundamental characteristics and micromechanisms of C-A interface. Particularly, sample preparation for TEM analysis is an important (and at the same time challenging) step. The electro-polishing method, used in this study for sample preparation, is a blind technique which does not allow control over selecting the desired regions for TEM analysis. Focused ion beam (FIB) is a TEM sample preparation technique which enables the user to select a specific region for TEM analysis. Considering various CuZr compositions detected in the EDS analysis in the current thesis, application of FIB can be useful in structural analysis for each identified CuZr phase formed during the ARB process.

References

[1] C. Suryanarayana, A. Inoue, Bulk metallic glasses, CRC, Boca Raton, Fla., 2011.

[2] Douglas C. Hofmann, Bulk Metallic Glasses and Their Composites: A Brief History of Diverging Fields, J. Mater. 2013 (2013) 8. doi:10.1155/2013/517904.

[3] G. Wang, J. Shen, J.F. Sun, Z.P. Lu, Z.H. Stachurski, B.D. Zhou, Tensile fracture characteristics and deformation behavior of a Zr-based bulk metallic glass at high temperatures, Intermetallics. 13 (2005) 642–648. doi:10.1016/j.intermet.2004.10.011.

[4] J.S. Langer, Shear-transformation-zone theory of deformation in metallic glasses, Viewp. Set No 37 Mech. Behav. Met. Glas. Set No 37 Mech. Behav. Met. Glas. 54 (2006) 375–379. doi:10.1016/j.scriptamat.2005.10.005.

[5] M.Q. Jiang, W.H. Wang, L.H. Dai, Prediction of shear-band thickness in metallic glasses, Scr. Mater. 60 (2009) 1004–1007. doi:10.1016/j.scriptamat.2009.02.039.

[6] Z. Zhu, H. Zhang, Z. Hu, W. Zhang, A. Inoue, Ta-particulate reinforced Zr-based bulk metallic glass matrix composite with tensile plasticity, Scr. Mater. 62 (2010) 278–281. doi:10.1016/j.scriptamat.2009.11.018.

[7] Y. Wang, J. Li, A.V. Hamza, T.W. Barbee, Ductile crystalline–amorphous nanolaminates, Proc. Natl. Acad. Sci. 104 (2007) 11155–11160. doi:10.1073/pnas.0702344104.

[8] C.C. Hays, C.P. Kim, W.L. Johnson, Microstructure Controlled Shear Band Pattern Formation and Enhanced Plasticity of Bulk Metallic Glasses Containing in situ Formed Ductile Phase Dendrite Dispersions, Phys. Rev. Lett. (2000). doi:10.1103/PhysRevLett.84.2901.

[9] Y.F. Sun, N. Tsuji, H. Fujii, F.S. Li, Cu/Zr nanoscaled multi-stacks fabricated by accumulative roll bonding, 16th Int. Symp. Metastable Amorph. Nanostructured Mater. 504, Supplement 1 (2010) S443–S447. doi:10.1016/j.jallcom.2010.02.201.

[10] S. Ohsaki, S. Kato, N. Tsuji, T. Ohkubo, K. Hono, Bulk mechanical alloying of Cu–Ag and Cu/Zr two-phase microstructures by accumulative roll-bonding process, Acta Mater. 55 (2007) 2885–2895. doi:10.1016/j.actamat.2006.12.027.

[11] E. Cerreta, G.T. Gray, R.S. Hixson, P.A. Rigg, D.W. Brown, The influence of interstitial oxygen and peak pressure on the shock loading behavior of zirconium, Acta Mater. 53 (2005) 1751–1758. doi:10.1016/j.actamat.2004.12.024.

[12] M.C. Liu, J.C. Huang, H.S. Chou, Y.H. Lai, C.J. Lee, T.G. Nieh, A nanoscaled underlayer confinement approach for achieving extraordinarily plastic amorphous thin film, Scr. Mater. 61 (2009) 840–843. doi:10.1016/j.scriptamat.2009.07.010.

[13] T.G. Nieh, J. Wadsworth, Bypassing shear band nucleation and ductilization of an amorphous–crystalline nanolaminate in tension, Intermetallics. 16 (2008) 1156–1159. doi:10.1016/j.intermet.2008.06.018.

[14] W. Guo, E.A. Jägle, P.-P. Choi, J. Yao, A. Kostka, J.M. Schneider, D. Raabe, Shear-Induced Mixing Governs Codeformation of Crystalline-Amorphous Nanolaminates, Phys Rev Lett. 113 (2014) 035501. doi:10.1103/PhysRevLett.113.035501.

[15] W.D. Callister, D.G. Rethwisch, Materials science and engineering : an introduction, 2014.

[16] J. Weertman, J.R. Weertman, Elementary dislocation theory, Oxford University Press, New York, 1992.

[17] D. Louër, Powder X-Ray Diffraction, Applications* A2 - Lindon, John C., in: Encycl. Spectrosc. Spectrom. Second Ed., Academic Press, Oxford, 1999: pp. 2253–2262. doi:10.1016/B978-0-12-374413-5.00257-8.

[18] D. Chandler, Introduction to modern statistical mechanics, Oxford University Press, New York, 1987.

[19] W. KLEMENT, R.H. WILLENS, P. DUWEZ, Non-crystalline Structure in Solidified Gold-Silicon Alloys, Nature. 187 (1960) 869–870. doi:10.1038/187869b0.

[20] M.F. Ashby, A.L. Greer, Metallic glasses as structural materials, Viewp. Set No 37 Mech. Behav. Met. Glas. Set No 37 Mech. Behav. Met. Glas. 54 (2006) 321–326. doi:10.1016/j.scriptamat.2005.09.051.
[21] D.B. Miracle, Metallic glasses: Fast track to production, Nat Mater. 13 (2014) 432–433.
[22] H.F. Zhou, C. Zhong, Q.P. Cao, S.X. Qu, X.D. Wang, W. Yang, J.Z. Jiang, Non-localized deformation in metallic alloys with amorphous structure, Acta Mater. 68 (2014) 32–41. doi:10.1016/j.actamat.2014.01.003.
[23] J. Gao, J. Sharp, D. Guan, W.M. Rainforth, I. Todd, New compositional design for creating tough metallic glass composites with excellent work hardening, Acta Mater. 86 (2015) 208–215. doi:10.1016/j.actamat.2014.11.055.
[24] W. Kauzmann, The Nature of the Glassy State and the Behavior of Liquids at Low Temperatures., Chem. Rev. 43 (1948) 219–256. doi:10.1021/cr60135a002.
[25] D. Turnbull, Under what conditions can a glass be formed?, Contemp. Phys. 10 (1969) 473–488. doi:10.1080/00107516908204405.
[26] A.A. Valladares, J.A. Díaz-Celaya, J. Galván-Colín, L.M. Mejía-Mendoza, J.A. Reyes-Retana, R.M. Valladares, A. Valladares, F. Alvarez-Ramirez, D. Qu, J. Shen, New Approaches to the Computer Simulation of Amorphous Alloys: A Review, Materials. 4 (2011). doi:10.3390/ma4040716.
[27] E.A. Lazar, J. Han, D.J. Srolovitz, Topological framework for local structure analysis in condensed matter, Proc. Natl. Acad. Sci. 112 (2015) E5769. doi:10.1073/pnas.1505788112.
[28] M. Kumar, Atomistic Investigation of the Structural, Transport, and Mechanical Properties of Cu-Zr Metallic Glasses, Universtiy of Toronto, 2016. http://hdl.handle.net/1807/75093.
[29] A.S. Argon, H.Y. Kuo, Plastic flow in a disordered bubble raft (an analog of a metallic glass), Mater. Sci. Eng. 39 (1979) 101–109. doi:10.1016/0025-5416(79)90174-5.
[30] C.A. Schuh, T.C. Hufnagel, U. Ramamurty, Mechanical behavior of amorphous alloys, Acta Mater. 55 (2007) 4067–4109. doi:10.1016/j.actamat.2007.01.052.
[31] W.L. Johnson, K. Samwer, A Universal Criterion for Plastic Yielding of Metallic Glasses with a $(T/T_g)^2/3$ Temperature Dependence, Phys Rev Lett. 95 (2005) 195501. doi:10.1103/PhysRevLett.95.195501.
[32] F. Spaepen, A microscopic mechanism for steady state inhomogeneous flow in metallic glasses, Acta Metall. 25 (1977) 407–415. doi:10.1016/0001-6160(77)90232-2.
[33] H. Kimura, T. Masumoto, A model of the mechanics of serrated flow in an amorphous alloy, Acta Metall. 31 (1983) 231–240. doi:10.1016/0001-6160(83)90100-1.
[34] S. Pauly, G. Liu, S. Gorantla, G. Wang, U. Kühn, D.H. Kim, J. Eckert, Criteria for tensile plasticity in Cu–Zr–Al bulk metallic glasses, Acta Mater. 58 (2010) 4883–4890. doi:10.1016/j.actamat.2010.05.026.
[35] Z. Ning, W. Liang, M. Zhang, Z. Li, H. Sun, A. Liu, J. Sun, High tensile plasticity and strength of a CuZr-based bulk metallic glass composite, Mater. Des. 90 (2016) 145–150. doi:10.1016/j.matdes.2015.10.117.
[36] A. Inoue, B.L. Shen, A.R. Yavari, A.L. Greer, Mechanical properties of Fe-based bulk glassy alloys in Fe–B–Si–Nb and Fe–Ga–P–C–B–Si systems, J. Mater. Res. 18 (2003) 1487–1492. doi:10.1557/JMR.2003.0205.
[37] Y.-K. Xu, H. Ma, J. Xu, E. Ma, Mg-based bulk metallic glass composites with plasticity and gigapascal strength, Acta Mater. 53 (2005) 1857–1866. doi:10.1016/j.actamat.2004.12.036.
[38] C.A. Schuh, T.G. Nieh, A nanoindentation study of serrated flow in bulk metallic glasses, Acta Mater. 51 (2003) 87–99. doi:10.1016/S1359-6454(02)00303-8.
[39] Y. Shi, M.L. Falk, Stress-induced structural transformation and shear banding during simulated nanoindentation of a metallic glass, Acta Mater. 55 (2007) 4317–4324. doi:10.1016/j.actamat.2007.03.029.

[40] B.J. Alder, T.E. Wainwright, Studies in Molecular Dynamics. I. General Method, J. Chem. Phys. 31 (1959) 459–466. doi:10.1063/1.1730376.
[41] D.C. Rapaport, The art of molecular dynamics simulation, (2004). http://dx.doi.org/10.1017/CBO9780511816581.
[42] G. Raabe, Introduction to Statistical Mechanics, in: G. Raabe (Ed.), Mol. Simul. Stud. Thermophys. Prop. Appl. Work. Fluids, Springer Singapore, Singapore, 2017: pp. 5–30. doi:10.1007/978-981-10-3545-6_2.
[43] P. Lowhaphandu, J.J. [Case W.R.U. Lewandowski Cleveland, OH (United States)], Fracture toughness and notched toughness of bulk amorphous alloy: Zr-Ti-Ni-Cu-Be, Scr. Mater. (1998). doi:10.1016/S1359-6462(98)00102-X.
[44] A.H. Brothers, D. Dunand, Amorphous metal foams, 2005. doi:10.1016/j.scriptamat.2005.10.048.
[45] J. Schroers, W.L. Johnson, Ductile Bulk Metallic Glass, Phys. Rev. Lett. 93 (2004) 255506.
[46] D. Xu, B. Lohwongwatana, G. Duan, W.L. Johnson, C. Garland, Bulk metallic glass formation in binary Cu-rich alloy series – Cu100−xZrx (x=34, 36, 38.2, 40 at.%) and mechanical properties of bulk Cu64Zr36 glass, Acta Mater. 52 (2004) 2621–2624. doi:10.1016/j.actamat.2004.02.009.
[47] P. Franke, D. Neuschütz, P. Franke, D. Neuschütz, Binary systems. Part 3: Binary Systems from Cs-K to Mg-Zr · Cu-Zr: Datasheet from Landolt-Börnstein - Group IV Physical Chemistry · Volume 19B3: "Binary systems. Part 3: Binary Systems from Cs-K to Mg-Zr" in SpringerMaterials (https://dx.doi.org/10.1007/10757413_24), Springer-Verlag Berlin Heidelberg, n.d. doi:10.1007/10757413_24.
[48] F. Szuecs, C.P. Kim, W.L. Johnson, Mechanical properties of Zr56.2Ti13.8Nb5.0Cu6.9Ni5.6Be12.5 ductile phase reinforced bulk metallic glass composite, Acta Mater. 49 (2001) 1507–1513. doi:10.1016/S1359-6454(01)00068-4.
[49] M.L. Lee, Y. Li, C.A. Schuh, Effect of a controlled volume fraction of dendritic phases on tensile and compressive ductility in La-based metallic glass matrix composites, Acta Mater. 52 (2004) 4121–4131. doi:10.1016/j.actamat.2004.05.025.
[50] A. Inoue, W. Zhang *, T. Tsurui, A.R. Yavari, A.L. Greer, Unusual room-temperature compressive plasticity in nanocrystal-toughened bulk copper-zirconium glass, Philos. Mag. Lett. 85 (2005) 221–237. doi:10.1080/09500830500197724.
[51] G. He, W. Löser, J. Eckert, In situ formed Ti–Cu–Ni–Sn–Ta nanostructure-dendrite composite with large plasticity, Acta Mater. 51 (2003) 5223–5234. doi:10.1016/S1359-6454(03)00386-0.
[52] H. Skliarova, O. Azzolini, R.R. Johnson, V. Palmieri, Co-sputtered amorphous Nb–Ta, Nb–Zr and Ta–Zr coatings for corrosion protection of cyclotron targets for [18F] production, J. Alloys Compd. 639 (2015) 488–495. doi:10.1016/j.jallcom.2015.03.181.
[53] C.J. Chen, J.C. Huang, H.S. Chou, Y.H. Lai, L.W. Chang, X.H. Du, J.P. Chu, T.G. Nieh, On the amorphous and nanocrystalline Zr–Cu and Zr–Ti co-sputtered thin films, 14th Int. Symp. Metastable Nano-Mater. ISMANAM-2007. 483 (2009) 337–340. doi:10.1016/j.jallcom.2008.07.188.
[54] P. Carson, C. Mumford, 3 - General principles of chemistry, in: Hazard. Chem. Handb. Second Ed., Butterworth-Heinemann, Oxford, 2002: pp. 21–44. doi:10.1016/B978-075064888-2/50004-9.
[55] E. Chen, Thin Film Deposition, (2004). http://www.mrsec.harvard.edu/education/ap298r2004/Erli%20chenFabrication%20II%20-%20Deposition-1.pdf.
[56] Y. Cui, O.T. Abad, F. Wang, P. Huang, T.-J. Lu, K.-W. Xu, J. Wang, Plastic Deformation Modes of CuZr/Cu Multilayers, Sci. Rep. 6 (2016) 23306.

[57] Y. Saito, N. Tsuji, H. Utsunomiya, T. Sakai, R. Hong G., Ultrafine grained bulk aluminum produced by accumulative roll-bonding (ARB) process, Scr. Mater. 39 (1998) 1221–1227. doi:10.1016/S1359-6462(98)00302-9.
[58] M.M. Mahdavian, L. Ghalandari, M. Reihanian, Accumulative roll bonding of multilayered Cu/Zn/Al: An evaluation of microstructure and mechanical properties, Mater. Sci. Eng. A. 579 (2013) 99–107. doi:10.1016/j.msea.2013.05.002.
[59] A. Mozaffari, H. Danesh Manesh, K. Janghorban, Evaluation of mechanical properties and structure of multilayered Al/Ni composites produced by accumulative roll bonding (ARB) process, J. Alloys Compd. 489 (2010) 103–109. doi:10.1016/j.jallcom.2009.09.022.
[60] X. Cui, G. Fan, L. Geng, H. Wu, J. Pang, J. Gong, Influence of raw material selection and fabrication parameters on microstructure and properties of micro-laminated TiB2–TiAl composite sheets, Mater. Sci. Eng. A. 589 (2014) 83–88. doi:10.1016/j.msea.2013.09.070.
[61] L. Li, K. Nagai, F. Yin, Progress in cold roll bonding of metals, Sci. Technol. Adv. Mater. 9 (2008) 023001. doi:10.1088/1468-6996/9/2/023001.
[62] D. Pan, K. Gao, J. Yu, Cold roll bonding of bimetallic sheets and strips, Mater. Sci. Technol. 5 (1989) 934–939. doi:10.1179/mst.1989.5.9.934.
[63] J.-M. Lee, B.-R. Lee, S.-B. Kang, Control of layer continuity in metallic multilayers produced by deformation synthesis method, Mater. Sci. Eng. A. 406 (2005) 95–101. doi:10.1016/j.msea.2005.06.030.
[64] Y.-M. Hwang, H.-H. Hsu, H.-J. Lee, Analysis of plastic instability during sandwich sheet rolling, Int. J. Mach. Tools Manuf. 36 (1996) 47–62. doi:10.1016/0890-6955(95)92628-C.
[65] R. Jamaati, M.R. Toroghinejad, The Role of Surface Preparation Parameters on Cold Roll Bonding of Aluminum Strips, J. Mater. Eng. Perform. 20 (2011) 191–197. doi:10.1007/s11665-010-9664-7.
[66] C. Suryanarayana, Mechanical alloying and milling, Prog. Mater. Sci. 46 (2001) 1–184. doi:10.1016/S0079-6425(99)00010-9.
[67] P. J. Hsieh, Y. P. Hung, S. I. Chou, J. Huang, Nanocrystallization and Amorphization Mechanisms in Zr-X Alloys during the ARB Process, 2004. doi:10.2320/matertrans.45.2686.
[68] J.Y. Zhang, Y. Liu, J. Chen, Y. Chen, G. Liu, X. Zhang, J. Sun, Mechanical properties of crystalline Cu/Zr and crystal–amorphous Cu/Cu–Zr multilayers, Mater. Sci. Eng. A. 552 (2012) 392–398. doi:10.1016/j.msea.2012.05.056.
[69] J.Y. Zhang, G. Liu, J. Sun, Self-toughening crystalline Cu/amorphous Cu–Zr nanolaminates: Deformation-induced devitrification, Acta Mater. 66 (2014) 22–31. doi:10.1016/j.actamat.2013.11.061.
[70] J.Y. Zhang, G. Liu, J. Sun, Crystallization-aided extraordinary plastic deformation in nanolayered crystalline Cu/amorphous Cu-Zr micropillars, Sci. Rep. 3 (2013) 2324.
[71] W. Guo, E.A. Jägle, P.-P. Choi, J. Yao, A. Kostka, J.M. Schneider, D. Raabe, Shear-Induced Mixing Governs Codeformation of Crystalline-Amorphous Nanolaminates, Phys Rev Lett. 113 (2014) 035501. doi:10.1103/PhysRevLett.113.035501.
[72] W. Guo, J. Yao, E.A. Jägle, P.-P. Choi, M. Herbig, J.M. Schneider, D. Raabe, Deformation induced alloying in crystalline – metallic glass nano-composites, Mater. Sci. Eng. A. 628 (2015) 269–280. doi:10.1016/j.msea.2015.01.062.
[73] M.C. Liu, X.H. Du, I.C. Lin, H.J. Pei, J.C. Huang, Superplastic-like deformation in metallic amorphous/crystalline nanolayered micropillars, Bulk Met. Glas. VIII. 30 (2012) 30–34. doi:10.1016/j.intermet.2012.03.037.
[74] J.Y. Zhang, G. Liu, S.Y. Lei, J.J. Niu, J. Sun, Transition from homogeneous-like to shear-band deformation in nanolayered crystalline Cu/amorphous Cu–Zr micropillars: Intrinsic vs. extrinsic size effect, Acta Mater. 60 (2012) 7183–7196. doi:10.1016/j.actamat.2012.09.027.

[75] Z. Pan, T.J. Rupert, Amorphous intergranular films as toughening structural features, Acta Mater. 89 (2015) 205–214. doi:10.1016/j.actamat.2015.02.012.
[76] C. Brandl, T.C. Germann, A. Misra, Structure and shear deformation of metallic crystalline–amorphous interfaces, Acta Mater. 61 (2013) 3600–3611. doi:10.1016/j.actamat.2013.02.047.
[77] K. Chen, S. Shi, W. Zhu, X. Peng, Plastic deformation due to interfacial sliding in amorphous/crystalline nanolaminates, Comput. Mater. Sci. 109 (2015) 266–276. doi:10.1016/j.commatsci.2015.07.032.
[78] B. Cheng, J.R. Trelewicz, Mechanistic coupling of dislocation and shear transformation zone plasticity in crystalline-amorphous nanolaminates, Acta Mater. 117 (2016) 293–305. doi:10.1016/j.actamat.2016.07.011.
[79] ASTM International, ASTM E3-11(2017), Standard Guide for Preparation of Metallographic Specimens, (n.d.). http://www.astm.org/cgi-bin/resolver.cgi?E3-11(2017).
[80] ASTM International, ASTM E1558-99, Standard Guide for Electrolytic Polishing of Metallographic Specimens, (n.d.). www.astm.org.
[81] M. Nowell, R. A. Witt, B. W. True, EBSD Sample Preparation: Techniques, Tips, and Tricks, 2005. doi:10.1017/S143192760550672X.
[82] W.C. Oliver, G.M. Pharr, An improved technique for determining hardness and elastic modulus using load and displacement sensing indentation experiments, J. Mater. Res. 7 (1992) 1564–1583. doi:10.1557/JMR.1992.1564.
[83] M.I. Mendelev, M.J. Kramer, R.T. Ott, D.J. Sordelet, D. Yagodin, P. Popel, Development of suitable interatomic potentials for simulation of liquid and amorphous Cu–Zr alloys, Philos. Mag. 89 (2009) 967–987. doi:10.1080/14786430902832773.
[84] C. Deng, C.A. Schuh, Atomistic mechanisms of cyclic hardening in metallic glass, Appl. Phys. Lett. 100 (2012) 251909. doi:10.1063/1.4729941.
[85] D.Z. Chen, C.Y. Shi, Q. An, Q. Zeng, W.L. Mao, W.A. Goddard, J.R. Greer, Fractal atomic-level percolation in metallic glasses, Science. 349 (2015) 1306. doi:10.1126/science.aab1233.
[86] C. Tang, P. Harrowell, Anomalously slow crystal growth of the glass-forming alloy CuZr, Nat Mater. 12 (2013) 507–511.
[87] S. Plimpton, Fast Parallel Algorithms for Short-Range Molecular Dynamics, J. Comput. Phys. 117 (1995) 1–19. doi:10.1006/jcph.1995.1039.
[88] Q. Du, V. Faber, M. Gunzburger, Centroidal Voronoi Tessellations: Applications and Algorithms, SIAM Rev. 41 (1999) 637–676. doi:10.1137/S0036144599352836.
[89] Alexander Stukowski, Visualization and analysis of atomistic simulation data with OVITO–the Open Visualization Tool, Model. Simul. Mater. Sci. Eng. 18 (2010) 015012.
[90] C.H. Rycroft, VORO++: A three-dimensional Voronoi cell library in C++, Chaos Interdiscip. J. Nonlinear Sci. 19 (2009) 041111. doi:10.1063/1.3215722.
[91] A.P. Thompson, S.J. Plimpton, W. Mattson, General formulation of pressure and stress tensor for arbitrary many-body interaction potentials under periodic boundary conditions, J. Chem. Phys. 131 (2009) 154107. doi:10.1063/1.3245303.
[92] R.J. Swenson, Comments on virial theorems for bounded systems, Am. J. Phys. 51 (1983) 940–942. doi:10.1119/1.13390.
[93] E. Schmid, W. Boas, Plasticity of crystals with special reference to metals, F.A. Hughes, London, 1950.
[94] ASM International., Handbook Committee., ASM handbook. Volume 4, Volume 4, (1991). http://app.knovel.com/hotlink/toc/id:kpASMHVHT3/asm-handbook-volume.
[95] O.J. Kwon, Y.C. Kim, K.B. Kim, Y.K. Lee, E. Fleury, Formation of amorphous phase in the binary Cu−Zr alloy system, Met. Mater. Int. 12 (2006) 207–212. doi:10.1007/BF03027532.
[96] R. Nielsen, Zirconium and Zirconium Compounds, in: Ullmanns Encycl. Ind. Chem., American Cancer Society, 2000. doi:10.1002/14356007.a28_543.

[97] Arrhenius Svante, Über die Dissociationswärme und den Einfluss der Temperatur auf den Dissociationsgrad der Elektrolyte, Z. Für Phys. Chem. 4U (1889) 96. doi:10.1515/zpch-1889-0408.
[98] P. Villars, K. Cenzual, CuZr2 Crystal Structure: Datasheet from "PAULING FILE Multinaries Edition – 2012" in SpringerMaterials (http://materials.springer.com/isp/crystallographic/docs/sd_0310057), Springer-Verlag Berlin Heidelberg & Material Phases Data System (MPDS), Switzerland & National Institute for Materials Science (NIMS), Japan, n.d. http://materials.springer.com/isp/crystallographic/docs/sd_0310057.
[99] Y. Wang, J. Yao, Y. Li, Glass formation adjacent to the intermetallic compounds in Cu-Zr binary system, J. Mater. Sci. Technol. (2017). doi:10.1016/j.jmst.2017.09.008.
[100] Y. Cui, P. Huang, F. Wang, T.J. Lu, K.W. Xu, The hardness and related deformation mechanisms in nanoscale crystalline–amorphous multilayers, 7th Int. Conf. Technol. Adv. Thin Films Surf. Coat. ThinFilms2014. 584 (2015) 270–276. doi:10.1016/j.tsf.2015.01.067.
[101] G.M. Pharr, T.Y. Tsui, A. Bolshakov, W. Oliver, Effects of Residual Stress on the Measurement of Hardness and Elastic Modulus using Nanoindentation, 1994. doi:10.1557/PROC-338-127.
[102] I. Adlakha, K.N. Solanki, Structural stability and energetics of grain boundary triple junctions in face centered cubic materials, Sci. Rep. 5 (2015) 8692.
[103] I.I. Novoselov, A.V. Yanilkin, Impact of segregated interstitials on structures and energies of tilt grain boundaries in Mo, Comput. Mater. Sci. 112, Part A (2016) 276–281. doi:10.1016/j.commatsci.2015.11.004.
[104] N. Chen, L.-L. Niu, Y. Zhang, X. Shu, H.-B. Zhou, S. Jin, G. Ran, G.-H. Lu, F. Gao, Energetics of vacancy segregation to [100] symmetric tilt grain boundaries in bcc tungsten, Sci. Rep. 6 (2016) 36955.
[105] C. Deng, F. Sansoz, Size-dependent yield stress in twinned gold nanowires mediated by site-specific surface dislocation emission, Appl. Phys. Lett. 95 (2009) 091914.
[106] M. Sepúlveda-Macías, N. Amigo, G. Gutiérrez, Onset of plasticity and its relation to atomic structure in CuZr metallic glass nanowire: A molecular dynamics study, J. Alloys Compd. 655 (2016) 357–363. doi:10.1016/j.jallcom.2015.09.149.
[107] C.R. Weinberger, W. Cai, Plasticity of metal nanowires, J. Mater. Chem. 22 (2012) 3277–3292. doi:10.1039/C2JM13682A.
[108] Z. Pan, T.J. Rupert, Amorphous intergranular films as toughening structural features, Acta Mater. 89 (2015) 205–214. doi:10.1016/j.actamat.2015.02.012.
[109] J.R. Greer, W.D. Nix, Nanoscale gold pillars strengthened through dislocation starvation, Phys. Rev. B. 73 (2006) 245410.
[110] A. Jérusalem, A. Fernández, A. Kunz, J.R. Greer, Continuum modeling of dislocation starvation and subsequent nucleation in nano-pillar compressions, Scr. Mater. 66 (2012) 93–96. doi:10.1016/j.scriptamat.2011.10.009.
[111] Y. Cui, O.T. Abad, F. Wang, P. Huang, T.-J. Lu, K.-W. Xu, J. Wang, Plastic Deformation Modes of CuZr/Cu Multilayers, Sci. Rep. 6 (2016) 23306.